Enhancing Thermoelectric Properties of n-type Mg_3Sb_2 Zintl Phase through Microstructure Engineering

by

Melis Özen

A Dissertation Submitted to the

Graduate School of Sciences and Engineering

in Partial Fulfillment of the Requirements for

the Degree of

Master of Science

in

Materials Science and Engineering

December 27, 2019

Enhancing Thermoelectric Properties of n-type Mg_3Sb_2 Zintl Phase through Microstructure Engineering

Koç University

Graduate School of Sciences and Engineering

This is to certify that I have examined this copy of a master's thesis by

Melis Özen

and have found that it is complete and satisfactory in all respects,
and that any and all revisions required by the final
examining committee have been made.

Committee Members:

_____

Asst. Prof. Umut Aydemir

_____

Assoc. Prof. Uğur Ünal

_____

Asst. Prof. Enes Kılınç

Date: _____

To my lovely family…

ABSTRACT

Enhancing Thermoelectric Properties of n-type Mg_3Sb_2 Zintl Phase through Microstructure Engineering

Melis Özen

Master of Science in Materials Science and Engineering

December 27, 2019

Environmental concerns have been growing due to dramatic consequences (e.g., air pollution, global warming) of utilization of harmful energy sources such as fossil fuels. Recent studies indicate that more than 60% of energy produced in the world is lost as a form of waste heat. Therefore, harvesting waste heat would be one of the promising options to support the global energy sustainability. Thermoelectric materials, which directly convert heat to electricity or vice-versa, have gained great interests of researchers for both energy generation and refrigeration applications. To generate significant amounts of energy by using thermoelectric materials, first conversion efficiency should be increased, which is evaluated by the dimensionless figure of merit (zT). zT is defined as $zT = \alpha^2\sigma T/(\kappa_l+\kappa_e)$, where α, σ, κ_l, κ_e and T correspond to Seebeck coefficient, electrical conductivity, lattice thermal conductivity, electronic thermal conductivity and temperature, respectively. As these transport properties are interdependent, achieving optimum zT values is challenging. Zintl phase thermoelectric materials display high thermoelectric efficiencies stemming from their tunable electronic transport properties along with their inherently low thermal conductivities. Among them, Mg_3Sb_2 has recently attracted significant attention due to its high zT as an n-type material.

In this thesis study, the electrical and thermal transport properties of n-type Mg_3Sb_2 were investigated through Bi, Te, nano-boron (nB) and carbon-coated nano-boron (CnB) doping as well as microstructure engineering strategies. Pure $Mg_{3.2}Sb_2$ and $Mg_{3.2}Sb_{1.5}Bi_{0.49}Te_{0.01}$ powders have been synthesized by high energy ball milling and were sintered by spark plasma sintering technique. To decrease the thermal conductivity even further, melt-centrifugation method was applied to create dislocation arrays and porosity in the microstructure as additional phonon scattering centers. According to SEM and TEM analyses, porous microstructure and dislocation arrays were created by

centrifugation method. Further, LFA measurements proved that thermal conductivity values were decreased from 0.98 W/Km to 0.47 W/Km. When heat treatment time increased to an hour, the *zT* value has increased from 1.2 to 1.67 for $Mg_{3.2}Sb_{1.5}Bi_{0.49}Te_{0.01}$ compound. However, nB, CnB and MgB_2 incorporation experiments didn't positively contribute to the enhancement of thermoelectric properties.

Overall, the melt-centrifugation technique was applied on n-type $Mg_{3.2}Sb_2$ Zintl phase for the first time and was successful in creating lattice dislocations and a porous structure leading to substantial improvement in both peak and average *zT*s of $Mg_{3.2}Sb_{1.5}Bi_{0.49}Te_{0.01}$. This material with porous structure and lower density displays as good thermoelectric efficiency as the fully dense analogues. Since lightweight materials are preferable and advantageous for several thermoelectric applications including energy harvesting from a vehicle's exhaust system, as-prepared $Mg_{3.2}Sb_{1.5}Bi_{0.49}Te_{0.01}$ material may have a great potential to commercialize.

ÖZETÇE

Mikroyapı Mühendisliği ile n-tipi Mg_3Sb_2 Zintl Fazların Termoelektrik Özelliklerinin Geliştirilmesi

Melis Özen

Malzeme Bilimi ve Mühendisliği, Yüksek Lisans

27 Aralık 2019

Fosil yakıtlar gibi zararlı enerji kaynaklarının kullanılmasına bağlı dramatik sonuçlardan dolayı (hava kirliliği, küresel ısınma gibi) çevresel endişeler giderek büyümektedir. Son çalışmalar dünyada üretilen enerjinin %60'ının atık ısı olarak kaybedildiğini göstermektedir. Bu nedenle kayıp ısıyı toplamak küresel enerji sürdürülebilirliğini desteklemek için gelecek vadeden bir seçenek olmaktadır. Atık ısıyı enerjiye dönüştürebilen ya da enerjiden soğutma sağlayabilen termoelektrik malzemeler hem enerji üretimi hem de soğutma uygulamaları için araştırmacıların büyük ilgisini kazanmıştır. Termoelektrik malzemeleri kullanarak önemli miktarda enerji elde etmek için öncelikle boyutsuz termoelektrik değer katsayısı (zT) ile değerlendirilen termoelektrik verimlilik artırılmalıdır. zT, $zT = \alpha^2\sigma T/(\kappa_l+\kappa_e)$ olarak tanımlanmaktadır, α, σ, κ_l, κ_e ve T sırasıyla Seebeck katsayısını, elektrik iletkenliğini, örgül ısıl iletkenliğini, elektronik ısıl iletkenliğini ve sıcaklığı ifade etmektedir. Bu iletim özellikleri birbirine bağlı olduğundan dolayı ideal zT değerlerini elde etmek zorlayıcı olmaktadır. Zintl faz termoelektrik malzemeler ayarlanabilir elektronik iletim özellikleriyle yapılarından ötürü düşük ısıl iletkenliklerinden kaynaklı yüksek termoelektrik verimlilik göstermektedirler. Bunların arasında Mg_3Sb_2 n-tipi malzeme olarak yüksek zT değerinden dolayı son zamanlarda önemli ölçüde dikkat çekmektedir.

Bu tez çalışmasında, Bi-Te ve nano bor (nB) ve karbon kaplanmış nano-bor (CnB) katkılarına ilaveten mikroyapı mühendisliği stratejilerinin n-tipi Mg_3Sb_2 malzemelerinin elektriksel ve termal iletimi özelliklerine etkisi araştırılmıştır. Saf $Mg_{3.2}Sb_2$ and $Mg_{3.2}Sb_{1.5}Bi_{0.49}Te_{0.01}$ tozları yüksek enerjili bilyeli öğütücü ve kıvılcımlı plazma sinterlemesi yöntemleri kullanılarak sentezlenmiştir. Malzemelerin termal iletimini düşürmek için eriyik-santrifüjleme yöntemiyle mikroyapıda fazladan fonon saçılma

merkezleri olarak dislokasyon dizileri ve porlar oluşturulmuştur. Taramalı elekrton mikroskobu (SEM) ve geçirimli elektron mikroskobu (TEM) analizlerine göre santrifüj sonrası, dislokasyon dizileri ve boşlukların oluşumu gözlemlenmiştir. Bunlara ek olarak, lazer flaş (LFA) tekniği kullanılarak ölçülen, malzemenin termal iletkenlik değerlerinde 0.98 W/Km'den 0.47 W/Km'e düşüş gözlemlenmiştir. Isıl işlem süresinin 1 saat uygulanması, $Mg_{3.2}Sb_{1.5}Bi_{0.49}Te_{0.01}$ malzemesi için zT değerinin 1.2'den 1.67'ye kadar artmasına neden olmuştur. Fakat nB, CnB ve MgB_2 katkılama çalışmaları termoelektrik özelliklerin geliştirilmesine olumlu katkı sağlamamıştır.

Sonuç olarak, eriyik-santrifüjleme yöntemi $Mg_{3.2}Sb_{1.5}Bi_{0.49}Te_{0.01}$ malzemesine ilk defa uygulanmış ve örgül dislokasyonlar ve boşluklu yapı oluşturmada başarılı olarak hem en yüksek zT hem de ortalama zT değerlerinde önemli miktarda artışa neden olmuştur. Boşluklu yapılı ve düşük yoğunluklu bu malzemeler tamamen yoğun benzer malzemeler kadar iyi termoelektrik verimlilik göstermektedir. Malzemenin daha hafif olması araçların egzoz sistemlerinden enerji toplanması gibi birçok termoelektrik uygulama için avantajlı ve tercih edilir olduğundan hazırlanan $Mg_{3.2}Sb_{1.5}Bi_{0.49}Te_{0.01}$ malzemesi ticarileşme için büyük potansiyele sahip olabilir.

ACKNOWLEDGEMENTS

I would like to thank all the supportive people for the motivation and belief during my academic studies. Financial support provided by TÜBİTAK with grant number 218M254 is also gratefully acknowledged.

First, I would like to thank my supervisor Asst. Prof. Dr. Umut Aydemir for all his guidance and endless support. He always encouraged me and provided great opportunities throughout my thesis study.

I would like to thank Assoc. Prof. Dr. Uğur Ünal. He supported me at the beginning of my thesis study and he always shared his knowledge and experience with me. I would also like to thank Asst. Prof. Dr. Enes Kılınç for being my thesis committee member and his valuable comments.

I am also very grateful that I had chance to meet and work with Prof. Dr. Mehmet Somer. He enlightened me through his endless knowledge and life lessons. I was also lucky to work with Dr. Annamaria Miko, she taught me lots of things to handle in the laboratory.

I thank to all my group members; Yaprak Subaşı, Dr. Semih Afyon, Kamil Kiraz, Sina Khoshsima, Dr. Zerrin Altıntaş, Dr. Özge Balcı, Samet Aydın, Dr. Ferit Siyahcan, Şeyma Özdemir, Kıvanç Sağlık, İlayda Terzi, Dr. Naeimeh Sadat Peighambardoust, Dr. Aryan Azad, Ebrahim Sadeghi, for the excellent research environment and their supports.

I want to thank Prof. Yuri Grin for allowing me to visit the MPI institute and supporting me in using such advanced research facilities. I would like to express my gratitude to Dr. Igor Veremchuck. I am very lucky to have the opportunity to work with him at the Max Planck Institute in Dresden/Germany. He provided me the opportunity to work freely in his laboratory and taught how to operate some advanced devices. I would like to thank also Dr. Ulrich Burkhardt for his collaboration and WDX-SEM analysis. I am also thankful to Felix Kaisor for his support.

I would like to also thank to members of KUYTAM, Dr. Barış Yağcı for SEM analysis and Dr. Amir Motallebzadeh for his guidance in metallography.

As my friends, many thanks to Büşra Mete for her undoubted support and endless positive energy through my studies and my life. Special thanks to Müjde Yahyaoğlu for

being my side during this journey, she was like a sister, friend, colleague for me. I have learned lots of things from her and felt her support all with me. I am also lucky to have my special, thoughtful, intelligent friends throughout my life Beril Yenigül and Meliz Türkileri. I always feel their support, encouragement and love throughout my life. I know they will be by my side all the time.

Finally, I am very lucky and thankful by having a lovely family. I would like to dedicate my thesis to my thoughtful parents Hatice & Mesut Özen and my lovely sister Merve Nurseli Özen. I always feel their endless support and love beside me. And, many thanks to my brother in-law Uğur Dinç, he always gives his support without any hesitation.

TABLE OF CONTENTS

LIST OF TABLES

LIST OF FIGURES

ABBREVIATIONS

DOS	Density of States
DSC	Differential Scanning Calorimetry
EDX	Energy Dispersive X-ray
LFA	Laser Flash Analysis
PGEC	Phonon Glass Electron Concept
SEM	Scanning Electron Microscopy
SPS	Spark Plasma Sintering
TEM	Transmission Electron Microscopy
TG	Thermo Gravimetry
VEC	Valence Electron Count
WDX	Wavelength Dispersive X-ray
XRD	X-Ray Diffraction
zT	Dimensionless Figure of Merit

Chapter 1:
INTRODUCTION

Due to high amount of fossil fuel usage, the world faces several problems like huge amount of CO_2 emissions, global warming, climate change etc. The discovery of new renewable and clean energy sources as alternatives to limited fossil fuel resources is triggered by the necessity for more energy utilization and less environmental pollution.

According to various research outputs, it has been found that every year a considerable amount of energy around 30-40% is wasted as heat, during the industrial processes [1, 2]. 67% of energy becomes useless from the electrical production processes, and 33% of energy coming from manufacturing industries is released to the atmosphere[3]. For this reason, by managing the waste heat as recovery of energy release would provide the compensation for energy requirement. In this context, as a promising energy conversion method, thermoelectric technology can convert renewable waste heat to electricity without any emission. The thermoelectric devices come forward from the other heat recovery systems regarding to their distinctive properties like low cost, emission free, no moving parts, solid state form, no noise, durability, maintenance free etc. [2-4]. In figure 1.1. several industrial processes and their waste heat temperature ranges are presented. As an example, for the processes that waste heat transportation to energy resolution is relatively hard to manage, the connected thermoelectric systems seem promising to utilize the waste heat [3].

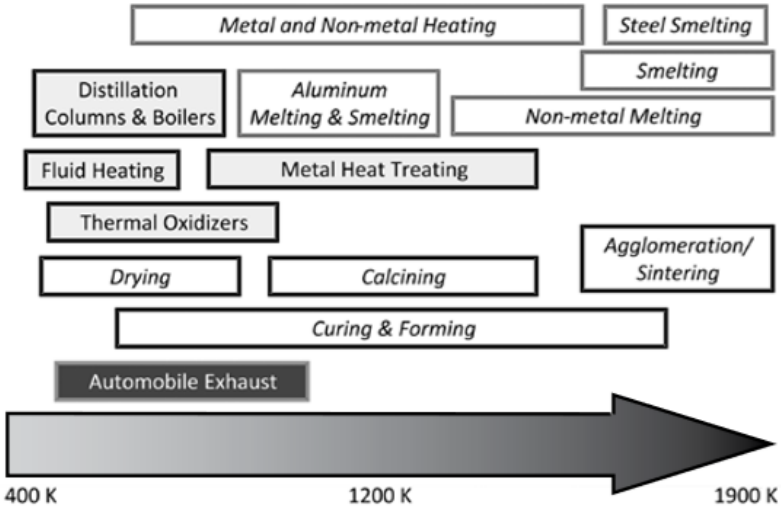

Figure 1.1 The waste heat temperatures regarding to different types of industrial operations[3]

Overall, the possible waste heat capacities as a function temperature and industrial processes are presented in figure 1.2. From the distribution of waste heat capacities, it come out that the waste heat occurs in a wide diversity from 100 °C to 1000°C. Hence, each of them requires different type of recovery systems, producing specific amount of energy related to the operation temperature. Fortunately, the thermoelectric technology enables to utilize the waste heat at several temperatures just by changing the used thermoelectric materials.

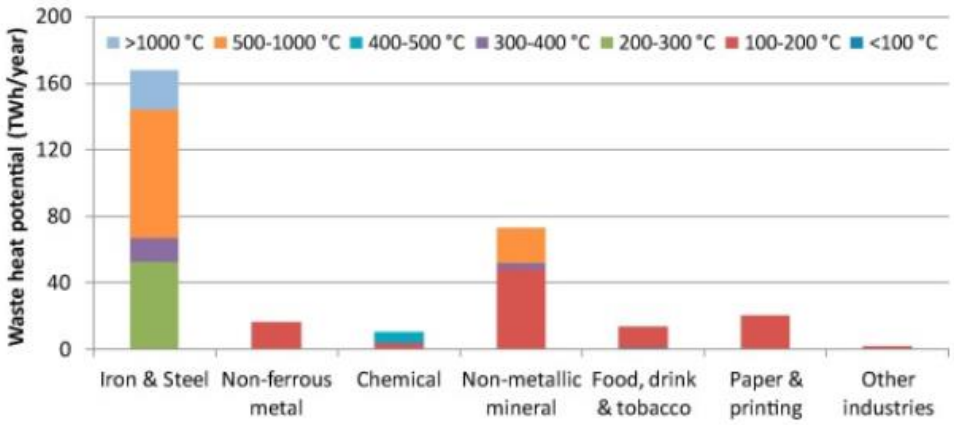

Figure 1.2 The distribution of waste heat potentials sorted by the temperature range of the processes [5]

As presented in the figure 1.3, the thermoelectric technology offers various types of thermoelectric materials as n-type and p-type for different temperature ranges. Therefore, depending on the processes that waste heat released, a proper thermoelectric material can be selected effectively. According to the waste heat capacities of industrial sectors, the highest amount of potential coming from iron-steel processes and the temperature regions are between 500-1000°C and 200-300°C.

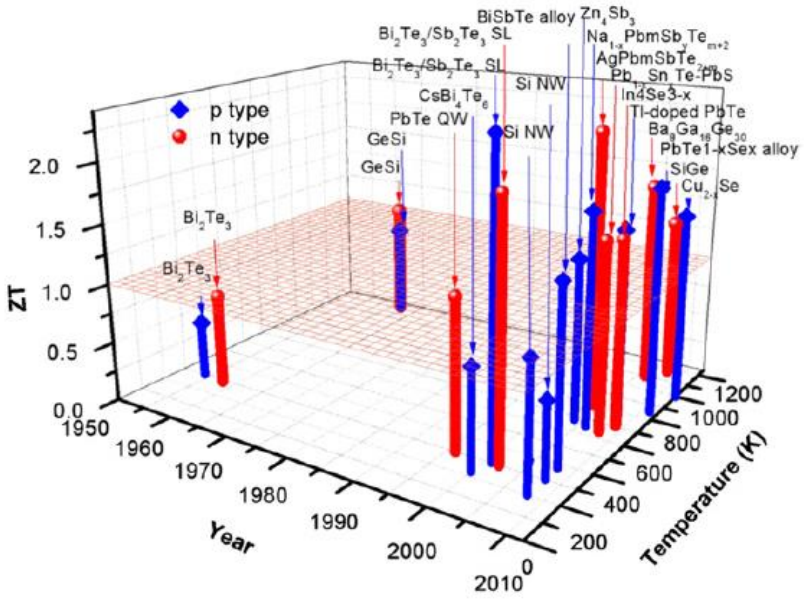

Figure 1.3 zT values (thermoelectric figure-of-merits; see section 1.2.2) of several thermoelectric materials as a function of temperature ranges [6]

In this study, n-type Mg_3Sb_2 thermoelectric material which has promising zT values around 300-500°C will be discussed. The first chapter will focus on the general thermoelectric theory and literature review about thermoelectric Zintl phases and Mg_3Sb_2-based materials. In the second chapter experimental and characterization methods will be provided. The third and fourth chapter will present the main results and discussions for different studies. At the end a conclusion section will summarize my research outputs.

Chapter 2:
THERMOELECTRIC THEORY AND LITERATURE REVIEW ON ZINTL THERMOELECTRICS

2.1 Thermoelectric Effects

The main theory of the thermoelectricity dates back to the discovery of Seebeck effect in 1821. Thomas Johann Seebeck found out that a circuit consists of two different electrically conductors would deflect a compass needle due to the electromotive force created by the temperature difference between the junctions [7]. When a temperature gradient is carried out at two different junctions, the charge carriers will move from hot side to cold side leading to a current flow and a small amount of voltage. This effect is called as the Seebeck effect or the thermopower [8]. The movement of the carriers and the developed electric field related to Seebeck effect are shown in Figure 2.1. The amount of the generated voltage is proportional to the temperature difference. The ratio of the generated voltage to the related temperature difference ($\Delta V/\Delta T$) gives the Seebeck coefficient (α) value which is material specific [9].

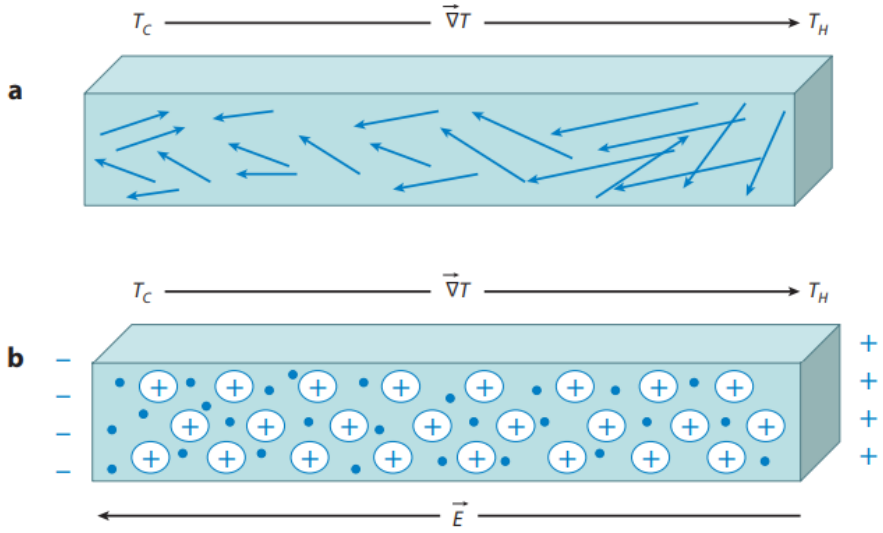

Figure 2.1 Exemplification of the Seebeck effect on the material after applied external temperature gradient a) mean free path of the electrons related to their energy, b) The diffusion of the energetic electrons from hot side to the cold side until the development of an electric field to counter the diffusion [9].

Another thermoelectric effect is the reverse of the Seebeck effect, which is called as the Peltier effect. When two different materials are connected to each other on a circuit, an applied current would force charge carriers to migrate from one side to the other. An intentional temperature gradient would form in this way, which is called as the Peltier effect. Later, this effect is utilized to produce electronic coolers (Peltier coolers) for different applications[10].

For the heat recovery and cooling purposes thermoelectric theory is applied through the thermoelectric devices either in an energy generation (Fig. 2.2a) or cooling (Fig. 2.2b) mode.

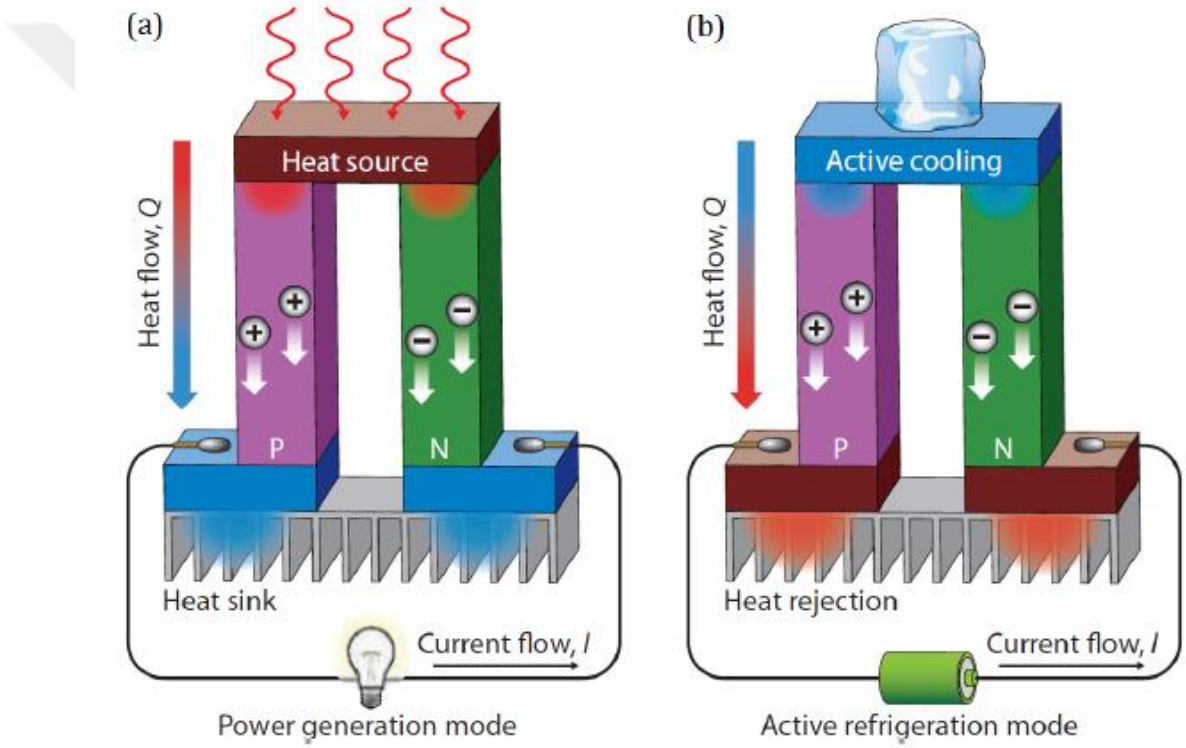

Figure 2.2 Illustration of the thermoelectric modules **a)** Seebeck effect: due to the temperature difference, charge carriers move from hot side to the cold side leading to a current flow through the circuit, **b)** Peltier effect: because of the applied current through the circuit heat generated at upper junction is absorbed at the lower junction [8].

2.2 *Thermoelectric Devices and Thermoelectric Figure of Merit*

2.2.1 Thermoelectric Figure of Merit

The efficiency of thermoelectric materials depends on the dimensionless figure of merit "z*T*" value. The figure of merit can be given by

$$zT = \frac{\alpha^2 \sigma T}{K} \quad \text{Eq.1.3}$$

where α is the Seebeck coefficient, σ is electrical conductivity, T is absolute temperature and K is thermal conductivity. Regarding to the Eq.1.3, higher *zT* values require larger Seebeck coefficient, higher electrical conductivity with lower thermal conductivity. Nevertheless, the main challenge is the dependency of these three thermoelectric parameters on the electronic properties of the materials. As discussed above, Wiedemann-Franz law ($\kappa_e = L\sigma T$) shows that the electronic thermal conductivity (κ_e) is directly proportional to the electrical conductivity. Also, both Seebeck coefficient and electrical conductivity depend upon carrier concentration as seen from Eq.1.4 and Eq. 1.9. Therefore, rather than high carrier concentration amount, achieving the optimum carrier concentration is more important to obtain higher *zT* values.

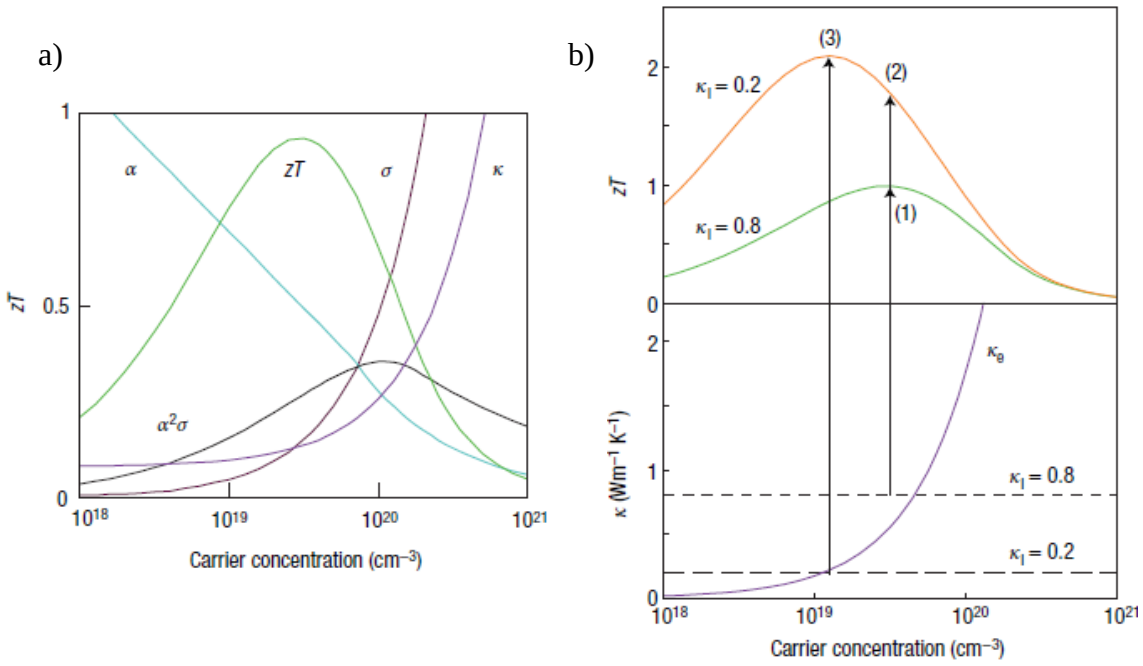

Figure 2.3 a) The relation between carrier concentration and transport properties, **b)** the dependence of *zT* to lattice thermal conductivity with the same amount of carrier concentration [11].

Figure 2.3(a) presents the relation between the carrier concentration and transport properties. Thermal conductivity of materials increases with the increasing amount of carrier concentration, because of its electronic contribution. Also, electrical conductivity increases with increasing carrier concentration, on the other hand the Seebeck coefficient decreases. (See Eq. 1.4 and 6). While combining those transport properties the optimum *zT* value could be achieved with carrier concentration between 10^{19}-10^{20} cm^{-3}. Therefore, heavily doped semiconducting materials are more attractive for thermoelectric applications rather than metals and insulating materials. Although, it is difficult to decrease thermal conductivity without effecting electrical conductivity, it can be succeeded due to the phonon contribution of thermal conductivity. As seen from Figure 2.3(b), if one can decrease the lattice thermal conductivity without changing the carrier concentration, the *zT* value can be increased.

2.2.2 Thermoelectric Devices

In a typical thermoelectric device, thermoelectric segments consisting of n-type and p-type legs which are connected to each other electrically in series and thermally in parallel as illustrated in Figure 2.4. The connection between the legs provided by the electrically conductive shunts such as copper. For the applications, the module is also combined with a heat sink to maintain the temperature difference between top and bottom sides [12].

The efficiency of thermoelectric materials mainly depends on the *zT* and thermoelectric quality factor. Firstly, the maximum efficiency of the TE power generation η is given as;

$$\eta_{max} = \frac{T_H - T_C}{T_H} \times \frac{\sqrt{1+\overline{ZT_m}}-1}{\sqrt{1+\overline{ZT_m}}+\frac{T_C}{T_H}} \quad \text{Eq.1.1}$$

where $(T_H - T_C/T_H)$ equals to the Carnot efficiency, ZT_m is the average ZT between the hot and cold temperature [13].

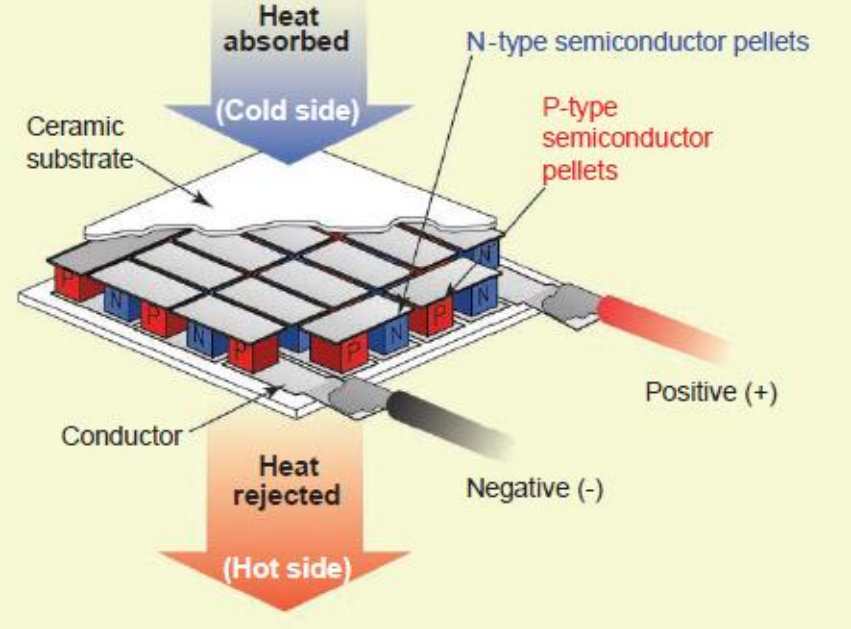

Figure 2.4 A schematic view of a thermoelectric device consisting of n and p-type thermoelectric legs that connected electrically in series and thermally in parallel[13].

Secondly, thermoelectric quality factor (B factor) can be determined related to the transport properties and band structure as follow,

$$B \propto \frac{\mu_c {m_*}^{1.5} T^{2.5}}{\kappa_L} \mathrm{E} \qquad \text{Eq.1.2}$$

where m*, κ_L, μ_c and T present the effective mass, carrier mobility, lattice thermal conductivity and specific temperature at the nondegenerate limit, respectively [13].

Figure 2.5. shows the maximum thermoelectric efficiency of devices as a function of *zT* values at different temperatures. Besides, the Carnot efficiency and the efficiency of other thermodynamic cycles like Rankine and Stirling cycles are presented. As seen from the Figure the existing systems such as solar, nuclear and coal are more efficient than thermoelectric devices. As an example, TE material with maximum zT (2.6) supplies less efficiency than other energy-conversion technologies[14]. On the other hand, it is claimed that under 100 W, thermoelectric devices become advantageous, since the sustainability at high efficiencies of Stirling and Rankine systems is more difficult [15].

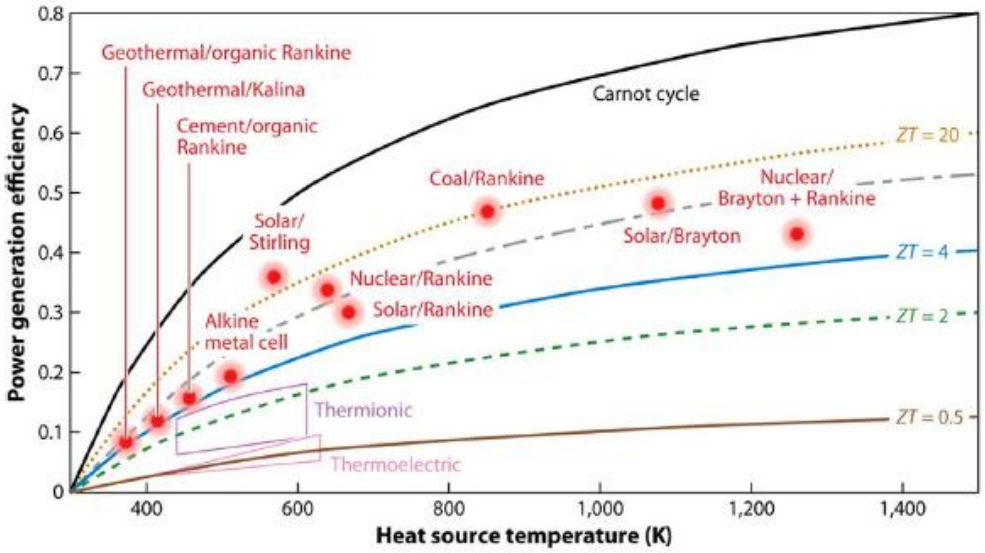

Figure 2.5 The efficiency of thermoelectric materials as a function of *zT* and comparison of them with various heat engine systems[14].

The prevalent characteristic properties of good thermoelectric materials can be assumed as;

- Many valleys should be observed near to the Fermi level to provide higher Seebeck coefficient and power factor.
- The crystal structure should be more symmetrical to achieve better electronic properties and high band degeneracy near the Fermi level.
- Compounds should involve heavier elements which causes lower lattice thermal conductivity related to phonon scattering.
- The complex crystal should be obtained to lead shorter phonon mean free path and lower lattice thermal conductivity[16].

2.3 Transport Properties

In addition to the Seebeck coefficient, the thermoelectric performance of the devices depends on the electrical resistivity and thermal conductivity of materials.

2.3.1 Seebeck Coefficient

To calculate the Seebeck coefficient, Mott formula (Eq.1.4) can be applied for degenerate metals and heavily doped semiconductors as:

$$\propto = \frac{8\pi^2 {k_B}^2}{3eh^2} m^* T \left(\frac{\pi}{3n}\right)^2 = \frac{\pi^2 k^2 T}{3e} \frac{d \ln \sigma(E)}{dE} \quad \text{Eq.1.4}$$

where k_B is the Boltzman constant, m* is the density of states effective mass, n is the carrier concentration, e is per electron charge, h is the Planck constant and σ(E) is the electronic conductivity as a function of the band filling or Fermi energy, E_F[8, 17]. Depending on the Mott equation, the carrier concentration and the band structure have important roles to optimize the thermopower (α). The Seebeck coefficient is generally very low for metals mostly around 10μV/K while it is higher for the semi-conductive materials like 300μV/K. Because the thermoelectric efficiency is directly proportional to the square of the Seebeck coefficient, semiconductor materials as thermoelectric materials are more advantageous than metals[18].

To obviate the interdependency of α and σ, several approaches have been discussed during the past years such as ideal crystal and band structure for an optimum thermoelectric material. The σ(E) is only proportional to the density of states (DOS), in the case of the independency of the electronic scattering from energy. As presented in the Eq 1.4, larger $d \ln \sigma(E)/dE$ value leads to larger Seebeck coefficient and power factor. Figure 2.6. shows the two different hypothetical electronic DOS diagrams. According to Eq. 1.4, a system like Figure 2.6(a) presents larger Seebeck coefficient.

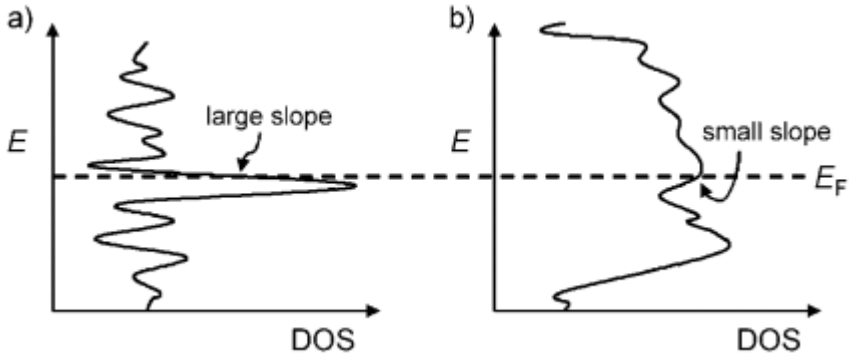

Figure 2.6 Hypothetical density of states with a) large slope $d \ln \sigma(E)/dE$ and b) small slope near E_F.

As discussed from Mott formula, the asymmetry of electronic structure near E_F quantifies the α. Therefore, the creation of several complexities in electronic structure within a small energy interval (a few kV) near E_F would provide better thermoelectric performance. For example, one can expect good complex electronic structure from

composite materials and compounds with complex structures and compositions. Figure 2.7 illustrates the electronic structure of two different semiconductor one is simple, and the other one is complex.

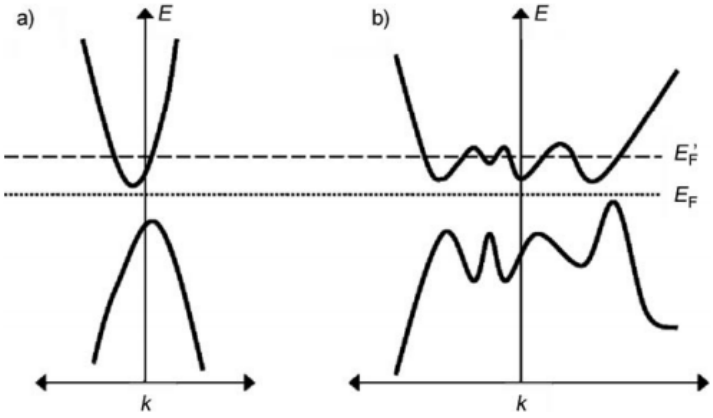

Figure 2.7 Hypothetic electronic band structures with a) single valley and b) multivalley valence and conduction band systems. If n type doping is applied on these systems, more valleys will be populated in the system b[17].

As seen from Figure 2.7(a), the system has only one band valley in the valence and conduction band, while the system in Figure 2.7(b) has several band valleys in both valence and conduction bands. Since, the power factor is related to the number of populated valleys, the system in Figure 2.7(b) is expected to have higher power factor.

2.3.2 Electrical Conductivity

As stated on the Ohm's law, the electrical conductivity can be expressed as;

$$\frac{V}{l}\sigma = \frac{I}{A} \qquad \text{Eq.1.5}$$

Where σ is the electrical conductivity, I/A is the current density J (A/cm2) and V/l is the electrical field E (V/cm). In other way the current density can be defined as Eq 1.6.

$$J = nqv \qquad \text{Eq.1.6}$$

Where n is the number of charge carriers, q is the charge of carrier and v is the average velocity. Recomposing the eq. 1.5 and utilizing the eq 1.6, the electrical conductivity can be stated as;

$$\sigma = nq\frac{v}{E} \quad \text{Eq.1.7}$$

Also, depending on the Equation 1.7, the electrical conductivity is also related to mobility of the carriers ($\frac{v}{E}$) (either electrons or holes). For conductive materials like metals the electrical conductivity highly affected from the mobility while for semiconductors the number of charge carriers more important than the mobility[19].

Under the presence of an electrical field, electrons can move preferentially through a direction leading to an average velocity[19]. Thus, the current density can be defined as;

$$J = \frac{ne^2\tau}{m}E \quad \text{Eq.1.8}$$

where m is the electron mass and τ is the average time between two collisions of electrons while moving through the solid (relaxation time). By combining eq 1.6 and eq 1.7, the electrical conductivity can be derived as;

$$\sigma = \frac{ne^2\tau}{m} \quad \text{Eq.1.9}$$

Therefore, it can be concluded that, the electrical conductivity of a materials depends on the charge carriers, the mass of the charges and the scattering mechanism inside the materials[20].

2.3.3 Thermal Conductivity

When a temperature gradient is applied to a material, the carriers inside the materials would conduct the energy by diffusion. This phenomenon is called as thermal conductivity and consists of two main components; phonon (lattice) thermal conductivity(κ_l) and electron thermal conductivity(κ_e)[21].

$$\kappa = \kappa_l + \kappa_e \quad \text{Eq.1.10}$$

In general metals show higher thermal conductivity than non-metal materials due to the heat transfer by the conduction electrons. Therefore, κ_e is more effective than the phonon thermal conductivity for conductive materials. On the other hand, for an insulator the most effective part for the thermal conductivity is provided by the movement of phonons. Coming from the elementary kinetic theory, the phonon thermal conductivity obtained from the Equation 1.11,

$$\kappa_l = \frac{1}{3} cvl = \frac{\pi^2 n {k_B}^2 T\tau}{3m_e} \quad \text{Eq.1.11}$$

where c is the heat capacity per unit volume, v is the phonon velocity, l is the mean free path of the phonons. It is seen that the terms $\frac{n\tau}{m_e}$ are involved in both Eq. 1.9 and Eq.1.11, by dividing these two equations we can get the Wiedemann-Franz Law as,

$$\frac{\kappa}{\sigma T} = \frac{\pi^2}{3}\left(\frac{k_B}{e}\right)^2 = 2.45 \times 10^{-8} W\Omega K^{-2} \quad \text{Eq.1.12}$$

at a specific temperature, in which the ratio $\frac{\kappa}{\sigma T}$ provides the Lorenz number[22]. As shown in the Wiedemann-Franz Law, the proportion of thermal conductivity to the electrical conductivity is unrelated to the phonon parameters[22]. Thus, we can define electron thermal conductivity as shown in Eq.1.13.

$$\kappa_e = L\sigma T \quad \text{Eq.1.13}$$

Since thermoelectric performance is directly proportional to the electrical conductivity while it is inversely proportional to the thermal conductivity, the decrease of the thermal conductivity without effecting the electrical conductivity is essential. As seen from Eq. 1.11, a possible strategy is changing the phonon mean free path. In this way, thermal conductivity can be decreased without affecting the electrical contribution. The possible phonon scattering mechanisms are shown in the Figure 2.8. While atomic defects are effective to scatter the short wavelength phonons, larger defects for example grain boundaries, embedded nanoparticles and interfaces are necessary to scatter mid and long wavelength phonons[23].

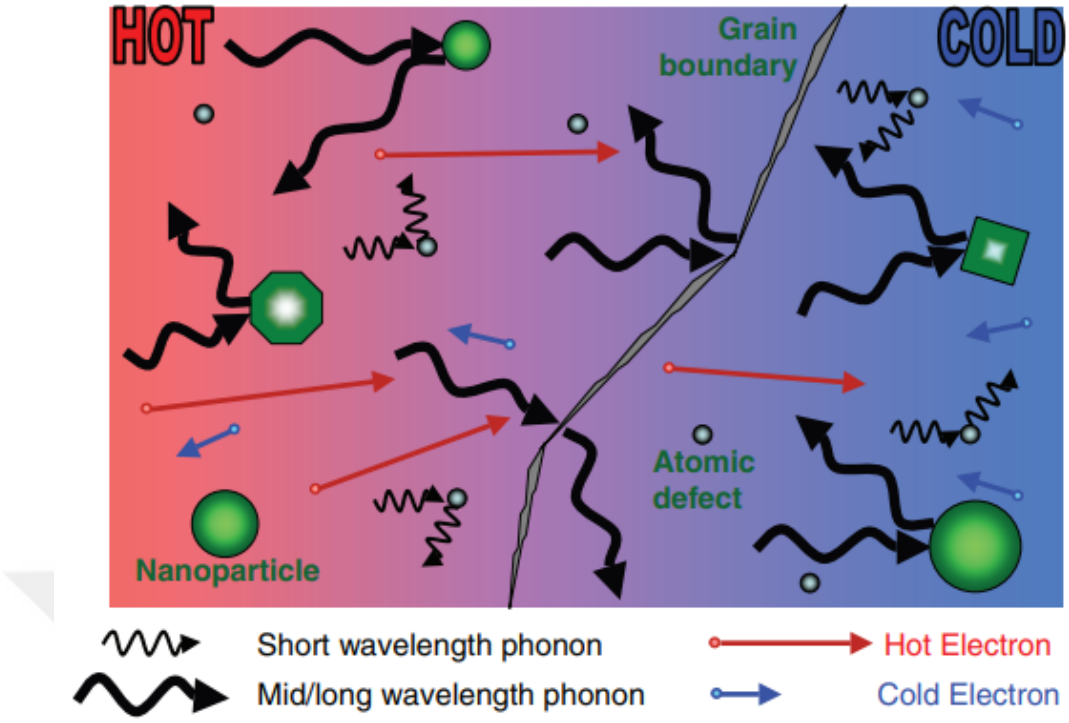

Figure 2.8 Schematic diagram of several phonon scattering mechanism within the thermoelectric material together with hot and cold electron transportation. Atomic defects to scatter the short wavelength phonons, embedded larger nanoparticles to scatter mid and long wavelength phonons. Grain boundaries for scattering longer-wavelength phonons effectively[23].

2.4 Introduction to Zintl Phases

During the 1930's, Eduard Zintl synthesized several types of intermetallic compounds which are composed of alkali and alkaline earth metals in combination with some of group 13 to 15 elements. He then studied on the structure of these phases. Further, the intermetallic compounds with recognized structures were sorted by Laves and called as the "Zintl Phases".

Zintl phase compounds consist of an anionic part from electronegative elements and a cationic part consisting of electropositive group 1 and 2 elements. Therefore, these compounds are classified between intermetallic compounds and nonconductive valence compounds. The electropositive element provide valence electrons to the electronegative one and the latter fulfills its valence requirements with the resulting electron transfer [24].

After various approximations, the 8-N rule is accepted to define the bonding of these structures, where N is the total valence electron. The valence electron count (VEC) describes the total number of electrons for each anionic atom;

$$VEC(X) = \frac{[m.e(M) + x.e(X)]}{x} \qquad \text{Eq.1.14}$$

where M has m electrons and X has x electrons. When a covalent bonding occurs between the X atoms, then the octet rule can be rewritten as;

$$b(XX) = 8 - VEC(X) \qquad \text{Eq.1.15}$$

where b(XX) is the number of bonds between X atoms. After E. Zintl revealed this idea, W. Klemm and E. Busmann improved it more [24, 25]. For the case where cations are inadequate to fulfil the need of electrons for anions, the anions create 2 center-2 electron bonding. For this reason, Zintl phases contain both ionic and covalent bonding [24, 26, 27]. While cationic part deriving the tunability and the phonon-glass structure, the polyanionic covalently bonded networks generate a complex crystalline structure, which provides electron-crystal structure [27, 28]. As an example, in NaTl structure, electrons are provided by more electropositive Na^+ cations and Tl atoms create Zintl anions by covalent bonding, resulting in an anionic Tl diamond framework. By applying the 8-N rule VEC can be calculated as, (1.1+1.3)/1= 4. In this case, 8-VEC equals to 4. Therefore, Tl atoms should generate 4 Tl-Tl bonds like group 14 elements [24]. In addition to the binary compounds, the Zintl-Klemm-Busmann concept is also applicable for the complex ternaries. One of the most common compounds AB_2X_2 which has $CaAl_2Si_2$ structure can be taken as an example. $CaAl_2Si_2$ crystallizes in a trigonal space group $P\bar{3}m$ with covalently bonded $[B_2X_2]^{2-}$ layers and A^{2+} monolayered cations [29]. $YbZn_2Sb_2$ is a good example for ternary zintl phase with layered structure, where Yb donates 2 electrons as a cation, atoms with similar electronegativities Zn and Sb create a covalently bonded $[Zn_2Sb_2]^{2-}$ framework [28].

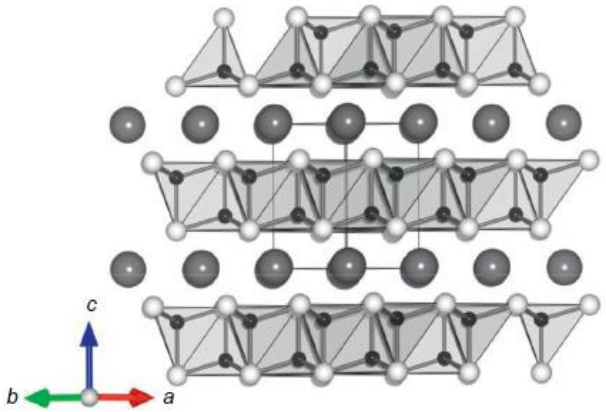

Figure 2.9 The crystal structure of AB_2X_2 compounds is illustrated where A is the large grey, B and X are the small black and white spheres. It forms with $[B_2X_2]^{2-}$ layers separated by cationic A^{2+} layers [29].

To summarize, several characteristic properties belong to Zintl compounds can be defined as following;

- They are composed of an alkali, alkaline earth and a p block element.
- They have a charge balanced electronic structure, which the necessary number of electrons for covalently bonded part is provided by electropositive element.
- They have brittle and semi-conducting characteristics.

2.4.1 Thermoelectric Zintl Phases

As mentioned above, the most important properties which make Zintl phases as good thermoelectric material are their tunable transport properties, complex structures and low thermal conductivities related to phonon glass-electron crystal structure. Zintl phases have received significant attention after adequate thermoelectric characteristics were found for $Yb_{1-x}Ca_xZn_2Sb_2$ in 2005 [30]. $Yb_{14}MnSb_{11}$ Zintl phase just discovered after a year with a zT higher than 1 [31]. Recently widescale investigations have been focused on various types of Zintl structures as thermoelectric materials; such as 0-dimensional (14-1-11), 1-dimensional (5-2-6, 3-1-3) and 2-dimensional (9-4-4, 1-2-2, 1-1-4) compounds[32]. In the last decades, several Zintl compounds like $Yb_{14}MnSb_{11}$ [31], $Ca_5Ga_2As_6$ [33], β-Zn_4Sb_3 [34], $BaGa_2Sb_2$[35], Mg_3Sb_2 [36, 37] have been investigated

related to their high potential to perform as a thermoelectric material. Some of the recent thermoelectric Zintl compounds and their zT values up to 1.4 are presented in Figure 2.11.

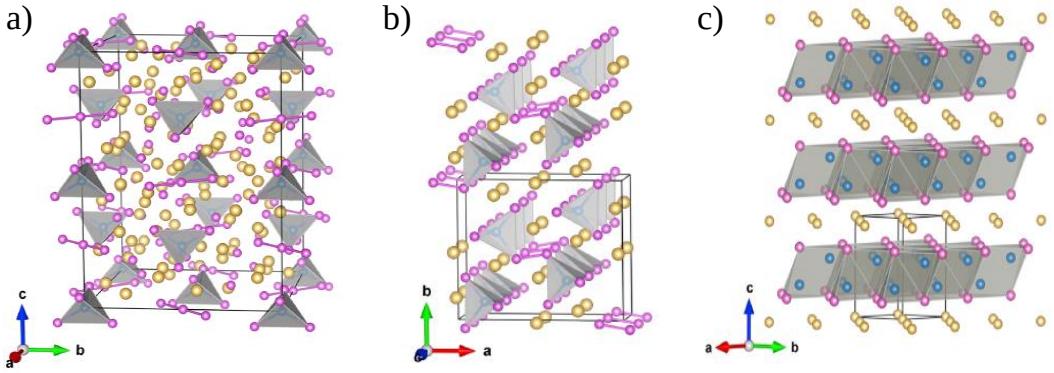

Figure 2.10 The crystal structure of thermoelectric zintl compounds where yellow spheres illustrate cations between covalently bonded anionic structure (blue and purple spheres). Gray parts show the tetrahedras. **a)** 0D anionic structure: The crystal structure of $A_{14}MPn_{11}$ presents $[MPn_4]^{9-}$ tetrahedra, the $[Pn_3]^{7-}$ polyatomic anions (purple lines), Pn^{3-} anions (purple spheres), and A^{2+} cations (yellow spheres). **b)** 1D anionic structure: The crystal structure of $Ca_5Ga_2A_6$ with corner-sharing chains of MPn_4 tetrahedra. **c)** 2D anionic structure: The crystal structure of AB_2X_2 with a layered edge shared tetrahedra between cationic A^{2+} planes[32].

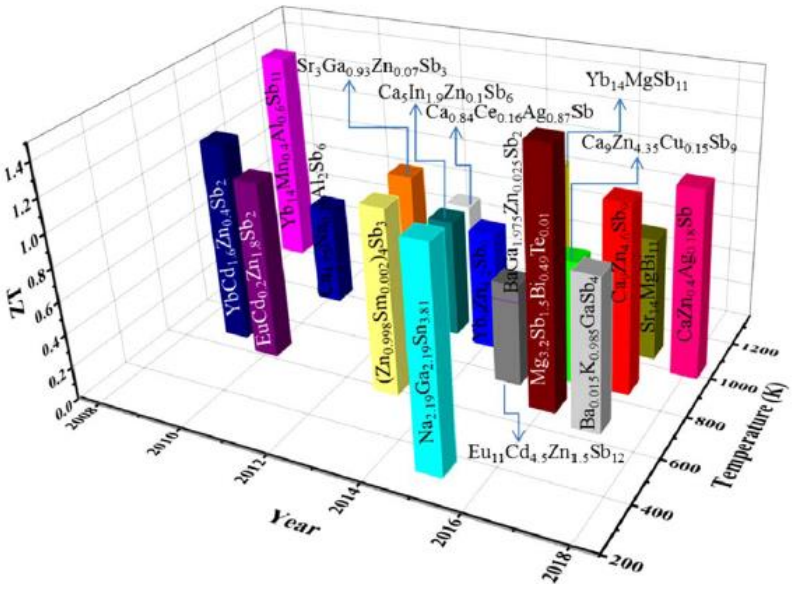

Figure 2.11 Recent developments on the zintl phase thermoelectric compounds[27].

Although their promising zT values, most of the discovered Zintl phase thermoelectric materials present p-type characteristics. The theoretical calculations and predictions shows that n-type Zintl compounds have much more potential, although more effort have been devoted to uncover p-type zintl compounds[38]. Since utilizing both p and n-type thermoelectric materials in a thermoelectric device is necessary, a relatively new discovered n-type $Mg_{3.2}Sb_2$ based thermoelectric materials with a high zT around 1.5 are getting significant attention[36]. In the next section, the investigations on optimizing and improving thermoelectric properties of $Mg_{3.2}Sb_2$ based materials are discussed.

2.4.2 The crystal and electronic structure of the Mg_3Sb_2

Among the Zintl compounds Mg_3Sb_2 based Zintl phase is promising due to its low cost, non-toxicity and abundance [39]. Mg_3Sb_2 crystallizes in the trigonal $CaAl_2Si_2$ structure with space group *P-3m*1. The crystal structure consists of an anionic $[Mg_2Sb_2]^{2-}$ layer by tetrahedrally bonded Mg and Sb atoms, and an electron donating cationic Mg^{2+} layer at the octahedral sites between two anionic frameworks as seen in Figure 1.15(a) [40, 41]. For the case of Mg_3Sb_2, while the $[Mg_2Sb_2]^{2-}$ framework providing high hole mobility and complex crystal structure, Mg^{2+} cations are responsible for good tunability and low thermal conductivity. As mentioned in the Zintl phase section, such a behavior brings along both phonon glass and electron-crystal structure together. This is called as phonon-glass electron crystal concept (PGEC) and is highly attractive for the thermoelectric utilizations.

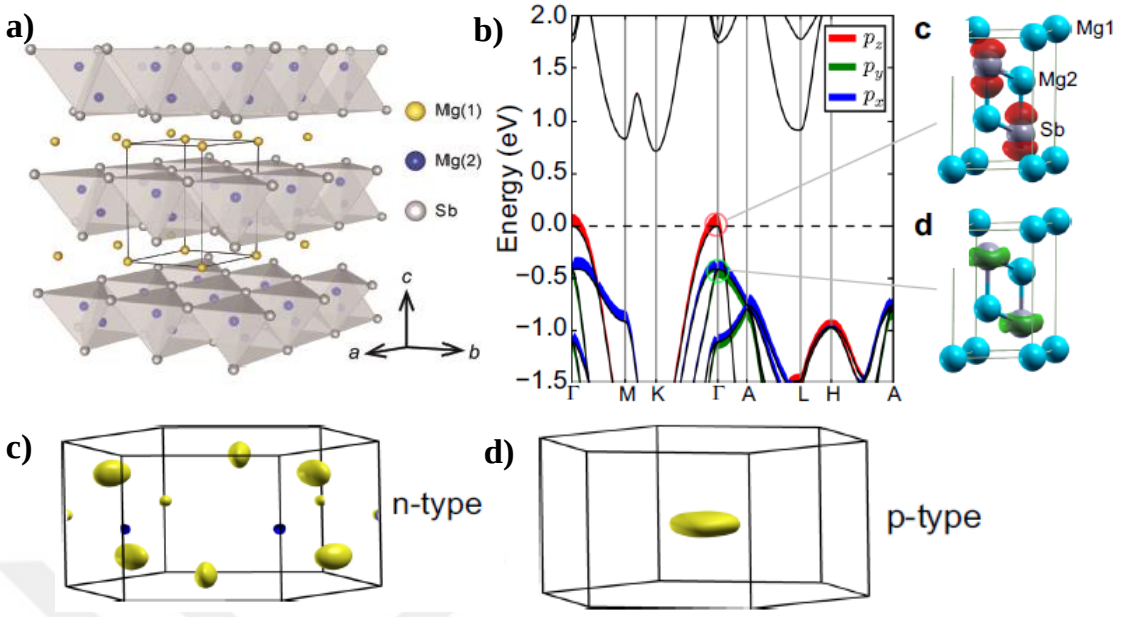

Figure 2.12 a) The crystal structure of Mg_3Sb_2 consisting of anionic $[Mg_2Sb_2]^{2-}$ layer and electron donating cationic Mg^{2+} layer along the c axis, **b)** the band structure and density of states of Mg_3Sb_2 indicating the p orbitals of Sb atoms, **c)** six degenerate carrier pockets of n-type Mg_3Sb_2 in Fermi surface at the conduction band minimum, **d)** one carrier pocket of p-type Mg_3Sb_2 at the valence band maximum (Γ point).

As mentioned on the previous sections, high zT values are intensely dependent on the large effective mass, high valley degeneracy and high carrier mobility. Since the electronic states close to the conduction band minimum and valence band maxima are very effective on those transport properties, the electronic structure of the materials become important for the thermoelectric properties. In the case of Mg_3Sb_2, Sb atoms are the main responsible atoms for the valence band and high density of states near to the Fermi level, while Mg(1) atoms are in charge of the conduction band. Also, the covalent bonding character between Mg-Sb, coming from the hybridized DOS of Mg(II) p states and Sb p states provides benefits for the electrical transport [42].

Figure 2.12(b) presents the calculated electronic band structure and density of states of Mg_3Sb_2. The indirect band gap of Mg_3Sb_2 is determined by density functional theory (DFT) as 0.6 eV with valence band maximum at the Γ point and the conduction band minimum at the CB1 point and the second band minimum at the K point. Sb-p and Mg2-p orbitals are the base components that originate the valence band of the Mg_3Sb_2. The

nondegenerate $\Gamma(p_z)$ and a doubly degenerate bands $\Gamma(p_{x,y})$ derive the first and second VBM, respectively [39, 41, 43]. Depending on the theoretical and experimental studies, it has been found that while p-type Mg_3Sb_2 has only one valley degeneracy, n-type Mg_3Sb_2 provides six valley degeneracy on the conduction band[43-45]. Therefore, it is more attractive to manipulate the transport properties of n-type Mg_3Sb_2 rather than p-type Mg_3Sb_2. The complex Fermi surface with six valley degeneracy on the conduction band of the n-type Mg_3Sb_2 and the one valley degeneracy on the valence band of the p-type Mg_3Sb_2 is schematically shown in the Figure 2.12(c) and 2.12(d), respectively.

2.4.3 The strategies to improve thermoelectric properties of Mg_3Sb_2 based materials

Recently, several strategies have been implemented to increase the thermoelectric performance of Mg_3Sb_2 based materials, such as band structure engineering, orbital engineering, carrier concentration tuning, grain boundary engineering and so on. Herein, some of the studies applied to optimize the transport properties of Mg_3Sb_2 will be discussed.

As stated on the electronic structure of Mg_3Sb_2, related to the multi-valley band degeneracy of n-type Mg_3Sb_2, the first n-type $Mg_{3.2}Sb_{1.5}Bi_{0.49}Te_{0.01}$ compound was synthesized by Tamaki et al. through suppressing the formation of Mg vacancies by adding excess amount of Mg to stoichiometric composition [36]. The theory behind creating n-type $Mg_{3.2}Sb_{1.5}Bi_{0.49}Te_{0.01}$ have been discussed by Ohno et.al through phase boundary mapping. It is shown that the p-type character of the main compound is coming from the low energy electron acceptor Mg vacancy defects. Because of the high vapor pressure and reactivity of Mg it is predictable to form Mg vacancies during the synthesis steps. Figure 2.13. shows that the excess Mg region results in a higher Mg vacancy formation energy than the excess Sb region. Although it is expected from Mg_3Sb_2 to present a line compound character, the defects restrain that behavior as seen from Figure 2.13b. The vacancies of Mg are more dominant near the Sb-excess phase side than the Mg-excess side. Therefore, to create positive defect formation energy and restrain vacancy formation, synthesis of Mg_3Sb_2 near to the Mg-excess side by adding extra amount of Mg is showed up as a successful method [45].

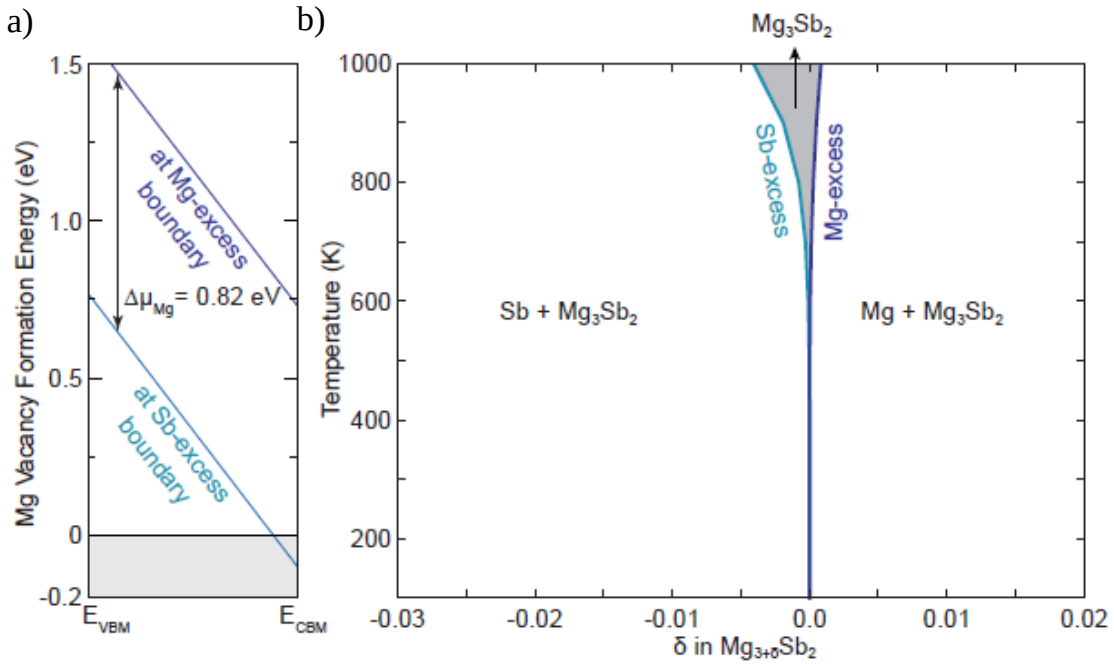

Figure 2.13 a) The formation energy of Mg vacancies showing that in the Sb-excess region blocking effect of Mg vacancies to bring the fermi level to the conduction band related to negative formation energy and high formation energy on the Mg-excess region, **b)** The phase diagram of Mg-Sb and phase boundaries with Sb-excess and Mg-excess solubility limits.

Among the several strategies to enhance the thermoelectric properties, the band engineering and orbital engineering have been found very promising related to the calculations and experimental studies. To be able to reach the most proper electrical transport properties, Zhang et.al [46], aimed to decrease the crystal field splitting energy which is derived as $\Delta = E(\Gamma(p_{x,y})) - E(\Gamma(p_z))$, and proposed the orbital engineering theory. By changing the structural variables such as the length and the angle of the bonds, interlayer distances, lattice parameters the splitting energy can be affected. Doping, alloying, creating solid solutions can be utilized to arrange the splitting energy [46]. Figure 2.14 indicates the crystal field splitting energy and orbital engineering idea for $CaAl_2Si_2$ structure such as Mg_3Sb_2. Zhang et. al purposed to enhance the electrical transport properties of p-type Mg_3Sb_2 through orbital engineering theory, but it was restricted due to the single valley degeneracy [46]. Hence, they also focused on improving the electronic transport properties of the n-type Mg_3Sb_2 [43]. Because Mg2-s orbitals show higher dependency on the K-point rather than Mg1s orbital, it is determined that

they are mostly affecting the first conduction band maximum rather than the second one. Therefore, it is proved that by disturbing the character of Mg2s–Sb_p band the CBM on the first level can be manipulated [39].

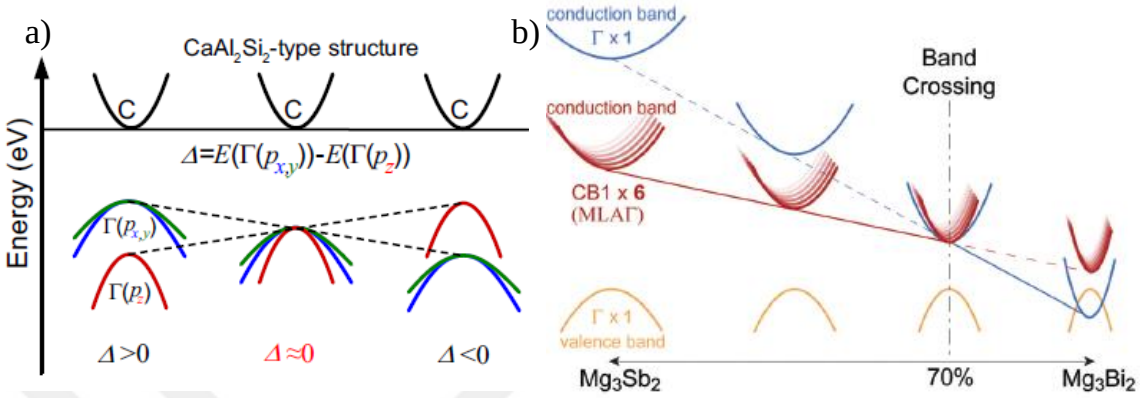

Figure 2.14 a) The illustration of the nondegenerate Γ(p_z) and a doubly degenerate bands Γ($p_{x,y}$) result from the orbitals of anions in $CaAl_2Si_2$ type structures and the definition of crystal field splitting energy at the Γ point **b)** a schematic view of conduction band engineering

In figure 2.14(b), the schematic view of the conduction band engineering is presented. Although the main component of conduction band minimum is coming from Mg1 orbitals, through the substitution of Bi or As instead of Sb atoms may change the dispersion of conduction bands and relative energy difference between them [39, 44]. Tamaki et. al, and Imasato et. al showed that by alloying Mg_3Sb_2 with Mg_3Bi_2 the band structure can be changed. Because of the increased curve characteristic in the band structure, the effective mass of the charge carriers is decreased, and mobility is increased by Bi substitution. In addition, the band gap is also decreased [36, 47].

For further studies the carrier scattering mechanisms have been investigated to optimize the electrical properties of Mg_3Sb_2 based materials. Mao et. al and Chen et. al showed that by tuning the carrier scattering mechanism [48, 49], the mechanism can vary from ionized impurity scattering to a scattering mechanism between ionized impurity and acoustic phonon. Thus, the carrier mobility can be increased. Because of the Mg vacancies in the structure, the ionization and deionization of them lead to change in the Hall carrier concentration during the heating and cooling steps. By implementing double

doping through the elements such as Mn, Co, Ta, Hf the vacancies of Mg at low temperature can be suppressed and Hall mobility can be increased [48, 49].

Another approach with respect to enhance thermoelectric properties is carrier concentration optimization around 10^{19} to 10^{20} cm^{-3}. After the capability of suppression of the Mg vacancy defects, Gorai et. al and Li et. al [50-52], have published several computational results investigating n-type doping strategies and have suggested new type dopants from group-3 elements. By calculating the defect formation energies for substitution and interstitial defects, and determining the solubility limits and phase stability they suggested several effective n-type and p-type dopants. Up to now, several studies indicated that Te doping as n-type dopant is very effective and most of the investigations selected the composition of $Mg_{3.2}Sb_{1.5}Bi_{0.49}Te_{0.01}$ as baseline [36, 45, 53-55]. After the theoretical calculations for possible dopants, high zT values and higher carrier concentrations are achieved through La, Co and Y doping [56-58].

2.4.4 Summary of Research

The main motivation of this thesis underlies the microstructure engineering to reduce the thermal conductivity of $Mg_{3.2}Sb_{1.5}Bi_{0.49}Te_{0.01}$ compound through porosity and dislocation formation by implementing a new technique called as melt-centrifugation. The success of this method is proved by Pan et. al for $(Bi,Sb)_2Te_3$ thermoelectric materials in 2018. Lattice and grain boundary dislocations with large amount of porosity is achieved by centrifugation causing to reduced lattice thermal conductivity and increased zT [59]. However, it is a quite novel idea and not applied to other systems yet.

Since changing the electronic contribution of thermal conductivity also affects the electronic transport properties of materials, it is crucial to reduce lattice thermal conductivity by phonon scattering without affecting the electronic properties of materials. In recent years it is discovered that the wide variety of phonons can be influenced related to the dislocation scattering [60-62].

The main idea of the melt-centrifugation technique is to remove liquid phase inside the mixture of solid and liquid phase, by applying a high centrifugal force. While implementing the centrifugation process, liquid phase which dispersed randomly inside the structure will be forced to move away from the bulk through the walls and bottom of

the sealed quartz ampoule. To be able to apply this technique, first a mix phase consisting of a solid and liquid part is essential. Therefore, the phase diagrams of possible thermoelectric materials which contain a eutectic phase like $(Bi,Sb)_2Te_3$ are investigated. Eventually, it is found that the phase diagram of Mg_3Sb_2 is promising. In Fig. 2.15 the phase diagram of Mg-Sb is shown. Because it has two different eutectic point in two different regions Mg-excess and Sb-excess regions, it is discussed that near to two edges of Mg_3Sb_2 phase, the melt centrifugation technique can be applied to Mg-excess and Sb-excess cases. As seen from the diagram on the left side of Mg_3Sb_2 through adding excess amount of Mg, a mixture of Mg and Mg_3Sb_2 can be achieved. By performing a heat treatment to the material up to a temperature that is higher than eutectic temperature (627°C) but lower than the melting temperature of main Mg_3Sb_2 phase, one can get a solid Mg_3Sb_2 phase with eutectic liquid phase. In that case, it is suggested that by removing proper amount of liquid Mg, the porous n-type Mg_3Sb_2 structure with dislocation arrays can be obtained. Similarly, it is considered that on the right side of the diagram by adding excess amount of Sb and applying heat treatment up to higher temperature than the eutectic temperature (580°C), a mix phase consisting of liquid phase and solid Mg_3Sb_2 phase can be achieved. For that case through the melt-centrifugation it is proposed that dislocations with large porous structure can be reached for p-type Mg_3Sb_2.

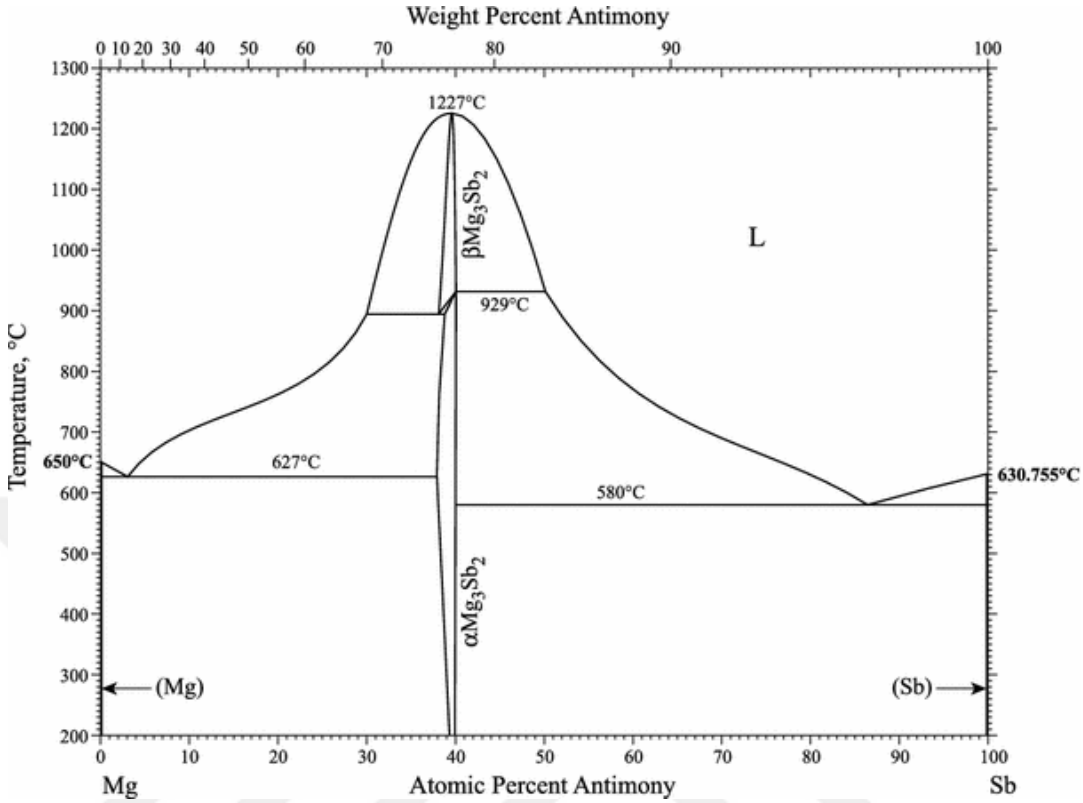

Figure 2.15 The phase diagram of Mg-Sb containing two eutectic points in Mg-excess and Sb-excess regions[63].

As a second strategy in this thesis the incorporation of superconducting MgB_2 and nano-boron doping inside the grains and grain boundaries were investigated. The main idea of this approach is also forming new phonon scattering centers by creating defects inside the structure. Related to the conductivity of MgB_2, it was expected that the electrical conductivity might not be affected as much as thermal conductivity. The doping and precipitation effects on both electrical and thermal transport properties were discussed. The reason behind the change of transport properties and the tendency of Mg vacancy defects with respect to doping of boron-based materials were discussed.

Chapter 3:

EXPERIMENTAL AND CHARACTERIZATION METHODS

In this study, some of the starting materials are known to be air sensitive; therefore, weighing and raw material preparation steps were implemented in the glove box (MBraun) under inert argon atmosphere. To reduce the particle size of the starting elements, and to synthesize the main products, high energy ball mill (SPEX8000D) was used. The compounds were produced through mechanical alloying technique. The consolidation of the fine powders was done with spark plasma sintering instrument. After the synthesis part, chemical and thermoelectric characterization were carried out through the techniques discussed below.

3.1 Materials

Starting chemicals are given in the Table 1. High energy ball mill was applied to elemental antimony and elemental bismuth to get fine particle sizes. Afterwards, all elements with fine particle sizes were used directly without further purification. For centrifugation experiments, pellet shaped samples were placed between glass wools in a quartz tube (Ø = 11 mm) and sealed under vacuum.

Table 1. Starting chemicals

Chemical	Physical State	Melting Point	Purity (%)	Company
Magnesium	Powder	650 °C	99.8	Pavezyum
Antimony	Powder	630 °C	99.999	Alfa Aesar
Bismuth	Powder	271°C	99.999	Alfa Aesar
Tellurium	Pieces	449.51 °C	99.9999	Alfa Aesar
Nano-boron	Powder	2076 °C	98.5	Pavezyum
C coated nano-boron	Powder	2076 °C	98.5	Pavezyum
MgB_2	Powder	830 °C		Lab scale

3.2 Sample Preparation Methods

3.2.1 Mechanical Alloying

A high energy ball mill machine (SPEX 8000D) was utilized to reduce particle size of starting elements and produce compounds by mechanical alloying. Simultaneously, two grinding vials could be placed between clamps in SPEX8000 Miller. The speed of these clamps reaches 875cycles/minutes. In this thesis, hardened steel vials with a highest capacity around 10 grams and half-inch stainless steel balls were used. As principle, vials were shaken in back-and-forth direction with short lateral movements and G-forces were generated on vials. During the experiment, with the effect of G-forces solid state powders react with each other and mechanical alloying took place. A schematic view of SPEX8000D is given in Figure 3.1.

Figure 3.1 Schematic view of high energy ball milling process.

In this study, Mg_3Sb_2 based different compositions were produced by using high energy ball milling. First, raw materials (Magnesium powder, bismuth powder, antimony powder, tellurium pieces, carbon coated boron powders) were weighed according to the desired stoichiometry, loaded into a stainless-steel ball milling vial with half-inch stainless-steel balls, and sealed in a glove box under an argon atmosphere. Mechanical alloying was applied for two hours. Then, the final black powder was extracted from the vial for characterization and SPS steps.

3.2.2 Ultrasonic Bath

For MgB2, carbon coated nano-boron(CnB) and nano-boron(nB) incorporation experiments, to add MgB_2, CnB and nB inside the grains and at the grain boundaries, instead of ball milling, ultrasonic dispersion method was applied by using ultrasonic bath. 40 kHz frequency was applied to disperse particles randomly.

3.2.3 Spark Plasma Sintering

Spark plasma sintering method was applied with a SPS-515 ET Sinter Lab device (Fuji Electronic Industrial Co. Ltd.) for densification of powder samples. This technique has several advantageous like short process time, production of well controlled grains and microstructure [64]. Figure 3.2 illustrates the SPS system. The SPS system consists of a vacuum chamber which creates a desired atmosphere condition, sintering machine which applies vertical single-axis forces through electrode punches, DC pulse power supply controlling the sintering processes and thermocouple measuring the temperature of the sintering environment.

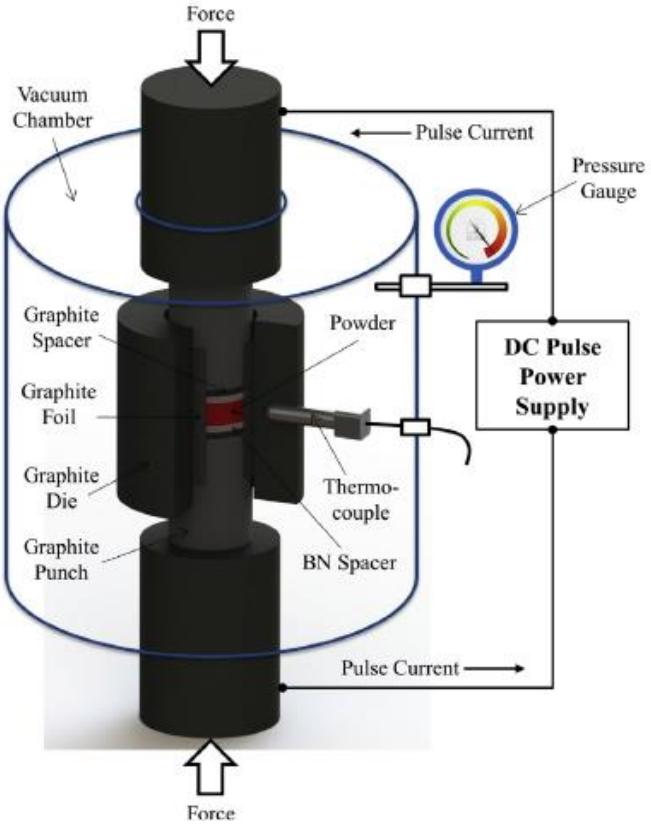

Figure 3.2 Spark Plasma Sintering System[64]

To prepare samples for SPS sintering, powder samples were placed inside the graphite die, between the graphite punches and graphite foils. By applying DC pulses, the temperature can be increased up to 1000-2500 °C in a short time. Due to the pressure and high temperature, highly compacted dense samples can be produced by SPS system. Basically, the SPS process benefits from different kind of effects such as generation of plasma, joule heating, electroplastic effect, electromigration due to the pulsed current,

and mechanical pressure [66]. Figure 3.3 demonstrates these effects on the mechanism of neck formation by SPS.

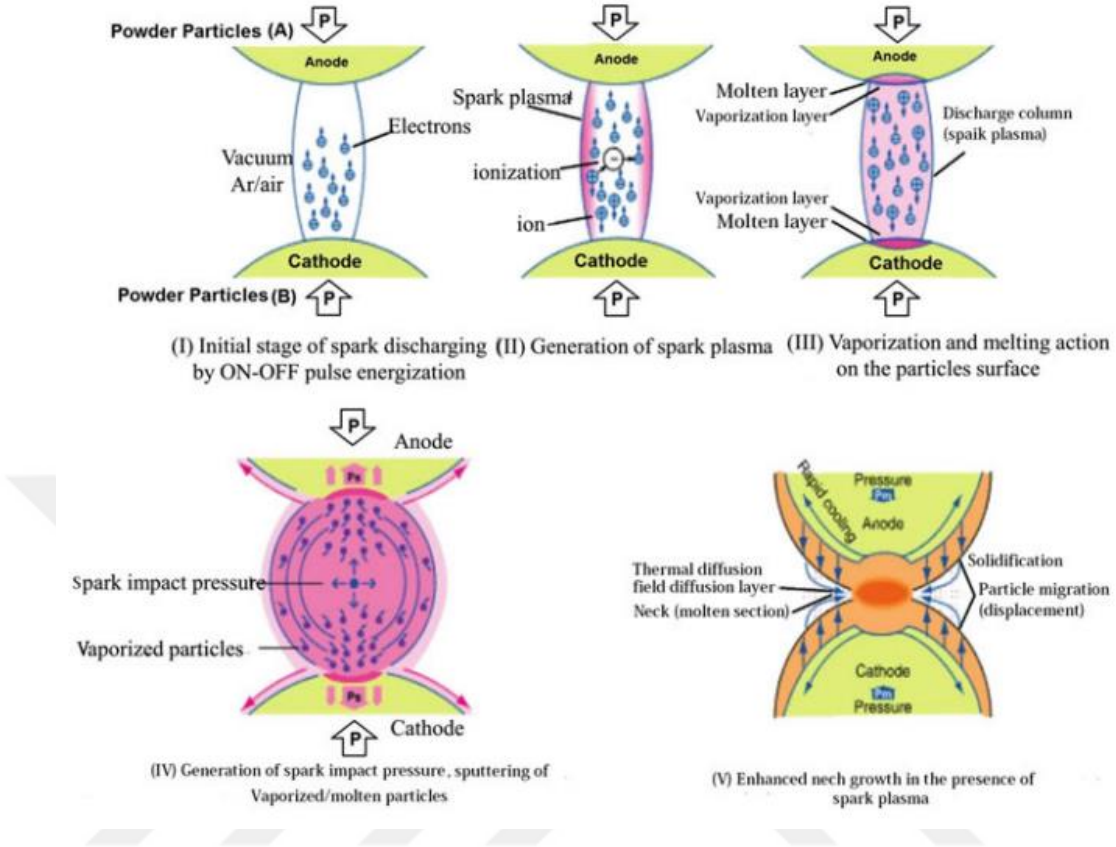

Figure 3.3 The neck formation mechanism through the SPS[65].

In theory, by SPS method, pressure is applied and held during the sintering process. However rather than the conventional systems through the SPS, sample is heated from both outside and inside due to the pulsed direct current through the graphite dies and materials themselves. When an electrical potential applied to the sample, because of the sparks at the contact points, electron flow and plasma discharges are generated between the particles. After the spark discharge on contact points, the local temperature increases up to thousands of degrees Celsius. Then, owing to the joule heating, evaporation and melting processes occurs through the surface of the particles immediately causing to the neck formation. Eventually, electroplastic effect which reduces the yield strength of metals when an electric field applied, assists the plastic deformation mechanism and speeds up the densification process[65, 66].

To consolidate powders, graphite dies (Ø=10 mm) and graphite punches were utilized. The inside of the graphite dies was covered with a graphite foil to ensure sample

purity and to take consolidated samples from the die easily. SPS process was carried out under 0.3 Torr argon atmosphere to prevent any oxidation on the surface. Different temperature and holding time parameters were applied to investigate the effect of the sintering temperature on thermoelectric properties. All the experiments were performed under 50 MPa pressure. The samples were hold at 600, 700 and 800°C for 10, 7 and 5 minutes respectively. At the end, pressure was released, and chamber was cooled down to room temperature. Highly dense bulk samples were removed from the graphite dies. For the samples prepared for centrifugation, SPS was performed at 550°C due to prevent evaporation of the excess amount of Mg content.

3.2.4 Melt Centrifugation

Centrifugation method was used to create porous microstructure and dislocations inside the structure to lower thermal conductivity. In this technique, liquid eutectic phase and excess Mg mixture were expelled from the solid MSBT phase by a strong centrifugal force. Rotating the swinging-buckets; a centrifugal force perpendicular to the spin axis was generated on the sample. A schematic diagram of melt-centrifugation is demonstrated on Fig. 3.4.

For centrifugation process, pellets were placed between quartz wools inside a quartz ampoule and placed in a furnace at 720 and 750°C to achieve a eutectic liquid phase with a solid matrix. The temperatures were selected according to phase diagram. After, the quartz ampoules were taken from furnace and put in centrifuge device immediately. Centrifugation process took place for 2 minutes with the speed of 3900 rpm. During this operation, quartz wools were also placed inside the swinging-buckets as protection medium regarding to high temperature. Through the centrifugation process the randomly distributed liquid eutectic phase was forced out of the bulk sample to the surface of the quartz ampoule.

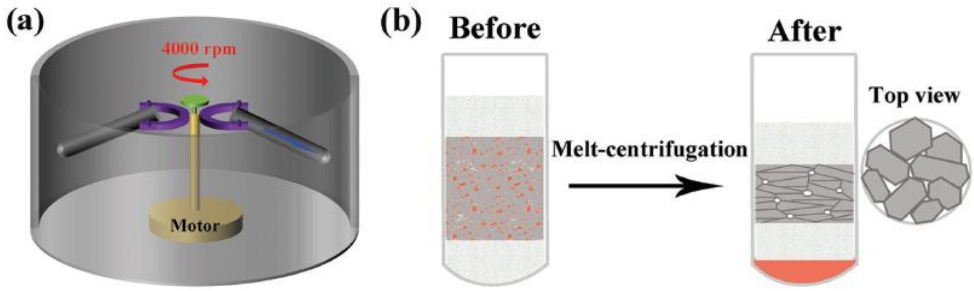

Figure 3.4 a) Schematic view of centrifugation **b)** Sample condition in the quartz ampoule before and after melt-centrifugation[59].

3.2.5 Diamond and Steel Saw Cutting

To measure the electronic transport properties with ZEM3 instrument, a rectangular shape is necessary. A digital low speed disc saw (SYJ-150) was used to cut materials in desired geometries (at least 2 mm width and depth and minimum 6 mm length). A digital micrometer provides an accurate measurement for dimension. Two different kinds of blades were used; diamond and steel. The dimensions of blades were given as 4" x 0.35 mm x 0.5". Water was used as coolant and a lubricant was also added to water to prevent corrosion and enhance efficiency of cutting process. 150 rpm speed was chosen for operation. Figure 3.5a shows the cutting setup. To make more precise dimensions and smooth surface, bar samples were ground with SiC sandpapers.

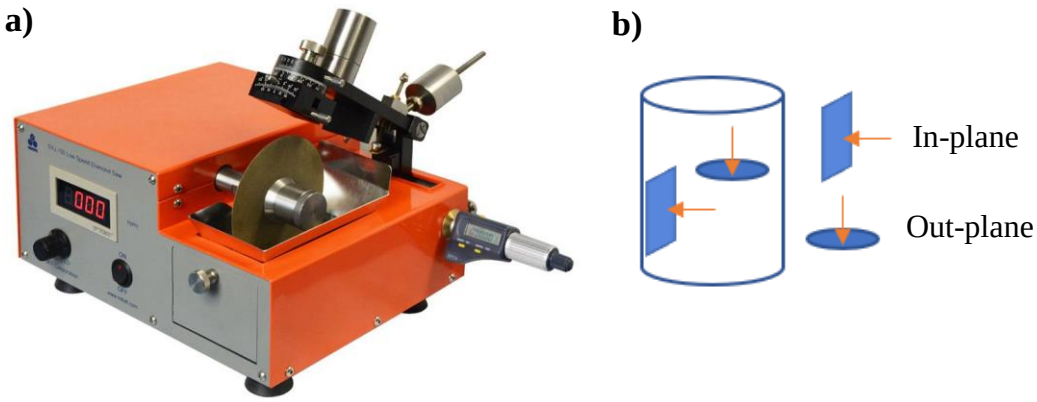

Figure 3.5 a) Digital low speed disc saw setup **b)** in-plane and out-plane directions of cutting

3.3 Material Characterization Techniques

3.3.1 X-ray Diffraction Technique

X-ray diffraction identifies the structure and the composition of materials, and gives information about lattice parameters, grain sizes and crystallinity of the samples. Powder and bulk samples were characterized by X-ray diffraction (XRD, Rigaku) with Cu Kα (λ = 1.540598 Å) radiation. 40 kV voltage and 20 mA current were applied.

X-ray diffraction is generated by the constructive interference of the X-rays and the crystalline sample. The X-rays are produced by bombarding the target material (Cu, Fe, Mo, Cr) with electrons in a cathode ray tube. To get monochromatic radiation and concentrate, these X-rays are filtered and collimated. Then, to create interference, monochromatic X-rays strikes the sample. When the requirements fulfil Bragg's Law $n\lambda = 2d \sin\theta$, constructive interference results in a diffraction pattern [68]. Because each diffraction pattern is unique, by comparing the results with the database, the chemical identity of the substance can be determined.

After XRD measurements, by using WinCSD program, the unit cell parameters of doped samples were calculated with least square refinement.

3.3.2 Scanning Electron Microscopy

To determine the morphology of the microstructure and the chemical composition Scanning Electron Microscopy (SEM) technique is a very effective multifunctional characterization technique. The main theory of the observing an image through SEM is depending on the gaining signals by the interactions between the sample and the electron beam.

SEM includes an electron gun, condenser lenses, objective lens, electron detectors and vacuum system. Basically, the electron gun generates electrons and speeds up them. These electrons go through electromagnetic lenses to provide small focused electron spot on the sample. To prevent the scattering of electrons by air, these processes take place under a high vacuum environment. When the electrons reach to the sample, incident electrons saturate into the sample and create an excitation which leads to several types of signals. Related to the characteristic of the interaction between the sample and the

electron beam different kind of signals can be produced such as; secondary electron, backscattered electron, auger electron, characteristic X-rays and cathodoluminescence [69, 70]. The secondary electron signal is the most common applied one which is produced by the ionization of atoms after the interaction between the sample and primary electrons. The secondary electrons provide information about the topography of specimens because of their low energy around 5 eV and they are able to resolve the surface structure until 10 nm. Related to the electron path, while unhindered electrons result in a bright area, those blocked electrons will result in darker images. Also, backscattered electron signals can provide compositional data in addition to the topographic data. After the elastic collision, the primary electron beams will reflect from the samples, maintaining the 60-80% energy. The reemitted backscattered signals provide contrast dependently their atomic numbers, due to the higher atomic numbers, more positive charges will lead to more backscattered electrons [70].

In this study, SEM measurements were done by Zeiss Ultra Plus Field Emission Scanning Electron Microscope. For the analyses, both fine powder and the bulk samples were placed on a holey-carbon film. Before the experiments, the bulk samples were prepared for the measurements in the metallography laboratory. First, using different size of grinding papers (800, 1200, 1500) the surface of the materials was ground, then through the polishing paper and SiC solution a bright-smooth surface was achieved.

3.3.3 Transmission Electron Microscopy (TEM)

Transmission electron microscopy provides atomic scale resolution with highly magnified images [71]. During the measurements, electron beams are applied to sample with an energy between 60-150 Kev. In the system, the electron beams are produced in the electron gun and through the condenser lenses the exposed area of the sample is determined. After the exposure of electron beams, another lens system provides an image of the distribution of electron intensities on a fluorescent screen [72]. In this thesis, TEM experiments were applied by the Hitachi Field Emission Transmission Electron Microscope HF5000. The crystal configuration and several dislocations inside the materials were analyzed through TEM images.

3.4 Physical Property Measurements

3.4.1 Thermal Diffusivity and Thermal Conductivity

LFA 467 HT Hyper Flash was performed to measure thermal diffusivity by laser flash method. Thermal diffusivity defines the impulse of a material to temperature change. In laser flash method, a short energy light pulse heats the lower surface of the sample and a temperature change on the sample occurs. This temperature variation on the upper surface of the material is detected with an infrared (IR) InSb detector. Final, the thermal diffusivity value is calculated by the equation $\alpha = 0.1388 \times \frac{d^2}{t_{\frac{1}{2}}}$, where d is the thickness of the sample and $t_{1/2}$ is the time value at half signal height.

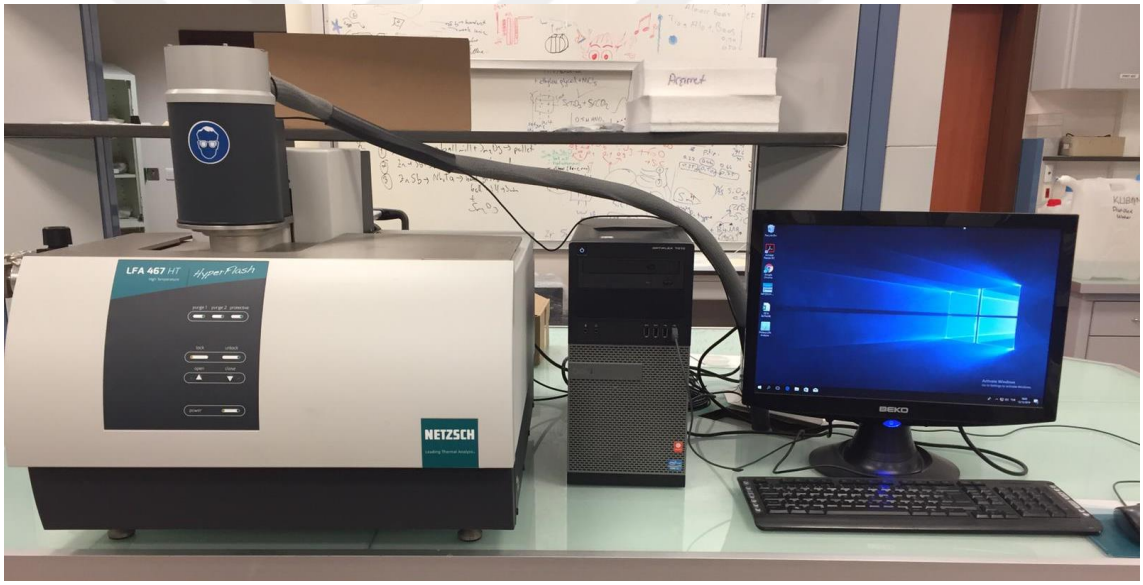

Figure 3.6 Laser flash analysis device**.**

The laser flash technique was operated from room temperature to 773 K under an argon atmosphere for 10 mm diameter pellet shaped samples. By using the thermal diffusivity value, the thermal conductivities of samples are calculated as follow;

$$\kappa(T) = d(T) \times c_p(T) \times \alpha(T) \qquad \text{Eq.1.16}$$

where κ is the thermal conductivity (W/K·m), d is the density (g/cm^3), α is the thermal diffusivity (mm^2/s) and c_p is the specific heat (J/g·K).

3.4.2 Electrical Conductivity and Seebeck Coefficient

The electrical resistivity and Seebeck coefficient measurements were performed by ULVAC ZEM-3 Seebeck Coefficient / Electrical Resistance Measurement System. All the measurement was controlled by the computer; that computer arranged the most appropriate electrical current for the resistivity determination. All measurements were taken with 10, 20, 30 K temperature differences at elevated temperatures.

In this technique, a rectangular shaped material was placed between the upper and lower electrodes in a vertical position and heated up to measurement temperatures, while a heater in the lower block was creating a temperature gradient on the sample. During the measurement a constant current I was applied through the electrodes. The temperature differences and the thermal electromotive force dE were measured by the thermocouples. The Seebeck coefficient was found with static dc method by the following equation;

$$S = \frac{\Delta V}{\Delta T} \qquad \text{Eq.1.17}$$

where S is the Seebeck coefficient (V/ K), ΔV is the voltage difference and ΔT is the temperature difference between lower and upper probes.

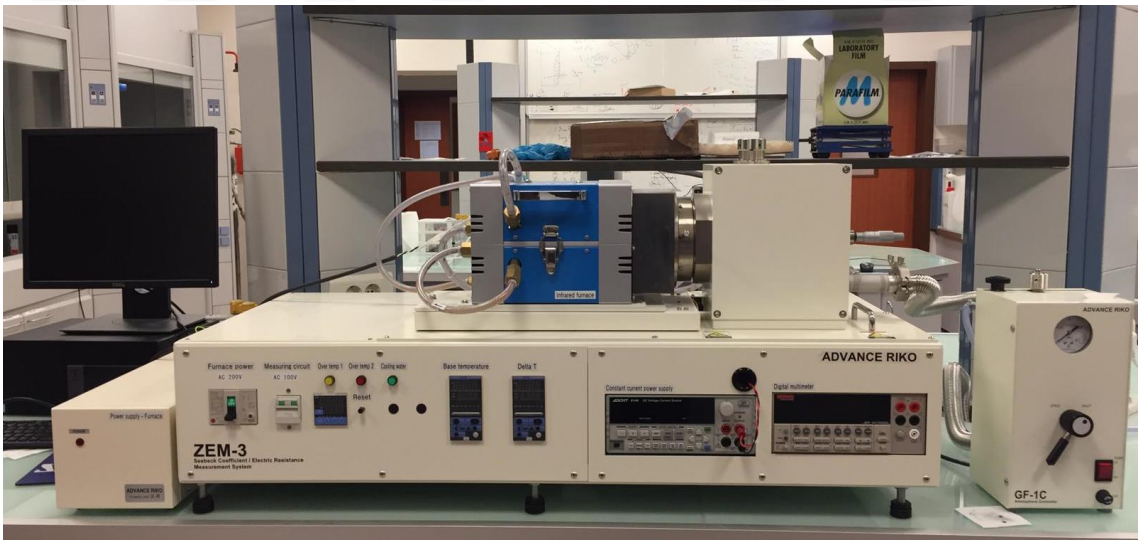

Figure 3.7 ZEM-3 Seebeck and electrical resistivity measurement system.

For the electrical resistivity measurements dc- four terminal method was used. To detect the voltage drops between the thermocouples the current was applied from both upper and lower electrodes. A schematic view of the measurement is given in the Figure 3.8. The electrical resistivity value is calculated as following;

$$R = \frac{V}{I}\frac{A}{d} \qquad \text{Eq.1.18}$$

where R is the resistance (Ohm.m), A is the cross-sectional area of the sample, I is the applied current (A) and d is the distance between the thermocouple probes.

ZEM-3 measurements require rectangular shaped material with a size between 2 to 4 square and 6 to 22 mm long. Therefore, all samples were cut in at least 6 mm heights and 2 mm widths. All the measurements were taken under a low He atmosphere rather than vacuum to create a conductive environment.

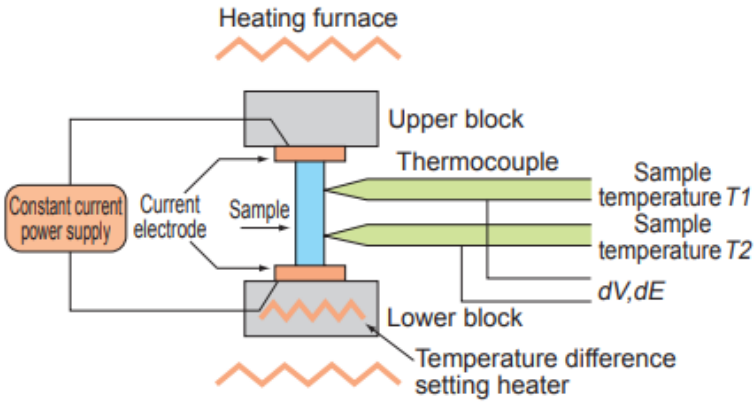

Figure 3.8 Schematic view of the electrical resistivity and Seebeck coefficient measurement system.

3.4.3 Vickers Hardness Test

To determine the microhardness of the materials Shimadzu HMV-G Series Micro Vickers Hardness Tester is applied to the samples. To measure the surface hardness first the surface of the specimen is prepared to have a flat surface. During the experiment different amounts of loads (0.098, 0.49 and 0.98 N) are applied to find the proper load.

In theory, a pyramidal shaped diamond indenter is used to load the force on the surface and kept there for 10-15 seconds without any quake and strikes. Next, the indenter is lifted from the surface the diagonals of the mark on the surface are used to calculate the Vickers hardness according to the Equation 1.16, where L is the load in kgf and d is the arithmetic mean of the two diagonals in mm [73].

$$HV = 2000L \sin\frac{\frac{a}{2}}{d^2} = \frac{1854.5L}{d^2} \qquad \text{Eq.1.16}$$

Chapter 4:

MELT-CENTRIFUGED $Mg_{3.2}Sb_{1.5}Bi_{0.49}Te_{0.01}$

In this section the characteristic properties of melt-centrifuged $Mg_{3.2}Sb_{1.5}Bi_{0.49}Te_{0.01}$ and non-centrifuged $Mg_{3.2}Sb_{1.5}Bi_{0.49}Te_{0.01}$ materials will be discussed. As a main composition the well-known $Mg_{3.2}Sb_{1.5}Bi_{0.49}Te_{0.01}$ compound was selected due to the its promising and confirmed good thermoelectric properties[36, 37, 44, 45, 48, 67, 68]. As mentioned in the first chapter melt-centrifugation was applied to get both n-type and p-type $Mg_{3.2}Sb_2$ phase based upon the phase diagram.

4.1 Preparation

The precursors are given in Chapter 2. Because Mg is air sensitive and high energy ball milling increases the reactivity of elements, all the precursors were weighed under Ar atmosphere according to the stoichiometry of $Mg_{3.2}Sb_{1.5}Bi_{0.49}Te_{0.01}$(MSBT) and $Mg_{3.2}Sb_2$, then they were placed inside a stainless-steel vial with two half inches stainless-steel balls and sealed inside the glovebox. The mechanical alloying was applied for 2 hours with SPEX8000D. The dark gray powder was subtracted from vial inside the glovebox. Later, the powder was sintered by spark plasma sintering (SPS) to produce high density bulk materials.

For SPS treatment, after covering the inside of graphite dies with a graphite foil, powder MSBT samples were filled into the graphite die between the graphite punches. Meanwhile, graphite layers with a 10 mm diameter also placed between the powder and graphite punches. The loaded graphite dies were inserted between punch electrodes in a vacuum chamber. After introducing vacuum, 0.3 Torr argon was filled into the system, and sintering process were carried out under an inert atmosphere to prevent any oxidation on the surface. The SPS was operated under 50 MPa pressure for all the samples.

For the melt-centrifugation experiments, two different preparation options were followed regarding to the amount of excess Mg and the way of addition. In the first one, excess amount of Mg element (20 wt. % and 10 wt. %) was weighed and added to vial together with other raw materials. The mixture was high energy ball milled for 2 hours. As the second option, the main composition was produced with high energy ball milling as mentioned above. Then, the dark gray powder was transferred to another stainless-steel vial to add an excess amount of Mg element and sealed again in the argon atmosphere.

After, the mixture was high energy milled for an extra 30 minutes, the final powder was taken from the vial and spark plasma sintered at 550°C for 5 minutes under 50 MPa. Because of the high amount of Mg which has high vapor pressure, the sintering temperature was changed from 600°C to 550°C for the centrifugation experiments.

For centrifugation, pellets were sealed under vacuum in a quartz ampoule with quartz wools placed top and bottom of the pellets Figure 4.1a. Afterwards, a heat treatment was applied to sealed ampoules at two different temperatures (720, 750°C), and quartz ampoules were inserted quickly to the centrifuge. The temperature of the heat treatment which is lower than the melting point of Mg_3Sb_2 compound was chosen according to the melting points of the eutectic phase and elemental Mg. To prepare centrifugation process quartz wools were placed inside the swinging-buckets and samples were centrifuged for 2 minutes with the speed of 3900 rpm. Figure 4.1b and Fig. 4.1c show that after the centrifugation, the liquid phase was removed from bulk sample through the walls of the quartz ampoule by leaving behind visible size pores. Table 4.1 summarizes the preparation conditions of non-centrifuged and centrifuged $Mg_{3.2}Sb_2$ based materials. Samples marked with "*" indicates that excess amount Mg or Sb was added during synthesis of main compound, while for other experimental parts these excess elements were put after synthesis of main phase.

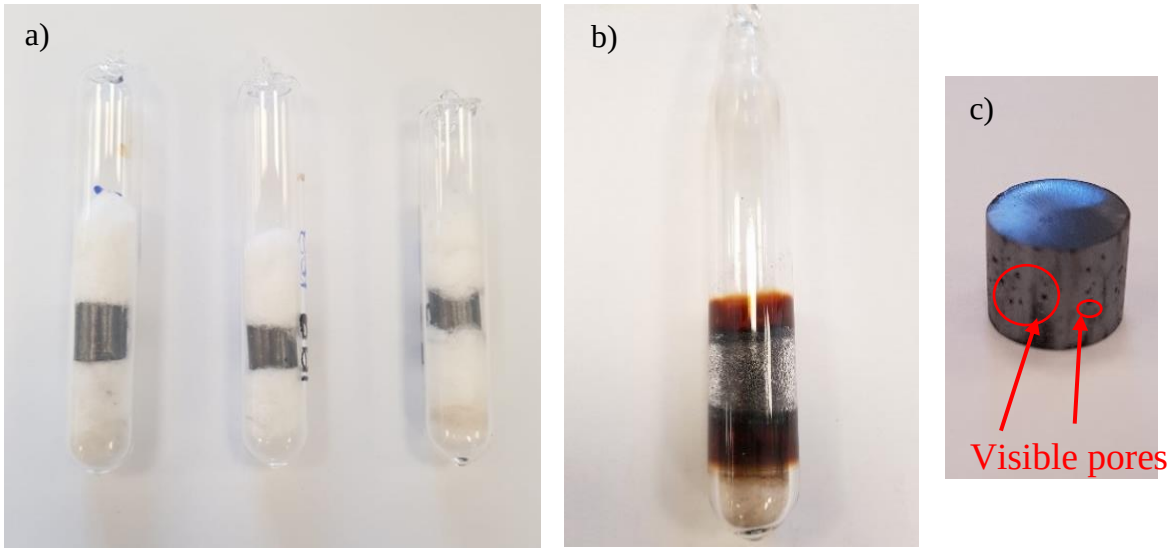

Figure 4.1 a) Samples sealed in quartz tubes under vacuum for conducting centrifugation processes, **b)** sample in the quartz ampoule after melt centrifugation (with Mg residual on the Wall of quartz ampoule) and **c)** MSBT-20wt sample after melt centrifugation with visible pores.

By using different temperatures above the melting temperature of the eutectic phase mixture, the effect of the temperature on the centrifugation process and thermoelectric properties of the materials were investigated.

Table 4.1. Preparation conditions of the Mg_3Sb_2 based compounds.

	Composition	Excess addition	Milling Time	SPS Temperature	SPS Time (min.)	Heat Treatment Temperature	Heat Treatment Time (min.)
MO40	$Mg_{3.2}Sb_2$	-	2 h	600°C	10	-	-
MO51*	$Mg_{3.2}Sb_2$	10 wt. % Mg	2 h	500°C	10	720	30
MO52*	$Mg_{3.2}Sb_2$	25 wt. % Sb	2 h	500°C	10	750	30
MO57	$Mg_{3.2}Sb_{1.5}Bi_{0.49}Te_{0.01}$	-	2 h	600°C	10	-	-
MO58*	$Mg_{3.2}Sb_{1.5}Bi_{0.49}Te_{0.01}$	10 wt. % Mg	2 h	550°C	10	720	30
MO61	$Mg_{3.2}Sb_{1.5}Bi_{0.49}Te_{0.01}$	10 wt. % Mg	2.5 h	550°C	10	720	30
MO65	$Mg_{3.2}Sb_2$	20 wt. % Mg	2.5 h	550°C	10	720	30
MO70	$Mg_{3.2}Sb_{1.5}Bi_{0.49}Te_{0.01}$	20 wt. % Mg	2.5 h	550°C	10	720	30
MO108	$Mg_{3.2}Sb_{1.5}Bi_{0.49}Te_{0.01}$	20 wt. % Mg	2.5 h	550°C	10	750	60

4.2 Crystal Structure Characterization

The crystal structure and the phase purity of the samples were determined by XRD with Cu-K_α source. Figure 4.2 shows the XRD patterns of spark plasma sintered non-centrifuged $Mg_{3.2}Sb_2$, 10 wt. % and 20 wt. % Mg excess $Mg_{3.2}Sb_2$ and 25 wt. % Sb excess $Mg_{3.2}Sb_2$ samples before and after centrifugation processes.

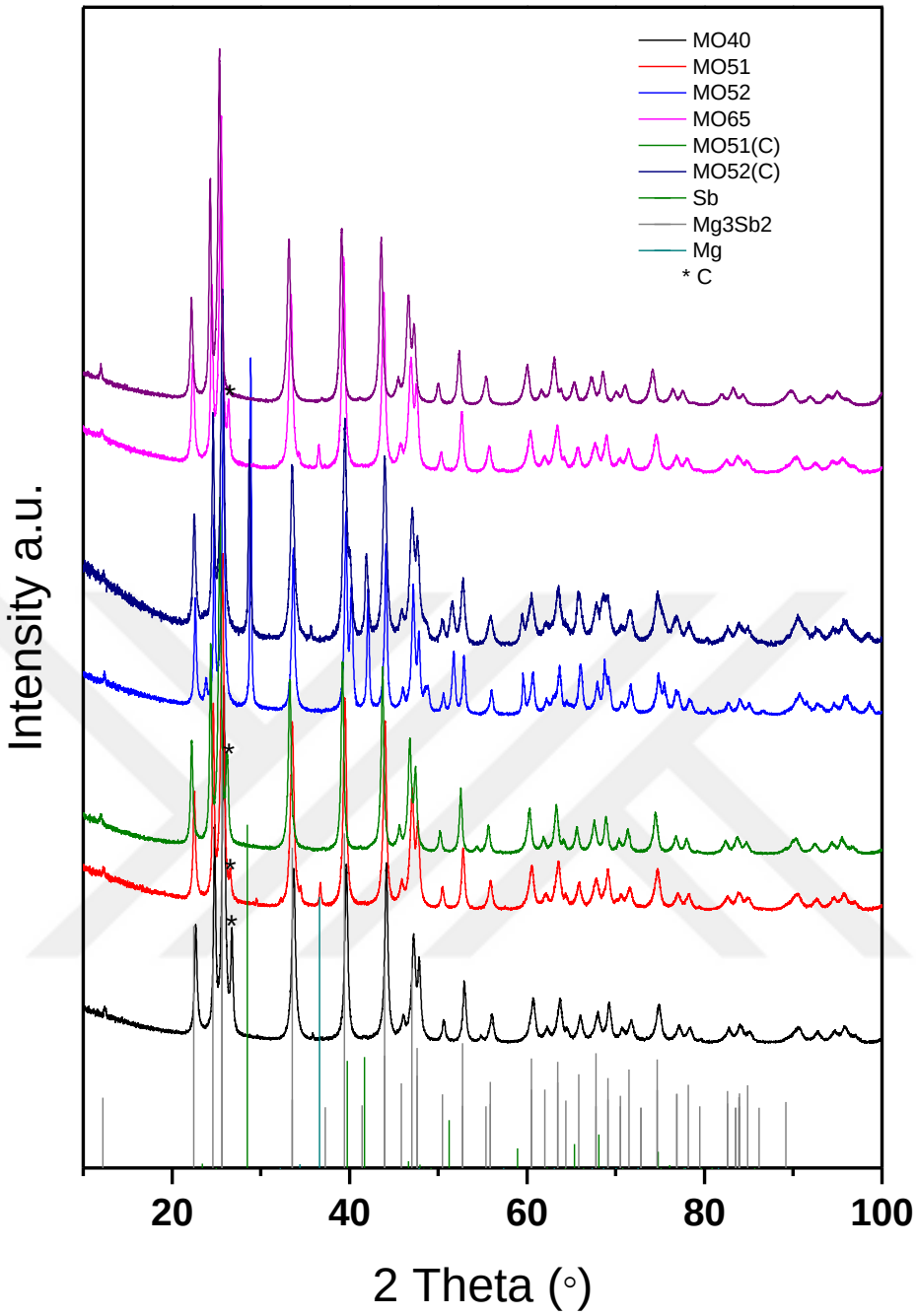

Figure 4.2 XRD patterns of $Mg_{3.2}Sb_2$ (black), 10 wt. % excess Mg added sintered (red) and centrifuged (green) $Mg_{3.2}Sb_2$, 25 wt. % excess Sb added sintered (blue) and centrifuged (dark blue) $Mg_{3.2}Sb_2$, 20 wt. % excess Mg added sintered (pink) and centrifuged (purple) $Mg_{3.2}Sb_2$

As seen from Fig. 4.2 all the main peaks belong to the trigonal Mg_3Sb_2 crystal structure in *P*-3*m*1 space group without presenting any impurity peaks. Since the XRD measurements were taken after the sintering processes some of the patterns contain

graphite peaks due to the graphite foil covered during the sintering process. Although most of them were ground with sandpaper, still little amount of graphite is observable.

In the case of excess elemental doping experiments, extra peak positions were observed which belong to Mg and Sb elements. Even, Mg has high vapor pressure and tends to create Mg vacancies, the intensity of elemental Mg peaks confirm that a considerable amount of Mg remained in the structure with the main phase Mg_3Sb_2 (red and pink lines in the Figure 4.2). To be able to determine the applicability of centrifugation technique on the p-type and n-type Mg_3Sb_2, first experiments were performed without any doping elements such as Bi and Te. For Mg excess cases, the centrifugation technique was applied successfully for the extraction of excess amount of Mg. Figure 4.2 proves that after centrifugation process, the peaks referred to elemental Mg were gone comparing to the XRD pattern of spark plasma sintered samples. On the other hand, the same result couldn't be reached with Sb excess Mg_3Sb_2 experiments. As seen in Figure 4.2, with blue and dark blue lines, the peaks corresponding to the elemental Sb remained after centrifugation. That behavior might be associated with the molecular weight of Sb (121.76 g/mol) which is 5 times heavier than the molecular weight of Mg (24.305 g/mol). As discussed in the Chapter 1, a region with two phases is required in the Mg-Sb phase diagram (Figure 1.18) to apply centrifugation. For the Sb excess case, to produce α phase Mg_3Sb_2 phase with eutectic Sb phase, at least 50% at. elemental Sb was necessary. In that case, although the heat treatment at 750°C for 30 min. was applied to get liquid eutectic phase with main solid Mg_3Sb_2 phase, during the centrifugation process for 2 minutes the decrease of the temperature might be resulted in the solidification of liquid eutectic Sb phase. Therefore, some of the excess Sb still presented in the structure after centrifugation.

Regarding to the $Mg_{3.2}Sb_2$ experimental results, the follow-up experiments were carried out based upon the n-type $Mg_{3.2}Sb_{1.5}Bi_{0.49}Te_{0.01}$ phase rather than the p-type Mg_3Sb_2. Figure 4.3 presents the XRD patterns of spark plasma sintered non-centrifuged $Mg_{3.2}Sb_{1.5}Bi_{0.49}Te_{0.01}$, 10 wt. % and 20 wt. % Mg excess $Mg_{3.2}Sb_{1.5}Bi_{0.49}Te_{0.01}$ samples before and after centrifugation processes with regarding to different heat treatment temperatures and times. The main composition matched exactly with the trigonal Mg_3Sb_2 crystal structure with a small amount of peak position changes with respect to the Bi and Te doping inside the crystal structure, but there was no impurity peak which might be

associated with undoped bismuth. All the XRD measurements prove that $Mg_{3.2}Sb_{1.5}Bi_{0.49}Te_{0.01}$ phase was produced as phase- pure. Also, as discussed for Mg_3Sb_2 experiments, a graphite peak was observed for MO61 sample. Although an extra amount of Mg (10%) was used for MO58 and MO61, after the centrifugation only a little amount of Mg, which was also seen for the main sample $Mg_{3.2}Sb_{1.5}Bi_{0.49}Te_{0.01}$, was detected. Still the main phase was considered as pure because the stoichiometry of the compound was already Mg excess rather than Mg_3Sb_2. When comparing the peak positions of the centrifuged and non-centrifuged samples, no considerable shift in the two-theta region was observed. It is thought that excess amount of Mg was extracted from the structure successfully.

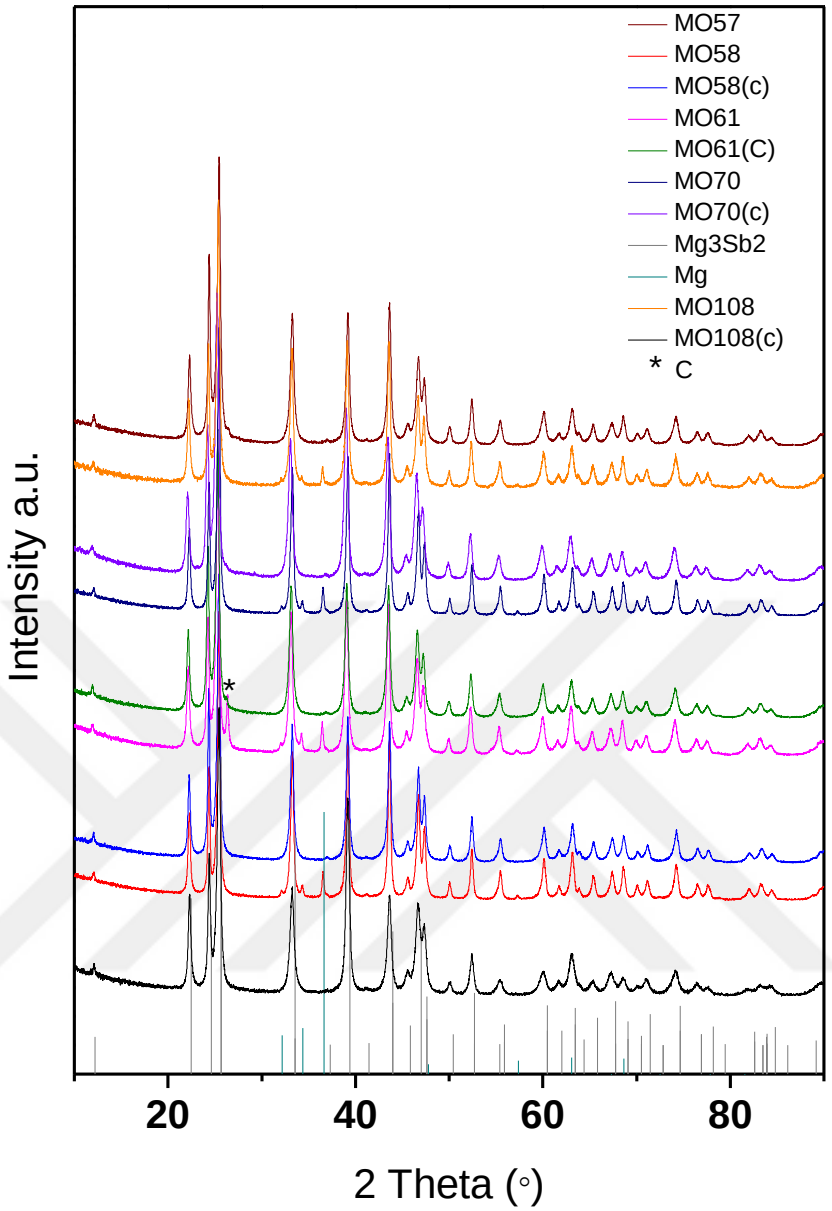

Figure 4.3 XRD patterns of $Mg_{3.2}Sb_{1.5}Bi_{0.49}Te_{0.01}$ (black), 10 wt. % excess Mg added sintered (red) and centrifuged (blue) $Mg_{3.2}Sb_{1.5}Bi_{0.49}Te_{0.01,}$ 10 wt. % excess Mg added sintered (pink) and centrifuged (green) $Mg_{3.2}Sb_{1.5}Bi_{0.49}Te_{0.01}$, 20 wt. % excess Mg added sintered (dark blue) and centrifuged (purple) $Mg_{3.2}Sb_{1.5}Bi_{0.49}Te_{0.01}$. 20 wt. % excess Mg added sintered (orange) and centrifuged (wine) $Mg_{3.2}Sb_{1.5}Bi_{0.49}Te_{0.01}$

The lattice parameters of pure $Mg_{3.2}Sb_2$, $Mg_{3.2}Sb_{1.5}Bi_{0.49}Te_{0.01}$ and centrifuged $Mg_{3.2}Sb_{1.5}Bi_{0.49}Te_{0.01}$ were calculated by using WINCSD program. These lattice parameters are given in the Table 4.2. In addition to the XRD results, the change on the lattice parameters proves that Bi and Te were successfully doped and affected the crystal structure of $Mg_{3.2}Sb_2$. When standard deviations were considered, all

$Mg_{3.2}Sb_{1.5}Bi_{0.49}Te_{0.01}$ samples displayed similar lattice parameters after the centrifugation process.

Table 4.2. Lattice parameters (a and c) of trigonal $Mg_{3.2}Sb_2$ based undoped, Bi and Te doped, and centrifuged samples

	a (Å)	**c(Å)**
MO40	4.560(1)	7.223(4)
MO57	4.582(4)	7.286(7)
MO70	4.602(1)	7.301(3)
MO70-C	4.613(3)	7.317(6)
MO108	4.601(1)	7.304(3)
MO108-C	4.596(1)	7.295(3)

4.3 Chemical and Microstructure Characterizations

All the primary samples showed high relative densities. After centrifugation process, densities were observed to decrease. As seen from the Table 4.3, spark plasma sintering method was very efficient to produce highly dense materials and it is observed that centrifugation created porous structure due to removed phases from the microstructure (Figure 4.1). The formation of porous structure and lower densities are beneficial for decreasing the thermal conductivity (Equation 2.2). Also, light weight of thermoelectric materials might be attractive for the application point of view.

Table 4.3. Density values and relative densities of spark plasma sintered and centrifuged samples calculated by geometrical method.

	MO40	**51**	**57**	**58**	**61**	**65**	**70**	**108**
Density (g/cm^3)	4.002	2.994	4.3	3.265	3.35	3.82	3.89	3.83
Relative Density %	99.0	74.1	95.7	72.6	74.5	95	86.6	85.3

For further investigations, EDX and WDX analyses were applied to determine the chemical composition and microstructure of non-centrifuged pure Mg_3Sb_2, Bi and Te doped $Mg_{3.2}Sb_{1.5}Bi_{0.49}Te_{0.01}$, and centrifuged samples.

In Figure 4.4, SEM images of samples centrifuged one at 720°C for 30 min. (MO70) and 750°C for an hour (MO108) displays that higher temperature and heat treatment time resulted in more amount of homogenously distributed porosity for MO108. In Figure 4.5, SEM images of MO40, MO57 and MO70 samples are displayed at different magnifications. Figure 4.5a presents the microstructure of pure $Mg_{3.2}Sb_2$ sample, which is highly dense and doesn't contain any porosity. Although it seems like it has some slight

scratches on the surface, EDX mapping proves that those darker lines resulting from the higher amount of Mg elements on these areas (please see appendix Figure A.1). The EDX analysis of MO40 is presented on the Figure 4.5b. The measurements were taken from 2 different spots object 1 and object 2 to be able to see the reason of color difference on the SEM images. It was detected that while bright regions contain higher amount of Sb as expected related to higher number of electrons, darker points contain slightly higher amount of Mg (2 at. %). In the Figure 4.5 c and d the microstructure of MO57 and regional EDX analysis results are given. As seen for the $Mg_{3.2}Sb_2$ case, a small color difference was observed, and the composition was measured as $Mg_2Sb_{1.5}Bi_{0.49}$. However, the Mg amount was less than the calculated value in the beginning of experimental studies and the amount of Te element couldn't detected because of the very low doping amount. Therefore, also WDX analysis was applied for this sample from 10 different spots (See Appendix Figure A.3. and Table A.1), which is better to analyze smaller amount of contents. As a result, the composition of the sample was determined as $Mg_{3,2}Sb_{1,49}Bi_{0,488}Te_{0,01}$, which is almost the same stoichiometry as the nominal composition. The atomic percent of each elements in the compound are given in Table 4.4. The microstructure of MO70 and EDX mapping images are given in Figure 4.5e, f, g, and h. Because of the heat treatment at 720°C for 30 minutes grain sizes are slightly increased from 4 to 7 μm (please see appendix Figure A.2.). In addition, after centrifugation process, porosities around 1μm to 3μm were generated mostly at the grain boundaries (Appendix Figure A.2.). The EDX mapping images for Mg, Sb and Bi elements don't contain any of these elements on some specific areas which are shown as black regions. These areas shown in Figure 4.5e correspond to the porosities inside the microstructure.

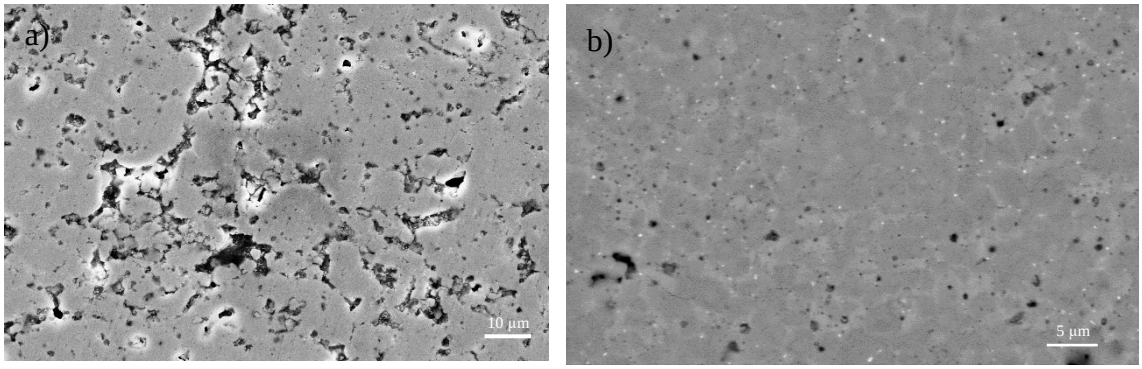

Figure 4.4 SEM images of samples centrifuged **a)** one at 750°C for an hour (MO108) and **b)** at 720°C for 30 min. (MO70).

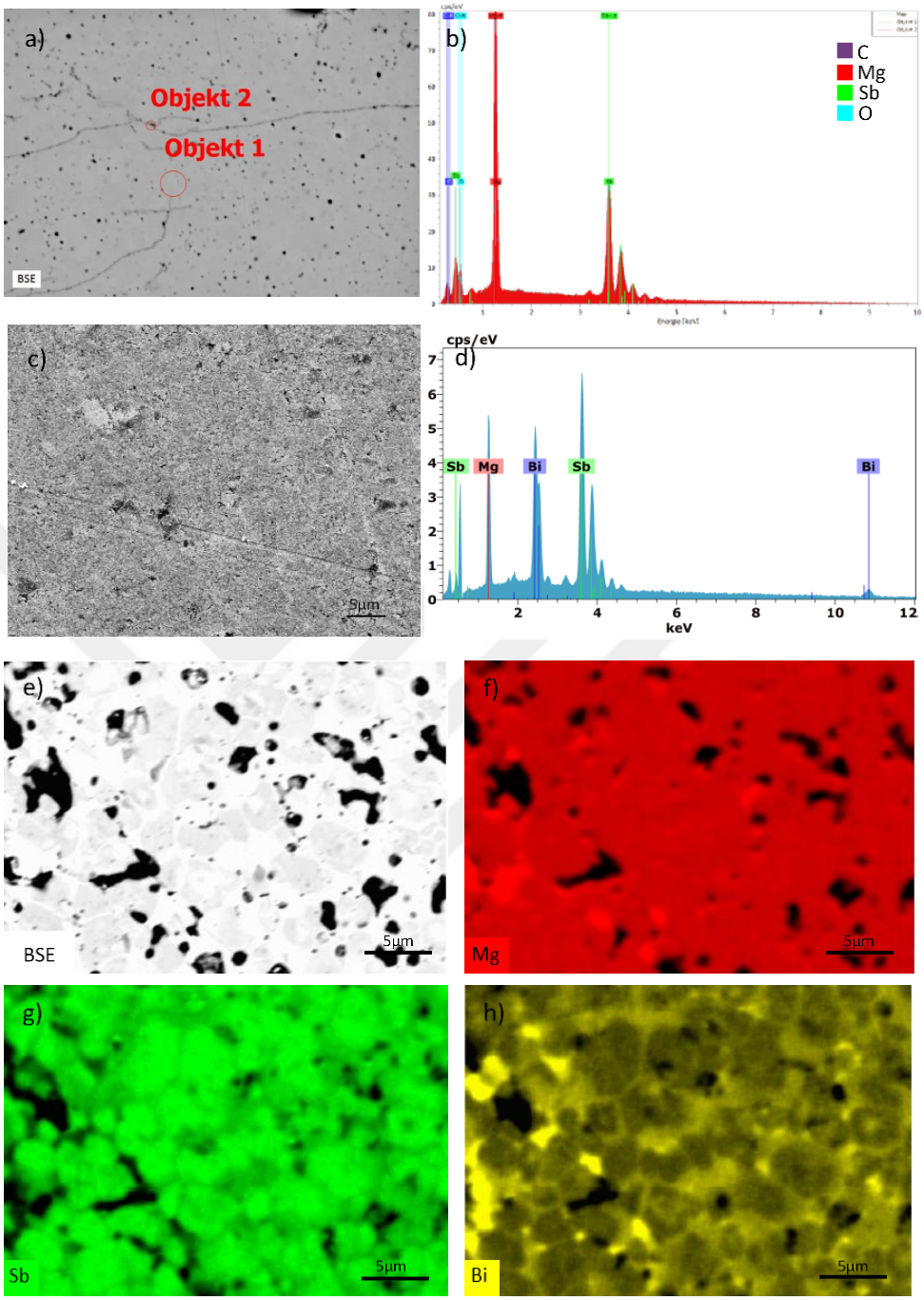

Figure 4.5 SEM images of **a)** $Mg_{3.2}Sb_2$, **c)** $Mg_{3.2}Sb_{1.5}Bi_{0.49}Te_{0.01}$, **e)** centrifuged $Mg_{3.2}Sb_{1.5}Bi_{0.49}Te_{0.01}$with elemental mapping of **f)** Mg, **g)** Sb, **h)** Bi, and EDX analysis of **b)** $Mg_{3.2}Sb_2$, **d)** $Mg_{3.2}Sb_{1.5}Bi_{0.49}Te_{0.01}$

Table 4.4. The WDX analysis results for the sample MO57 ($Mg_{3.2}Sb_{1.5}Bi_{0.49}Te_{0.01}$)

	Atomic Percent	Standard Deviation
Sb	28,809	0,281
Mg	61,572	0,241
Bi	9,398	0,217
Te	0,221	0,006
Total	100	

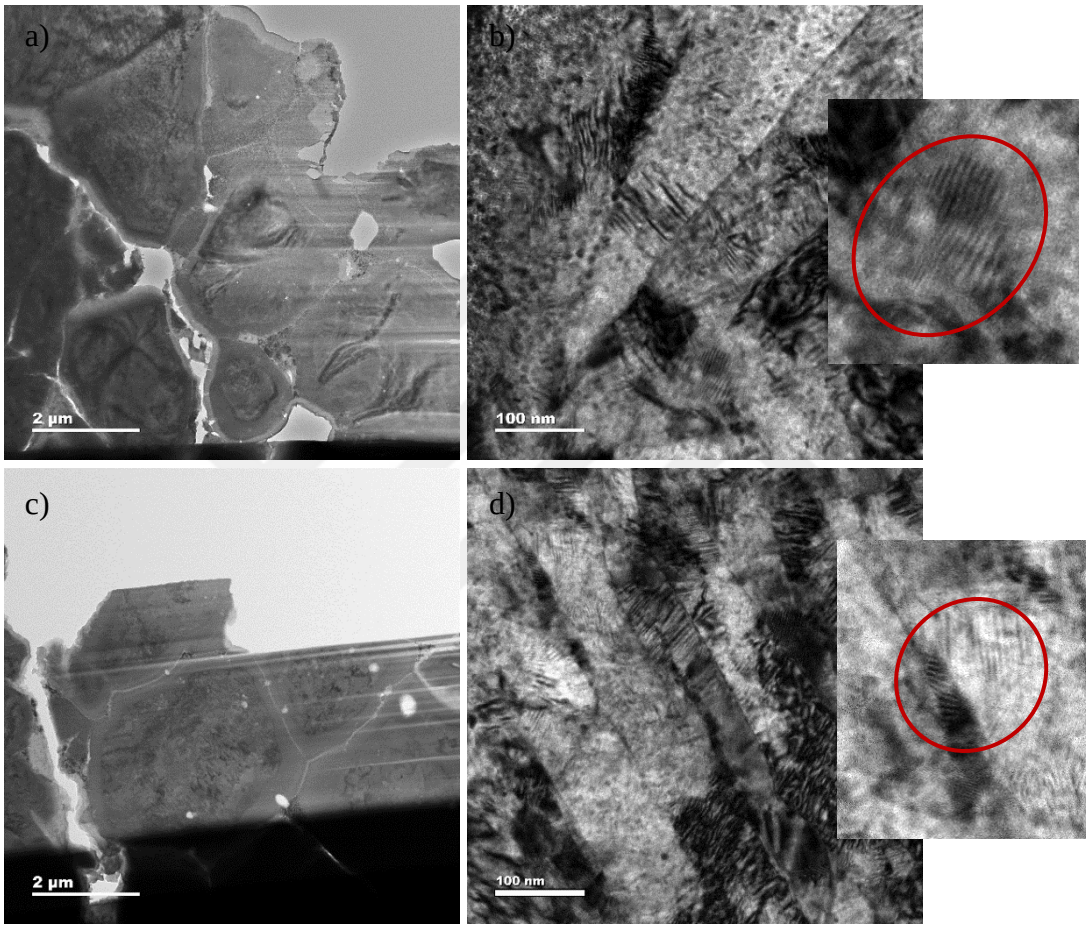

Figure 4.6 TEM images taken from **a, b)** the same direction with sintering direction of centrifuged $Mg_{3.2}Sb_{1.5}Bi_{0.49}Te_{0.01}$, **c, d)** the perpendicular direction to the sintering direction of centrifuged $Mg_{3.2}Sb_{1.5}Bi_{0.49}Te_{0.01}$

In Figure 4.6, TEM images of centrifuged MO70 sample are shown from two different aspects, one from out-plane direction, which is parallel to the sintering direction and the second from the in-plane direction, which is perpendicular to the sintering direction. Since samples were placed in the quartz ampoule vertically, it was expected that liquid eutectic phase would move out from structure through the out-plane direction. Therefore, the microstructure was investigated from both directions. The TEM images display that grain sizes of the sample were around 4 µm similar to the ones in the SEM

images. In Figure 4.6b and 4.6d, distinct ordered grains were observed from both in-plane and out-plane directions due to the centrifugal forces. Also, lattice dislocations within the grains with slightly ordering and dislocation arrays were seen in both in-plane and out-plane direction. Although, the ordered grains and dislocation arrays were more often in the out-plane direction. Since the dislocations generate strain fields and lead to shorter phonon scattering time, introducing lattice dislocations would prevent the propagation of phonons and reduce the lattice thermal conductivity[59, 62, 69, 70].

4.4 Physical Characterizations

Physical property measurements were applied on bulk polycrystalline materials of both centrifuged and non-centrifuged samples.

The stability of $Mg_{3.2}Sb_{1.5}Bi_{0.49}Te_{0.01}$ phase was investigated through DSC-TG measurement until 500°C, since the transport properties were measured until that temperature and optimum thermoelectric properties were observed at 450°C. As displayed in Figure 4.7, $Mg_{3.2}Sb_{1.5}Bi_{0.49}Te_{0.01}$ phase stayed stable until 500°C. TG curve stayed at 100% level and weight change wasn't observed for any temperature range. Also, no peak was detected on the DSC curve regarding to phase transition or decomposition. For thermal conductivity calculations, the specific heat capacity was calculated according to Dulong-Petit law. According to the study of Tamaki et.al, theoretical and experimental c_p values present almost the same value [36]. In this study, c_p value was taken as 0.37 J/gK for thermal conductivity calculations.

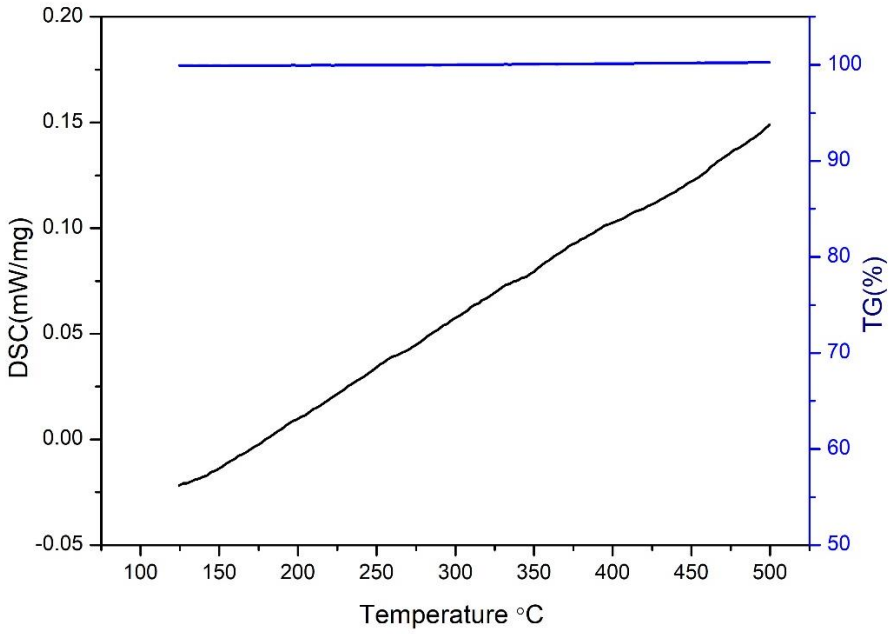

Figure 4.7 DSC-TG analysis of $Mg_{3.2}Sb_{1.5}Bi_{0.49}Te_{0.01}$

All electrical resistivity measurements were carried out from room temperature to 723K (Figure 40). The untreated $Mg_{3.2}Sb_{1.5}Bi_{0.49}Te_{0.01}$ sample displayed a semi-conducting behavior between this temperature range. Only sample MO58 didn't present a usual semi-conducting behavior and compared to other centrifuged samples its resistivity decreased dramatically after the centrifugation process although the large density decrease (Table 4.3). This result might be stemming from the excess Mg. Although the density measurements and XRD results presented that excess amount of Mg was removed from the material, it might still exist in the microstructure slightly higher than the calculated stoichiometry for $Mg_{3.2}Sb_{1.5}Bi_{0.49}Te_{0.01}$ compound. As stated on studies of Imasato et. al and Shuai et al., even the $Mg_{3+x}Sb_{1.5}Bi_{0.49}Te_{0.01}$ stoichiometry can affect the electrical transport properties in a negative way and less Mg amount can provide better transport properties [55, 71]. Thereafter, the excess amount of Mg was added after producing main $Mg_{3.2}Sb_{1.5}Bi_{0.49}Te_{0.01}$ compound, and only milled with the main phase for 30 minutes to be able to remove it more easily. The electrical resistivity of centrifuged MO61 presented similar character with MO57 and it showed that subsequently addition of excess Mg was a better option than adding it as the starting material.

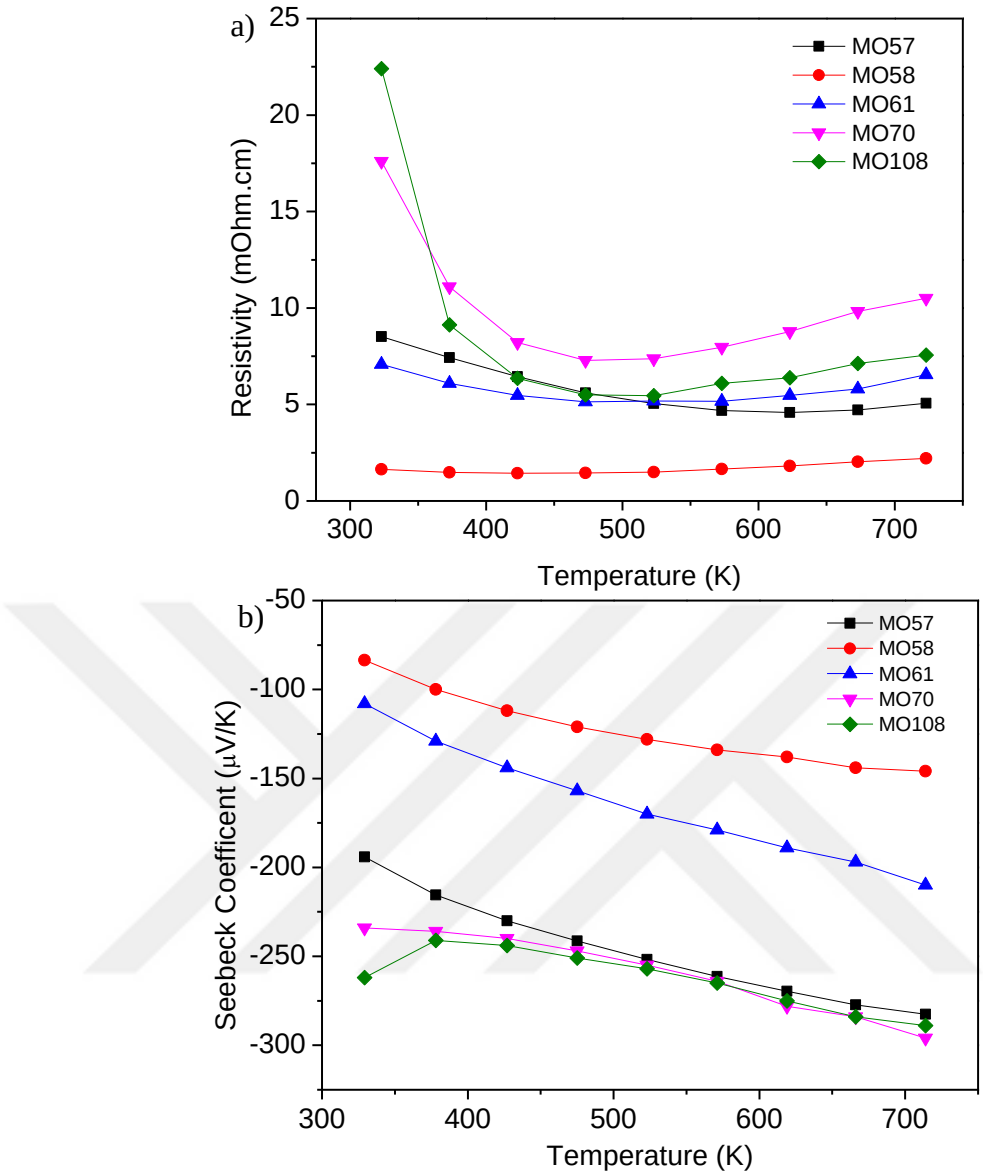

Figure 4.8 a) The electrical resistivity and **b)** Seebeck coefficient of MO57 non-centrifuged (black), MO58 in-situ 10 wt. % excess Mg added centrifuged (red), MO61 subsequently 10 wt. % excess Mg added centrifuged (blue), MO70 subsequently 20 wt. % excess Mg added centrifuged (pink) and MO108 subsequently 20 wt. % excess Mg added centrifuged for an hour (green) $Mg_{3.2}Sb_{1.5}Bi_{0.49}Te_{0.01}$ samples as a function of temperature

For following experimental studies, the effect of the excess amount of Mg and heat treatment time were investigated. 10 wt. % excess amount of Mg addition decreased the electrical resistivity value for the sample MO58. Since the excess amount of Mg was very small, most of them might be trapped in the crystal structure and couldn't be expelled from the microstructure. Therefore, a decrease in electrical resistivity was observed for

MO58. Although, resistivity values of the sample with external addition of the same amount of Mg were similar with the non-centrifuged sample. It might be related to lower Mg concentration in the crystal structure. It proves that it was easier to remove excess Mg after external addition. Thus, the excess amount of Mg was added after synthesis of the main phase for following experiments. By increasing the excess amount of Mg from 10 wt. % to 20 wt. % (MO70), the electrical resistivity highly increased after centrifugation. As it is seen from the phase-diagram (see Figure 2.15), higher amount of Mg would cause an increase in liquid phase at high temperatures (700 and 750 ˚C) and it would be easier to remove Mg from the structure. Therefore, relatively low carrier concentration and higher porosity formation led to this behavior. In addition, since it was claimed by Kanno et.al that increasing the grain-size can enhance the thermoelectric properties, the heat treatment time was extended from 30 minutes to an hour to investigate the grain size increase [72]. As seen from Figure 4.8, with longer heat treatment for lower temperature the resistivity was increased, but overall a significant decrease was observed for sample MO108 compared to MO70. This behavior might be associated with the grain boundary dominated charge transport. As grains and grain boundaries act like two different phases at the grain boundaries the electronic structure of material changes and a potential barrier is generated along the grain boundary resulting in the electrical resistivity increase on grain boundaries [73]. From this point of view, with increased heat treatment time it was expected to have larger grains and smaller amount of grain boundaries, which provides lower electrical resistivity as seen for sample MO108.

Figure 4.8b displays the Seebeck coefficients between 323 – 723 K. The negative sign of the Seebeck coefficients proved that all samples presented n-type behavior even after centrifugation processes. However, MO58 and MO61 had very low Seebeck coefficients compared to the starting composition of $Mg_{3.2}Sb_{1.5}Bi_{0.49}Te_{0.01}$. It might result from the higher number of carrier concentrations related to the Eq. 1.4. These results also promoted the electrical resistivity values of these samples. As discussed above, this outcome could be related to the higher amount of Mg trapped inside the crystal structure during the experiments. On the other hand, with 20 wt. % Mg addition, the Seebeck coefficients of MO70 and MO108 were almost same with non-centrifuged MO57 for most temperature ranges except for 323 and 373 K. These results were also in agreement with the electrical resistivity discussions. Because both electrical resistivity and Seebeck coefficients depend on the carrier concentration, these results supported that the decrease

on resistivity values caused by the microstructure defects rather than the carrier concentration changes due to Mg addition and removal. In addition, the similar Seebeck coefficients of MO70 and MO108 promote the idea of grain boundary dominated charge transport, because, grain boundaries are not much effective on the Seebeck coefficient [73].

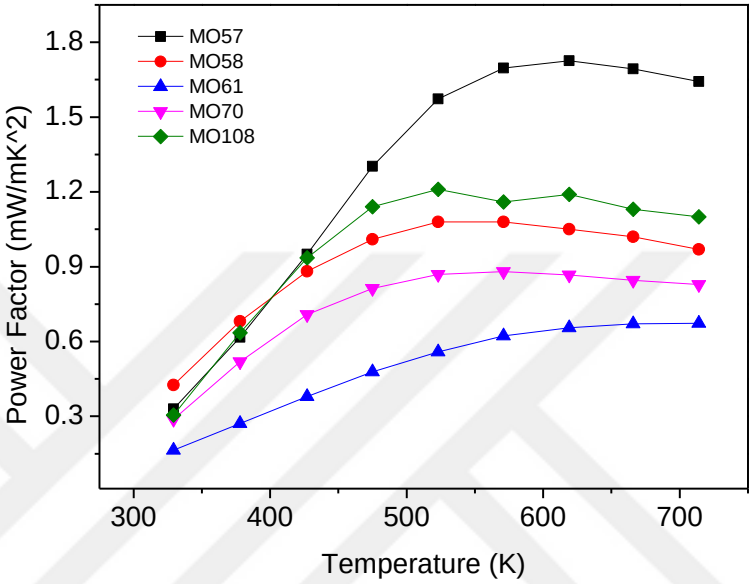

Figure 4.9 Power factor of non-centrifuged (black), in-situ 10 wt. % excess Mg added centrifuged (red), subsequently 10 wt. % excess Mg added centrifuged (blue), subsequently 20 wt. % excess Mg added centrifuged (pink) and subsequently 20 wt. % excess Mg added centrifuged for an hour (green) $Mg_{3.2}Sb_{1.5}Bi_{0.49}Te_{0.01}$ samples as a function of temperature.

By combining the electrical resistivity and Seebeck coefficient results, the measured power factor of materials is given in Figure 4.9. Since the Seebeck coefficients of centrifuged samples were similar with MO57, while the electrical resistivities were started to increase after 573 K, the power factor of MO57 was higher than others after this temperature.

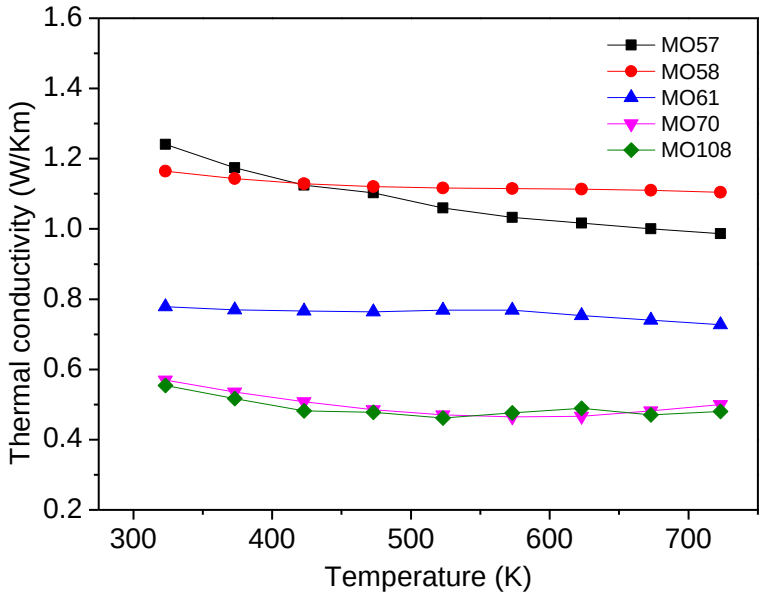

Figure 4.10 The thermal conductivity of non-centrifuged (black), in-situ 10 wt. % excess Mg added centrifuged (red), subsequently 10and 20 wt. % excess Mg added centrifuged (blue and pink), and subsequently 20 wt. % excess Mg added centrifuged for an hour (green) $Mg_{3.2}Sb_{1.5}Bi_{0.49}Te_{0.01}$ samples as a function of temperature

The total thermal conductivities of materials are presented in Figure 4.10. Despite the decrease of the density of MO58 from 4.3 to 3.265, the thermal conductivity showed even higher values for high temperature ranges. Although it was expected to reduce thermal conductivity due to porosities and dislocations, since thermal conductivity both dependent on lattice vibrations and electronic contribution, this behavior might relate to electronic transport properties. As parallel to the resistivity and Seebeck coefficient measurements, due to the increase of charge carrier number, the electronic thermal conductivity might be also much more increased than the decrease of lattice thermal conductivity for the MO58 sample. For MO61 by combining all transport properties, it might be concluded that the defect formations were more effective on the transport properties of MO61 than the charge carrier concentration. As shown in Figure 4.8b, the Seebeck coefficient was decreased significantly for all temperature ranges, which can be related to higher number of carriers, and Figure 4.8a presented similar resistivity values with main composition. By combining these results, it can be claimed that the defects in the microstructure dominated the electrical and thermal conductivity, and led to decrease on total thermal conductivity by creating additional phonon scattering mechanisms. This attitude became more effective for MO70 and MO108 samples. As discussed for the

electrical transport properties of these samples, it was concluded that the carrier concentration of them were lower than the non-centrifuged $Mg_{3.2}Sb_{1.5}Bi_{0.49}Te_{0.01}$ sample. Although MO70 had higher resistivity than MO108, thermal conductivity values were similar. When we compare this two samples centrifuged one at 720°C for 30 min. 750°C for an hour, we observe formation of more amount of homogenously distributed porosity in the latter case. This can be correlated more homogenous grain size distribution with this higher temperature and annealing time. This may imply that although the composition didn't change, grain sizes have increased for the letter sample. Therefore, we should see a decrease in the electrical resistivity. This should result in higher κ_e which might be compensated lower κ_l due to this porosity difference. When the low amount of carrier concentration was paired with the phonon scattering mechanisms coming from the defect structure, total thermal conductivities were decreased even higher than 50% as illustrated on Figure 4.10.

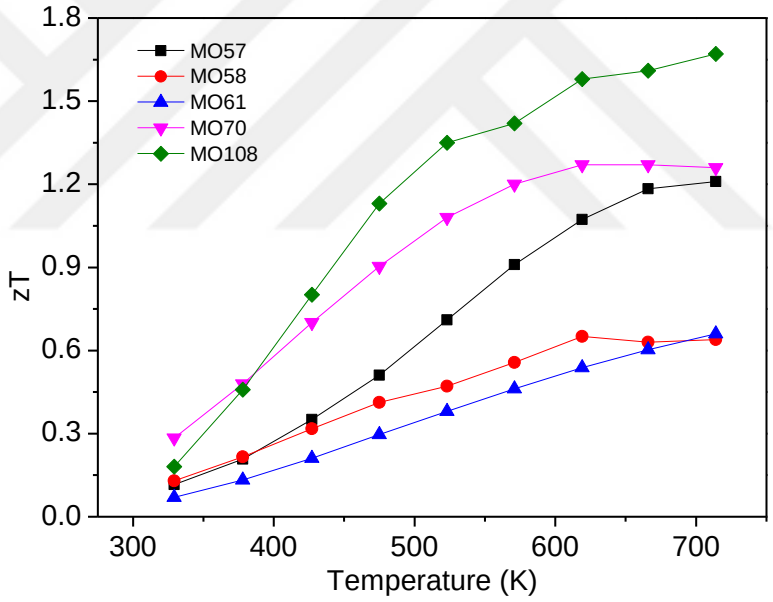

Figure 4.11 The themoelectric figure of merit of non-centrifuged (black), in-situ 10 wt. % excess Mg added centrifuged (red), subsequently 10 wt. % excess Mg added centrifuged (blue), subsequently 20 wt. % excess Mg added centrifuged (pink) and subsequently 20 wt. % excess Mg added centrifuged for an hour (green) $Mg_{3.2}Sb_{1.5}Bi_{0.49}Te_{0.01}$ samples as a function of temperature.

Figure 4.11 gives the thermoelectric figure of merit values for centrifuged and non-centrifuged samples. It was seen that 10 wt. % Mg addition affected the zT value negatively both for in-situ synthesis addition and addition after synthesis of main

composition. As indicated above both power factor decreased, and thermal conductivity increased or not decreased enough to be able to affect overall zT positively. On the other hand, the experiments with 20 wt. % Mg addition were successful and zT values increased for all temperature ranges than main $Mg_{3.2}Sb_{1.5}Bi_{0.49}Te_{0.01}$. Basically, the dramatic reduce of thermal conductivity led to increase in zT values, while sustaining the same Seebeck coefficient and increasing slightly the electrical resistivity. Even with longer heat treatment time, the highest zT of 1.67 was achieved. At the end, around 40% increase was observed for zT values from 1.2 to 1.67. Compared to literature values, zT was increased without changing the carrier concentration around 17 % [36, 45, 48, 55, 71].

Finally, micro-hardness measurements were done from 15 different points for non-centrifuged and centrifuged samples. The marks of Vickers indenter on different samples were presented in Figure 4.12. For the certainty the average values were calculated and given in Table 4.5. MO70 showed even higher Vickers hardness of 98 HV after centrifugation while MO108 presented a high amount of decrease in hardness of 43 HV compared to the hardness of 81 HV of non-centrifuged sample. When Vickers-hardness of the commercial thermoelectric material $Bi_{0.5}Sb_{1.5}Te_3$ is considered, the hardness values of sample 57 and 70 have also close Vickers values to the commercial one [74-77]. Besides, they presented similar hardness properties with calculated hardness value of Mg_3Sb_2 [78].

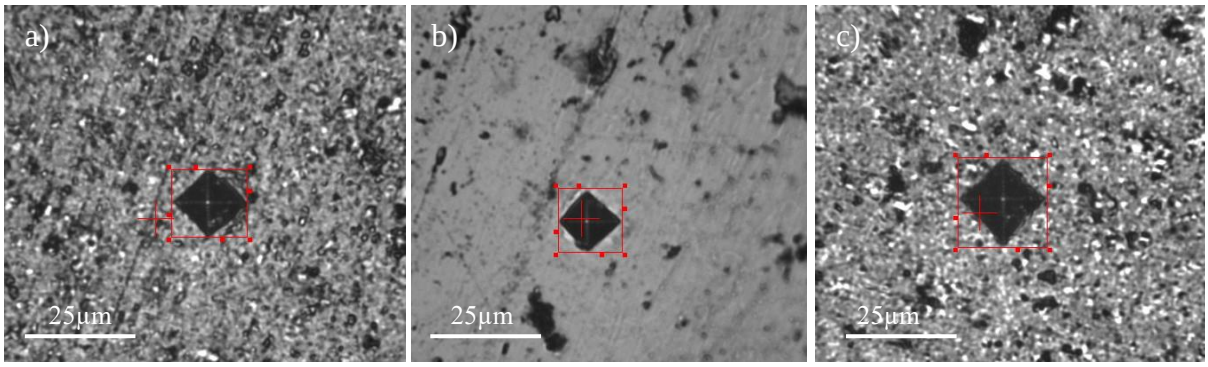

Figure 4.12 Vickers hardness measurement images of **a)** $Mg_{3.2}Sb_{1.5}Bi_{0.49}Te_{0.01}$, **b)** centrifuged sample after 720°C for 30 minutes heat treatment and **c)** centrifuged sample after 750°C for an hour heat treatment

Table 4.5. Vickers hardness values of non-centrifuged and centrifuged samples

	MO57	**MO70**	**MO108**
Hardness (HV)	81	98	43

Chapter 5:

MgB_2 AND B DOPED $Mg_{3.2}Sb_{1.5}Bi_{0.49}Te_{0.01}$

Recently, the positive effects of nano-boron(nB) incorporation have been discovered for different materials [79, 80]. In that part, the effects of MgB_2 and nB incorporation on the thermoelectric and physical properties of $Mg_{3.2}Sb_{1.5}Bi_{0.49}Te_{0.01}$ will be discussed.

5.1 Preparation

The same experimental procedure was used for starting $Mg_{3.2}Sb_{1.5}Bi_{0.49}Te_{0.01}$ compound as described during melt-centrifugation experiments. After subtracting the dark gray $Mg_{3.2}Sb_{1.5}Bi_{0.49}Te_{0.01}$ from the stainless-steel vials, to incorporate MgB_2, nano-boron and carbon coated nano-boron with the main phase, sonication operation was applied. First, 0.3 and 0.5 wt. % MgB_2 and $Mg_{3.2}Sb_{1.5}Bi_{0.49}Te_{0.01}$ were mixed together inside a 50 ml beaker. Then, 10 ml hexane was added, and the mixture was sonicated for 10 minutes in an ultrasonic bath. After sedimentation was observed, the mixture was filtered through the filter paper and black powder was dried for an hour. To produce high density bulk materials the powder was sintered by spark plasma sintering (SPS) at 700°C for 7 minutes under 50 MPa pressure. Same steps were followed during the SPS operation as mentioned in the melt-centrifugation section. For nano-boron and carbon coated nano-boron precipitation in $Mg_{3.2}Sb_{1.5}Bi_{0.49}Te_{0.01}$ compound, 0.3 wt. % nB and CnB were mixed with main compound following the same experimental procedure as MgB_2 experiments. To be able to compare the effects of incorporation, the main $Mg_{3.2}Sb_{1.5}Bi_{0.49}Te_{0.01}$ was also sintered at 700°C for 7 minutes under 50 MPa pressure. The effects of the sintering temperature also observed by applying different sintering temperatures 600, 700 and 800°C, respectively. Table 41. displays the preparation conditions of MgB_2, CnB and nB incorporated samples. Also, samples with different sintering temperatures are given in Table 5.1. Also, samples with different sintering temperatures are given in Table 5.1.

Table 5.1. Preparation conditions of the $Mg_{3.2}Sb_{1.5}Bi_{0.49}Te_{0.01}$ based compounds.

	Composition	Additive material	Milling Time	SPS Temperature	SPS Time (min.)	Sonication Time (min.)
MO57	$Mg_{3.2}Sb_{1.5}Bi_{0.49}Te_{0.01}$	-	2 h	600°C	10	-
MO107	$Mg_{3.2}Sb_{1.5}Bi_{0.49}Te_{0.01}$	-	2 h	800°C	5	-
MO113	$Mg_{3.2}Sb_{1.5}Bi_{0.49}Te_{0.01}$	-	2 h	700°C	7	-
MO97	$Mg_{3.2}Sb_{1.5}Bi_{0.49}Te_{0.01}$	0.3 wt. % MgB_2	2 h	700°C	7	10
MO110	$Mg_{3.2}Sb_{1.5}Bi_{0.49}Te_{0.01}$	0.2 wt. % MgB_2	2 h	700°C	7	10
MO114	$Mg_{3.2}Sb_{1.5}Bi_{0.49}Te_{0.01}$	0.5 wt. % MgB_2	2 h	700°C	7	10
MO115	$Mg_{3.2}Sb_{1.5}Bi_{0.49}Te_{0.01}$	0.3 wt. % nB	2 h	700°C	7	10
MO116	$Mg_{3.2}Sb_{1.5}Bi_{0.49}Te_{0.01}$	0.3 wt. % CnB	2 h	700°C	7	10

5.2 Crystal Structure Characterization

The crystal structure and phases of samples were determined by XRD with Cu-K_α source. Figure 5.1 shows the XRD patterns of sintered $Mg_{3.2}Sb_{1.5}Bi_{0.49}Te_{0.01}$, 0.2, 0.3, 0.5 wt. % MgB_2 and 0.3 wt. % nB and CnB added $Mg_{3.2}Sb_{1.5}Bi_{0.49}Te_{0.01}$ samples.

As seen from Figure 5.1 the XRD patterns presented a match with trigonal Mg_3Sb_2 crystal structure with *P-3m1* space group without containing any impurity peaks. Since the XRD measurements were taken after the sintering processes some of the patterns contain graphite peaks due to the graphite foil covering during the sintering process, as mentioned in melt-centrifugation results. Because the amount of MgB_2, nB, and CnB were very low, they couldn't detect from XRD results.

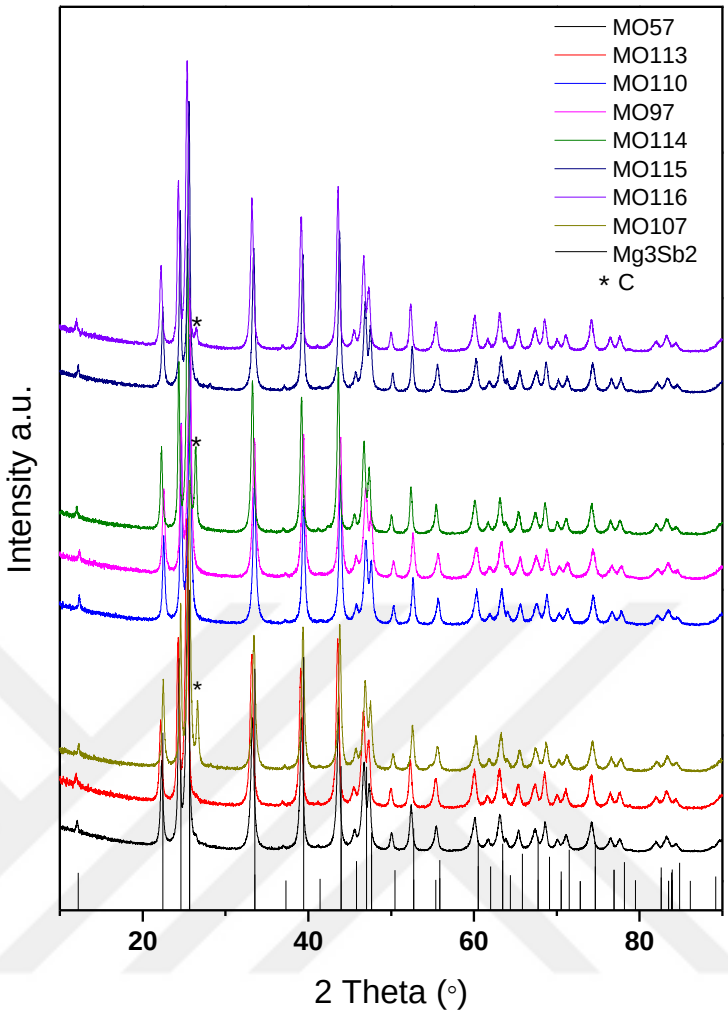

Figure 5.1 XRD patterns of $Mg_{3.2}Sb_2$ (black), 10 wt. % excess Mg added sintered (red) and centrifuged (green) $Mg_{3.2}Sb_2$, 25 wt. % excess Sb added sintered (blue) and centrifuged (dark blue) $Mg_{3.2}Sb_2$, 20 wt. % excess Mg added sintered (pink) and centrifuged (purple) $Mg_{3.2}Sb_2$

The calculated lattice parameters of pure, MgB_2, nB and CnB added phases are presented in Table 5.2. As the radius of B atom is much smaller than Mg atom, it might be placed in interstitial sites between or within the Mg-Sb layers leading to a decrease in cell parameter (a) and increase in cell parameter(c). In other aspect, due to the low solubility of boron atoms they may form a second phase with Mg atoms by creating a Mg vacancy inside the structure which result in a decrease lattice parameter. This result also promotes the supposal of Mg vacancy formation related to second phase formation between Mg and B atoms for boron addition experiments. To make certain, transport properties of these samples will be discussed on next part.

Table 5.2. Lattice parameters (a and c) of trigonal 0.3, 0.4 wt. % MgB_2(MO97 and MO114) and 0.3 wt. % nB and CnB added (MO115 and MO116) $Mg_{3.2}Sb_{1.5}Bi_{0.49}Te_{0.01}$

	a (Å)	c(Å)
MO57	4.582(4)	7.286(7)
MO113	4.605(2)	7.309(5)
MO97	4.582(2)	7.268(5)
MO114	4.596(4)	7.29(1)
MO115	4.5867(7)	7.280(2)
MO116	4.601(2)	7.303(4)

5.3 Chemical and Microstructure Characterization

The calculated densities of materials display high relative densities as given in the Table 5.3. By increasing the sintering temperature relative densities also slightly increased from 95.7 to 97%. Although nB and CnB additions did not change the densities, the MgB_2 addition up to 0.5 wt. % increased densities. Figure 5.2a and b show the SEM images of highly dense 0.2 and 0.3 wt. % MgB_2 added samples which don't contain any pores or cracks in microstructure.

Table 5.3. Density values and relative densities of spark plasma sintered MgB_2, nB and CnB incorporated samples

	MO57	MO113	MO97	MO110	MO114	MO115	MO116
Density (g/cm^3)	4.3	4.367	4.38	4.398	4.34	4.36	4.356
Relative Density %	95.7	97	97.4	97.8	96.6	97	96.9

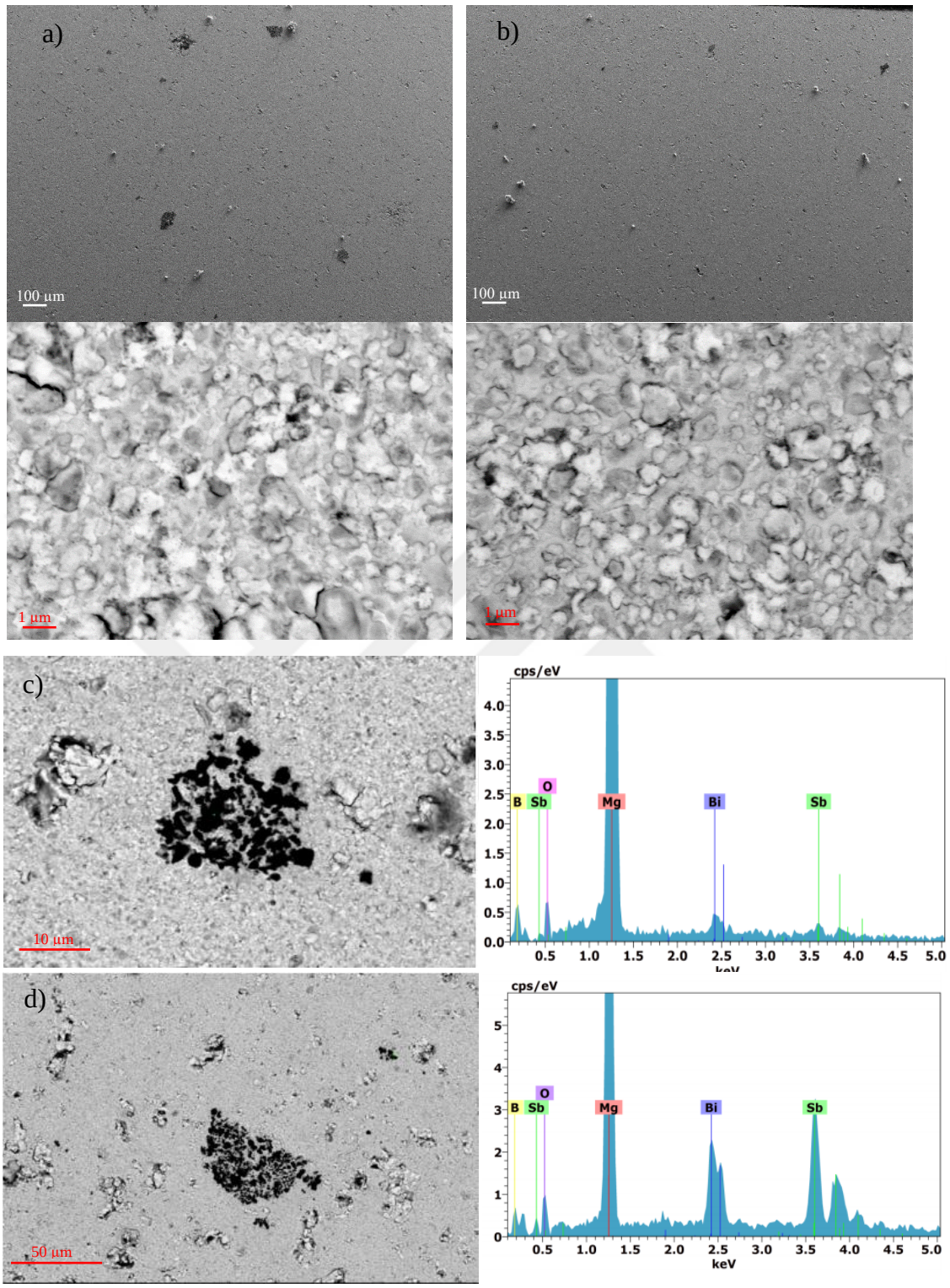

Figure 5.2 a,b) SEM images of 0.2 and 0.3 wt. % MgB_2 incorporated MSBT samples, **c,d)** EDX analyses of dark regions observed on SEM images of 0.2 and 0.3 wt. % MgB_2 incorporated MSBT samples

To clarify the influences of MgB_2 incorporation to the microstructure and morphology scanning electron microscopy was used. In Figure 5.2 c and d, the SEM images display different phases which create a contrast between them, and the EDX analysis spectrum of these darker agglomerated regions in the microstructure of sample 110 and sample 97 respectively. As a result of EDX analysis, the peak positions belong to Mg, Bi, Sb and B elements were determined on darker regions. This confirms that MgB_2 phase is distributed over the microstructure either as small or large grains.

5.4 Physical Property Characterizations

Physical property measurements were applied on bulk polycrystalline $Mg_{3.2}Sb_{1.5}Bi_{0.49}Te_{0.01}$, 0.3, 0.5 wt. % MgB_2 and 0.3 wt. % nB and CnB added $Mg_{3.2}Sb_{1.5}Bi_{0.49}Te_{0.01}$ samples.

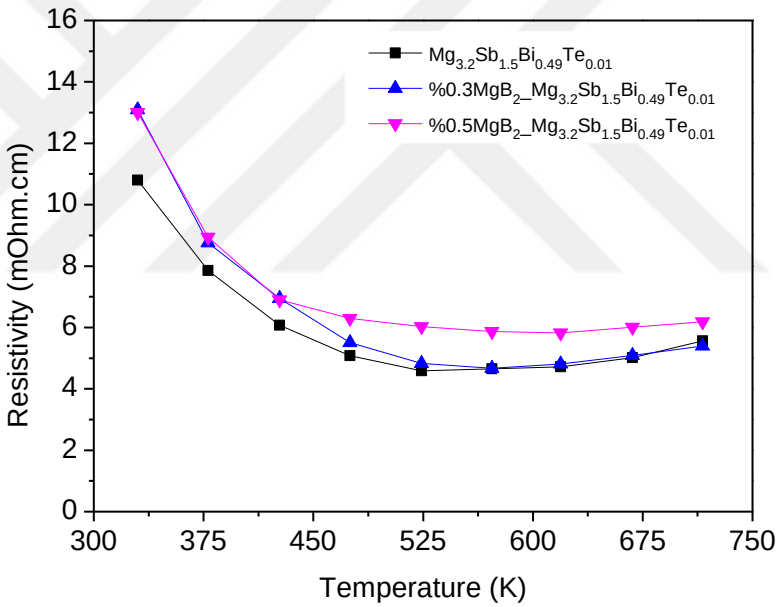

Figure 5.3 The electrical resistivity of 0, 0.3 and 0.5 wt. % MgB_2 (MO113, MO97 and MO114, respectively) added $Mg_{3.2}Sb_{1.5}Bi_{0.49}Te_{0.01}$ samples as a function of temperature

All resistivity values decrease with increasing temperature until 570K, at higher temperatures they tend to increase resistivities as presented in Figure 5.3. This behavior showed that materials had semiconducting properties up to 570 K, then their characters changed to active metallic behavior. While MgB_2 additions affected the resistivity values strongly, at elevated temperature the influence of addition decreased. Only 0.5 wt. %

addition had higher effect at higher temperatures. The reason of that increase might depend on either lower carrier concentration due to the Mg vacancy formation as discussed above, or inclusion of second phases as seen Figure 5.2 c and d.

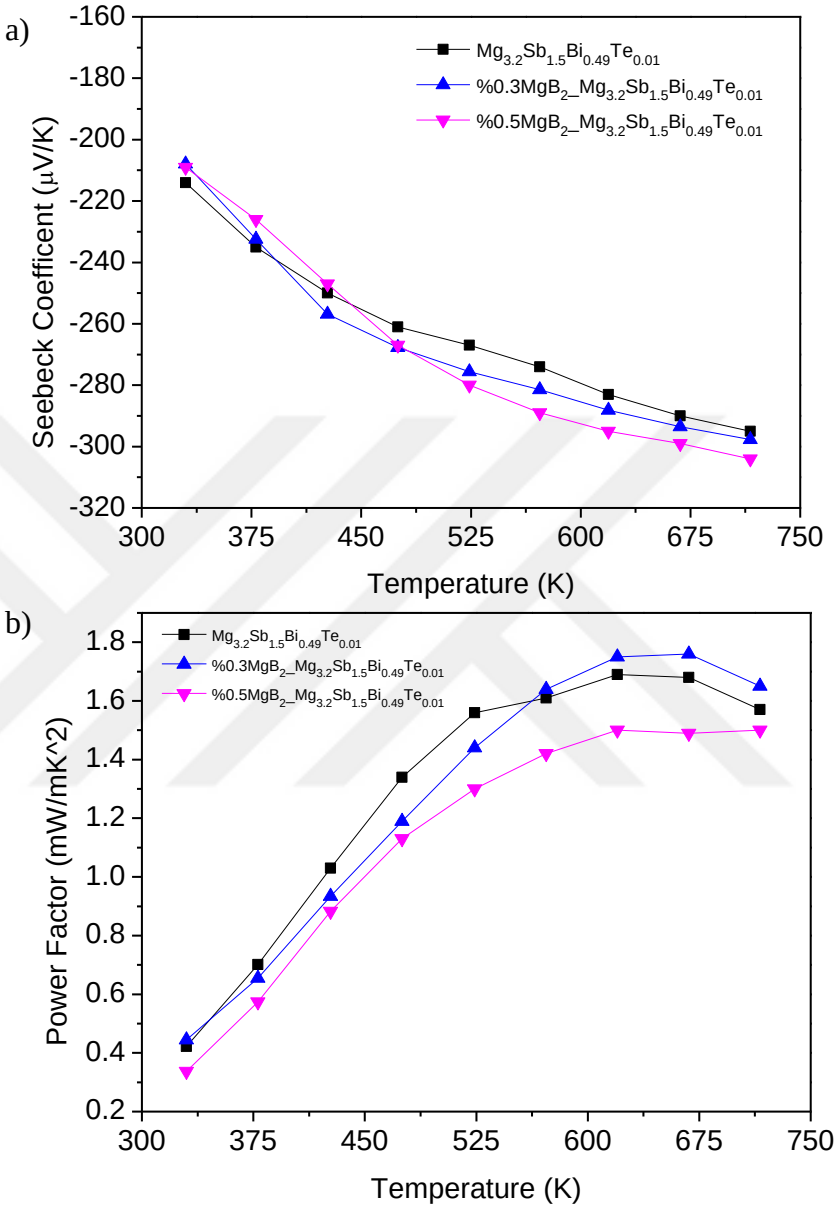

Figure 5.4 a) The Seebeck coefficient and **b)** power factor of 0, 0.3 and 0.5 wt. % MgB_2 (MO113, MO97 and MO114, respectively) added $Mg_{3.2}Sb_{1.5}Bi_{0.49}Te_{0.01}$ samples as a function of temperature

Figure 5.4a presents the Seebeck coefficients were negative for all samples mean that electrons were the charge carriers and MgB_2 didn't change the n-type character of materials. After MgB_2 addition, the Seebeck values increased slightly. Overall these small deviations are not significant considering the measurement accuracies. As given in Eq.

1.4., Seebeck coefficient increases with the decrease of carrier concentration. Therefore, the increase of Seebeck coefficients can be explained in terms of Mg amount in the structure. Since at 700°C sintering temperature the molten Mg tend to diffuse trough Mg deficient MgB_2, it may reduce the carrier concentration [68]. Figure 5.4b shows the power factors of samples. Until 570K all MgB_2 added samples had lower power factors than main phase, after that temperature 0.3 wt. % addition slightly increased power factor because of the same resistivity and slightly higher Seebeck coefficient.

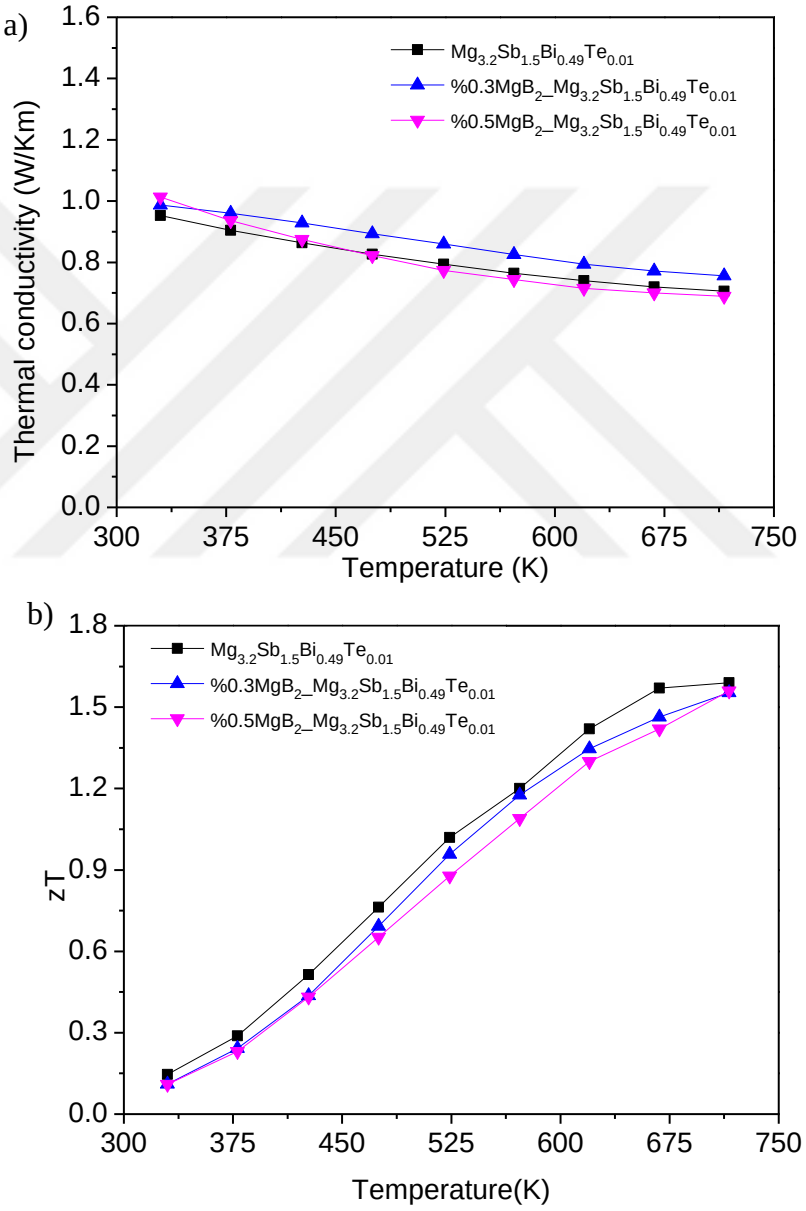

Figure 5.5 a) Thermal conductivities and **b)** zT values of 0, 0.3 and 0.5 wt. % MgB_2 (MO113, MO97 and MO114, respectively) added $Mg_{3.2}Sb_{1.5}Bi_{0.49}Te_{0.01}$ samples as a function of temperature.

Thermal conductivities of materials didn't change within the accuracy of the measurements as presented in Figure 5.5a. As a result, when all transport properties were combined the calculated zT values are given in Figure 5.5b. The highest zT 1.59 was achieved for the main $Mg_{3.2}Sb_{1.5}Bi_{0.49}Te_{0.01}$ compound sintered at 700°C(MO113). For 0.3 and 0.5 wt. % additions similar zT values 1.55 and 1.56 with main compound were obtained. Overall, MgB_2 addition didn't change the transport properties significantly and lead to overall enhancement in zT.

Furthermore, the effects of sintering temperature, and CnB and nB additions on the physical properties of $Mg_{3.2}Sb_{1.5}Bi_{0.49}Te_{0.01}$ were investigated. Because high sintering temperature 800°C caused a huge change on transport properties due to high amount of Mg lost, they weren't discussed with other samples (see appendix Figure A.4.). As given in the Figure 5.6a, while increase in sintering temperature from 600°C to 700°C didn't change resistivity value except for room temperature, the Seebeck coefficient was increased for all temperature ranges (Figure 5.6b). That kind of attitude might be related to the carrier concentration changes regarding to higher sintering temperature than the melting point of Mg. Besides, to be able to determine the reasons behind these certainly, Hall measurements are necessary. The unchanged resistivity value might be related to lower carrier concentration and higher mobility combination. Through nB and CnB additions, resistivity values and Seebeck coefficients were increased considerably. That parallelism on transport properties might support that the reason behind these values arisen from the decrease of carrier concentration. Since at higher temperatures molten Mg tends to diffuse to boron as discussed during MgB_2 results[81]. Because CnB was covered by carbon layer, the diffusion of Mg atoms through carbon coated nano boron was more difficult than nano-boron. Therefore, higher increases on resistivity and Seebeck coefficient were observed for nB addition than CnB addition.

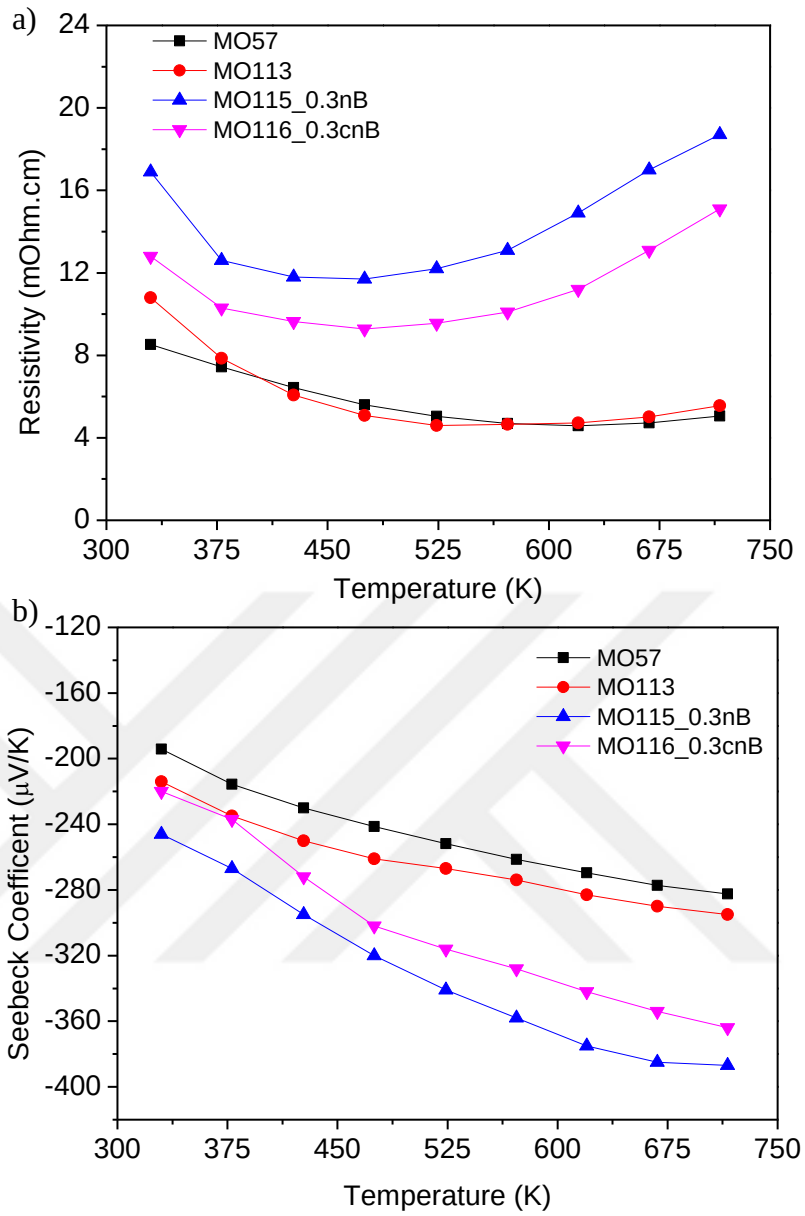

Figure 5.6 a) The resistivity and **b)** Seebeck coefficient of $Mg_{3.2}Sb_{1.5}Bi_{0.49}Te_{0.01}$ samples (sintered at 600°C(black), sintered at 700°C(red), with addition of 0.3 wt. % nB(blue) and 0.3 wt. % CnB(pink)) as a function of temperature

Total thermal conductivities of differently treated $Mg_{3.2}Sb_{1.5}Bi_{0.49}Te_{0.01}$ samples were presented in Figure 5.7. In the same way as resistivity results, both CnB and nB additions led to a significant decrease of thermal conductivities. However, while resistivity values were dependent on carbon coating, thermal conductivity values were almost same for CnB and nB additions. Since thermal conductivity depends on both electronic and lattice contribution, it might be claimed that in this case lattice thermal conductivity reduction acted as dominant part. Also, sintering process at 700°C caused a considerable decrease

on total thermal conductivity from 0.98 to 0.7 W/Km at 723K. One possible reason for the difference observed in thermal conductivity of samples sintered at 700°C and 600°C can be related to microstructural dislocations introduced during the SPS treatment under vacuum. Especially at 700°C due to the higher vapor pressure of Mg the possibility to form microstructural dislocations is considered to be higher. As this Mg is not the one in the crystal structure but in the microstructure, this should not result in any change in the resistivity and Seebeck coefficient but should decrease the thermal conductivity.

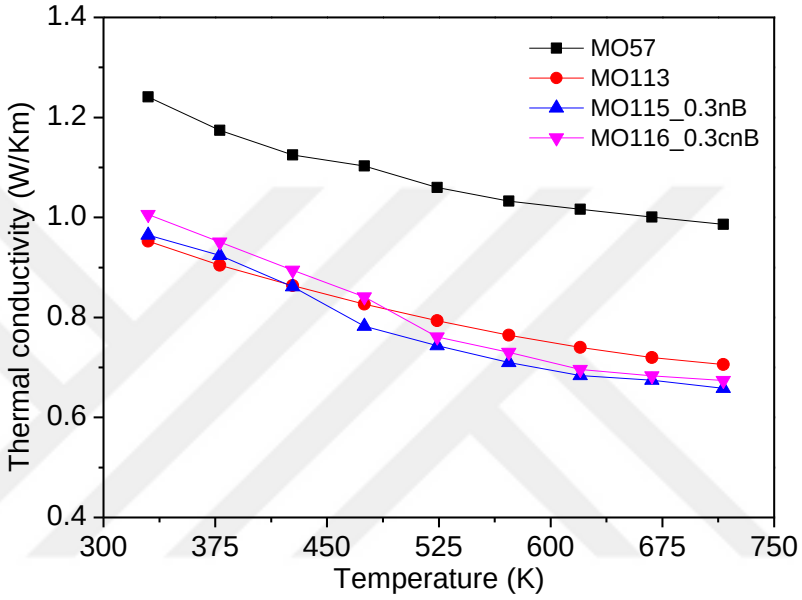

Figure 5.7 The total thermal conductivities of $Mg_{3.2}Sb_{1.5}Bi_{0.49}Te_{0.01}$ samples (sintered at 600°C(black), sintered at 700°C(red), with addition of 0.3 wt. % nB(blue) and 0.3 wt. % CnB(pink)) as a function of temperature

Thermoelectric figure of merit values of samples is given in Figure 5.8. It is seen that the zT value of $Mg_{3.2}Sb_{1.5}Bi_{0.49}Te_{0.01}$ was increased for all temperature ranges by increasing sintering temperature from 600 to 700°C, due to the thermal conductivity reduction. The maximum zT was increased around 32% from 1.2 to 1.59. zT values of nB and CnB added samples presents smaller values than the zT value before additions. Since boron additions highly increased the resistivity values and thermal conductivity is similar to thermal conductivity of MO113, the increase of Seebeck coefficient was not enough to derive better zT values.

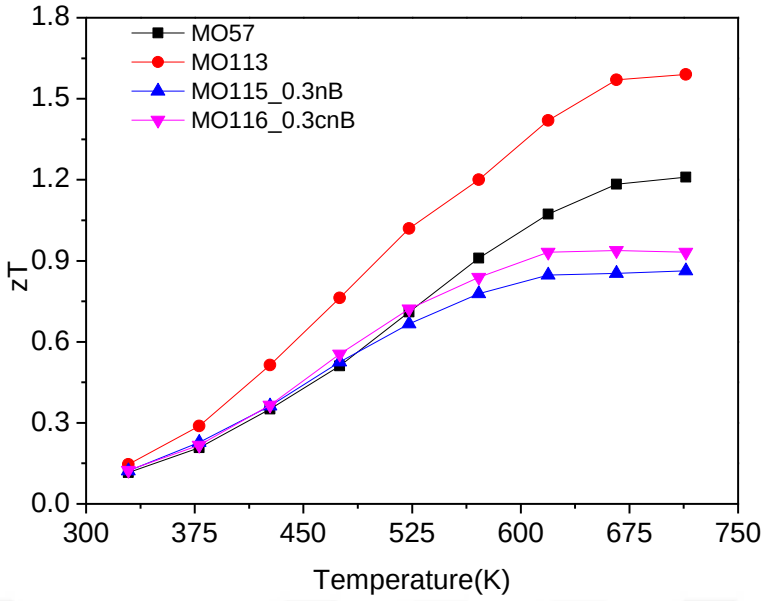

Figure 5.8 zT values of $Mg_{3.2}Sb_{1.5}Bi_{0.49}Te_{0.01}$ samples (sintered at 600°C(black), sintered at 700°C(red), with addition of 0.3 wt. % nB(blue) and 0.3 wt. % CnB(pink)) as a function of temperature

Chapter 6:
CONCLUSION

In this thesis optimization of thermoelectric properties of Mg_3Sb_2 based materials were studied. Considering the promising thermoelectric properties of n-type $Mg_{3.2}Sb_{1.5}Bi_{0.49}Te_{0.01}$, the centrifugation and incorporation of MgB_2, CnB and nB processes were applied to mainly in this composition. A new strategy of melt-centrifugation was implemented to the main compound, which succeeded to improve thermoelectric properties by decreasing thermal conductivity. A well-known superconductor MgB_2 which has also low resistivity of 12 μohm.cm at room temperature was selected to incorporate around grain boundaries and create phonon scattering sources without affecting resistivity much as thermal conductivity [68]. Also, CnB and nB incorporations around grain boundaries were aimed, due to their proved positive effects on thermoelectric and mechanical properties.

In the first experimental design, the applicability of melt-centrifugation technique on both n-type and p-type Mg_3Sb_2 was investigated. After findings of unsuccessful results of Sb excess p-type Mg_3Sb_2 experiments, further studies were focused on improving transport properties of n-type $Mg_{3.2}Sb_{1.5}Bi_{0.49}Te_{0.01}$ compound. TEM and SEM images indicated that by implementing centrifugation the liquid phase was successfully removed from the structure by creating dislocations and porous structure. The effects of the Mg addition sequence and the amount of excess Mg were investigated. As a result, it is found that 10 wt. % Mg addition affected electronic transport properties negatively and decreased the power factor. On the other hand, 20 wt. % Mg addition resulted in a high reduction of thermal conductivity without affecting the carrier concentrations of samples. A small increase of resistivity also observed due to the pore formation. Finally, higher zT values were achieved for all temperature ranges for MO70. Following, the effect of heat treatment time and temperature were examined. By applying heat treatment at 750°C for an hour electronic transport property was enhanced compared to heat treatment at 720°C for 30 minutes. Total thermal conductivity was reduced 51% from 0.98 to 0.48W/Km and the highest zT increased from 1.2 to 1.67.

Secondly, CnB, nB and MgB_2 incorporated $Mg_{3.2}Sb_{1.5}Bi_{0.49}Te_{0.01}$ compounds were produced without observing any impurity peaks in XRD patterns. SEM images showed that MgB_2 additions generally agglomerated at specific regions rather than grain

boundaries. The physical properties were investigated through LFA and ZEM-3 analysis. Resistivities and Seebeck coefficients were found higher for CnB and nB incorporated samples. That might happen due to the high sintering temperature and high vapor pressure of Mg. After sintering processes interstitial Mg might diffuse to boron and led to a decrease of carrier concentration. Eventually, much lower zT values were obtained from CnB and nB incorporated samples. However, MgB_2 additions didn't change the overall transport properties.

Finally, the effect of the sintering temperature was investigated by the sintering same composition at 600°C, 700°C and 800°C. Sample sintered at 800°C showed a dramatic increase of resistivity and the sign of Seebeck coefficients was changing by temperature. Probably, much higher applied temperature than the melting point of Mg caused lots of Mg vacancies inside the structure. Compared to 600°C, zT value was increased from 1.2 to 1.59 for the sample sintered at 700°C. Transport properties showed that higher sintering temperature resulted in lower thermal conductivities with similar power factor values for all temperatures.

Consequently, incorporation experiments through CnB, nB and MgB_2 didn't provide an enhancement for thermoelectric properties. It was obvious that increased sintering temperature at 700 °C resulted in 30% enhancement in *zT* value. Besides, melt centrifugation technique was successfully applied to $Mg_{3.2}Sb_{1.5}Bi_{0.49}Te_{0.01}$ compound for the first time and worked out with creation of dislocation arrays in addition to the porous structure. Due to the lower relative density values around 85%, lighter materials were produced and overall *zT* value was increased from 1.2 to 1.67 with a 40% enhancement. Therefore, these materials may be potentially used in a variety of applications, where light weight is deserved. As an example, the thermoelectric modules which are used in vehicle exhaust outlets significantly requires a specific design which their weight should be light to reduce overall fuel consumption. Further, the successfully implemented melt-centrifugation method can also be applied for other research areas such as adsorbent, gas capture (CO_2, H_2O, SO_2), catalysts, which may require micro-structural porosity.

BIBLIOGRAPHY

[1] S. Twaha, J. Zhu, Y. Yan, and B. Li, "A comprehensive review of thermoelectric technology: Materials, applications, modelling and performance improvement," *Renewable and sustainable energy reviews,* vol. 65, pp. 698-726, 2016.

[2] P. Aranguren, M. Araiz, D. Astrain, and A. Martínez, "Thermoelectric generators for waste heat harvesting: A computational and experimental approach," *Energy Conversion and Management,* vol. 148, pp. 680-691, 2017.

[3] J.-P. Fleurial, "Thermoelectric power generation materials: Technology and application opportunities," *Jom,* vol. 61, no. 4, pp. 79-85, 2009.

[4] D. Ji *et al.,* "Thermoelectric generation for waste heat recovery: Application of a system level design optimization approach via Taguchi method," *Energy conversion and management,* vol. 172, pp. 507-516, 2018.

[5] M. Papapetrou, G. Kosmadakis, A. Cipollina, U. La Commare, and G. Micale, "Industrial waste heat: Estimation of the technically available resource in the EU per industrial sector, temperature level and country," *Applied Thermal Engineering,* vol. 138, pp. 207-216, 2018.

[6] Z.-G. Chen, G. Han, L. Yang, L. Cheng, and J. Zou, "Nanostructured thermoelectric materials: Current research and future challenge," *Progress in Natural Science: Materials International,* vol. 22, no. 6, pp. 535-549, 2012.

[7] H. J. Goldsmid, *Introduction to thermoelectricity*. Springer, 2010.

[8] X. Zhang and L.-D. Zhao, "Thermoelectric materials: Energy conversion between heat and electricity," *Journal of Materiomics,* vol. 1, no. 2, pp. 92-105, 2015.

[9] T. M. Tritt, "Thermoelectric phenomena, materials, and applications," *Annual review of materials research,* vol. 41, pp. 433-448, 2011.

[10] I. Terasaki, "Thermal Conductivity and Thermoelectric Power of Semiconductors," in *Reference Module in Materials Science and Materials Engineering*: Elsevier, 2016.

[11] G. J. Snyder and E. S. Toberer, "Complex thermoelectric materials," in *Materials For Sustainable Energy: A Collection of Peer-Reviewed Research and Review Articles from Nature Publishing Group*: World Scientific, 2011, pp. 101-110.

[12] L. E. Bell, "Cooling, heating, generating power, and recovering waste heat with thermoelectric systems," *Science,* vol. 321, no. 5895, pp. 1457-1461, 2008.

[13] J. He and T. M. Tritt, "Advances in thermoelectric materials research: Looking back and moving forward," *Science,* vol. 357, no. 6358, p. eaak9997, 2017.

[14] L.-D. Zhao *et al.,* "Ultralow thermal conductivity and high thermoelectric figure of merit in SnSe crystals," *Nature,* vol. 508, no. 7496, p. 373, 2014.

[15] D. Paul, "Thermoelectric energy harvesting," *ICT-Energy-Concepts Towards Zero-Power Information and Communication Technology. InTech,* vol. 20, p. 21, 2014.

[16] X. Shi, L. Chen, and C. Uher, "Recent advances in high-performance bulk thermoelectric materials," *International Materials Reviews,* vol. 61, no. 6, pp. 379-415, 2016.

[17] J. R. Sootsman, D. Y. Chung, and M. G. Kanatzidis, "New and old concepts in thermoelectric materials," *Angewandte Chemie International Edition,* vol. 48, no. 46, pp. 8616-8639, 2009.

[18] A. da Rosa, "Chapter 5 - Thermoelectricity," in *Fundamentals of Renewable Energy Processes (Third Edition)*, A. da Rosa, Ed. Boston: Academic Press, 2013, pp. 149-212.

[19] R. Taherian and A. Kausar, *Electrical Conductivity in Polymer-Based Composites: Experiments, Modelling, and Applications*. William Andrew, 2018.

[20] E. Maciá, *Thermoelectric materials: advances and applications*. Jenny Stanford Publishing, 2015.

[21] J. R. Christman, J. R. Christman, J. R. Christman, J. R. Christman, and E.-U. Physicien, *Fundamentals of solid state physics*. Wiley New York, 1988.

[22] J. Hook and H. Hall, "Solid state physics 2nd Edition," ed: John Wiley & Sons Ltd, 2001.

[23] C. J. Vineis, A. Shakouri, A. Majumdar, and M. G. Kanatzidis, "Nanostructured thermoelectrics: big efficiency gains from small features," *Advanced Materials,* vol. 22, no. 36, pp. 3970-3980, 2010.

[24] O. Janka and S. M. Kauzlarich, "Zintl Compounds," *Encyclopedia of Inorganic and Bioinorganic Chemistry,* pp. 1-14, 2011.

[25] U. Müller, *Inorganic structural chemistry* (no. 04; QD151. 2, M8.). New York, 1993.

[26] S. M. Kauzlarich, S. R. Brown, and G. J. Snyder, "Zintl phases for thermoelectric devices," *Dalton Transactions,* no. 21, pp. 2099-2107, 2007.

[27] K.-F. Liu and S.-Q. Xia, "Recent progresses on thermoelectric Zintl phases: Structures, materials and optimization," *Journal of Solid State Chemistry,* vol. 270, pp. 252-264, 2019.

[28] C. Yu *et al.*, "Improved thermoelectric performance in the Zintl phase compounds Yb Zn 2− x Mn x Sb 2 via isoelectronic substitution in the anionic framework," *Journal of Applied Physics,* vol. 104, no. 1, p. 013705, 2008.

[29] N. Kazem and S. M. Kauzlarich, "Thermoelectric properties of Zintl antimonides," in *Handbook on the Physics and Chemistry of Rare Earths*, vol. 50: Elsevier, 2016, pp. 177-208.

[30] F. Gascoin, S. Ottensmann, D. Stark, S. M. Haïle, and G. J. Snyder, "Zintl phases as thermoelectric materials: tuned transport properties of the compounds CaxYb1–xZn2Sb2," *Advanced Functional Materials,* vol. 15, no. 11, pp. 1860-1864, 2005.

[31] S. R. Brown, S. M. Kauzlarich, F. Gascoin, and G. J. Snyder, "Yb14MnSb11: New high efficiency thermoelectric material for power generation," *Chemistry of materials,* vol. 18, no. 7, pp. 1873-1877, 2006.

[32] J. Shuai, J. Mao, S. Song, Q. Zhang, G. Chen, and Z. Ren, "Recent progress and future challenges on thermoelectric Zintl materials," *Materials Today Physics,* vol. 1, pp. 74-95, 2017.

[33] Y. L. Yan, Y. X. Wang, and G. B. Zhang, "Electronic structure and thermoelectric performance of Zintl compound Ca 5 Ga 2 As 6," *Journal of Materials Chemistry,* vol. 22, no. 38, pp. 20284-20290, 2012.

[34] E. S. Toberer, P. Rauwel, S. Gariel, J. Taftø, and G. J. Snyder, "Composition and the thermoelectric performance of β-Zn4Sb3," *Journal of materials chemistry,* vol. 20, no. 44, pp. 9877-9885, 2010.

[35] U. Aydemir, A. Zevalkink, A. Ormeci, Z. M. Gibbs, S. Bux, and G. J. Snyder, "Thermoelectric enhancement in BaGa2Sb2 by Zn doping," *Chemistry of Materials,* vol. 27, no. 5, pp. 1622-1630, 2015.

[36] H. Tamaki, H. K. Sato, and T. Kanno, "Isotropic Conduction Network and Defect Chemistry in Mg3+ δSb2-Based Layered Zintl Compounds with High Thermoelectric Performance," *Advanced Materials,* vol. 28, no. 46, pp. 10182-10187, 2016.

[37] C. L. Condron, S. M. Kauzlarich, F. Gascoin, and G. J. Snyder, "Thermoelectric properties and microstructure of Mg3Sb2," *Journal of Solid State Chemistry,* vol. 179, no. 8, pp. 2252-2257, 2006.

[38] B. R. Ortiz *et al.*, "Potential for high thermoelectric performance in n-type Zintl compounds: a case study of Ba doped KAlSb 4," *Journal of Materials Chemistry A,* vol. 5, no. 8, pp. 4036-4046, 2017.

[39] X. Tan, G.-Q. Liu, H. Hu, H. Shao, J. Xu, and J. Jiang, "Band engineering and crystal field screening in thermoelectric Mg 3 Sb 2," *Journal of Materials Chemistry A,* vol. 7, no. 15, pp. 8922-8928, 2019.

[40] X. Shi, X. Wang, W. Li, and Y. Pei, "Advances in Thermoelectric Mg3Sb2 and Its Derivatives," *Small Methods,* vol. 2, no. 10, p. 1800022, 2018.

[41] X. Sun *et al.*, "Achieving band convergence by tuning the bonding ionicity in n-type Mg3Sb2," *Journal of computational chemistry,* vol. 40, no. 18, pp. 1693-1700, 2019.

[42] B. Xu *et al.*, "The Relation between the Electronic Structure and Thermoelectric Properties for Zintl Compounds Mg3Sb2," *Journal of the Physical Society of Japan,* vol. 86, no. 2, p. 024601, 2017.

[43] J. Zhang, L. Song, and B. B. Iversen, "Insights into the design of thermoelectric Mg 3 Sb 2 and its analogs by combining theory and experiment," *Npj Computational Materials,* vol. 5, no. 1, p. 76, 2019.

[44] J. Zhang, L. Song, A. Mamakhel, M. R. V. Jørgensen, and B. B. Iversen, "High-performance low-cost n-type Se-doped Mg3Sb2-based Zintl compounds for

thermoelectric application," *Chemistry of Materials,* vol. 29, no. 12, pp. 5371-5383, 2017.

[45] S. Ohno *et al.*, "Phase boundary mapping to obtain n-type Mg3Sb2-based thermoelectrics," *Joule,* vol. 2, no. 1, pp. 141-154, 2018.

[46] J. Zhang *et al.*, "Designing high-performance layered thermoelectric materials through orbital engineering," *Nature communications,* vol. 7, p. 10892, 2016.

[47] K. Imasato, S. D. Kang, and G. J. Snyder, "Exceptional thermoelectric performance in Mg 3 Sb 0.6 Bi 1.4 for low-grade waste heat recovery," *Energy & Environmental Science,* vol. 12, no. 3, pp. 965-971, 2019.

[48] J. Mao *et al.*, "Manipulation of ionized impurity scattering for achieving high thermoelectric performance in n-type Mg3Sb2-based materials," *Proceedings of the National Academy of Sciences,* vol. 114, no. 40, pp. 10548-10553, 2017.

[49] X. Chen *et al.*, "Extraordinary thermoelectric performance in n-type manganese doped Mg3Sb2 Zintl: High band degeneracy, tuned carrier scattering mechanism and hierarchical microstructure," *Nano Energy,* vol. 52, pp. 246-255, 2018.

[50] P. Gorai, E. S. Toberer, and V. Stevanović, "Effective n-type doping of Mg 3 Sb 2 with group-3 elements," *Journal of Applied Physics,* vol. 125, no. 2, p. 025105, 2019.

[51] P. Gorai, B. R. Ortiz, E. S. Toberer, and V. Stevanović, "Investigation of n-type doping strategies for Mg 3 Sb 2," *Journal of Materials Chemistry A,* vol. 6, no. 28, pp. 13806-13815, 2018.

[52] J. Li *et al.*, "Defect Chemistry for N-Type Doping of Mg3Sb2-Based Thermoelectric Materials," *The Journal of Physical Chemistry C,* vol. 123, no. 34, pp. 20781-20788, 2019.

[53] Y. Wang, X. Zhang, Y. Wang, H. Liu, and J. Zhang, "Enhanced Thermoelectric Properties of n-type Mg3Sb2 by Excess Magnesium and Tellurium Doping," *physica status solidi (a),* vol. 216, no. 6, p. 1800811, 2019.

[54] K. Imasato, S. D. Kang, S. Ohno, and G. J. Snyder, "Band engineering in Mg 3 Sb 2 by alloying with Mg 3 Bi 2 for enhanced thermoelectric performance," *Materials Horizons,* vol. 5, no. 1, pp. 59-64, 2018.

[55] K. Imasato, S. Ohno, S. D. Kang, and G. J. Snyder, "Improving the thermoelectric performance in Mg3+ x Sb1. 5Bi0. 49Te0. 01 by reducing excess Mg," *APL Materials,* vol. 6, no. 1, p. 016106, 2018.

[56] S. Song *et al.*, "Joint effect of magnesium and yttrium on enhancing thermoelectric properties of n-type Zintl Mg3+ δY0. 02Sb1. 5Bi0. 5," *Materials Today Physics,* vol. 8, pp. 25-33, 2019.

[57] K. Imasato, M. Wood, J. J. Kuo, and G. J. Snyder, "Improved stability and high thermoelectric performance through cation site doping in n-type La-doped Mg 3 Sb 1.5 Bi 0.5," *Journal of Materials Chemistry A,* vol. 6, no. 41, pp. 19941-19946, 2018.

[58] Q. Zhu, S. Song, H. Zhu, and Z. Ren, "Realizing high conversion efficiency of Mg3Sb2-based thermoelectric materials," *Journal of Power Sources,* vol. 414, pp. 393-400, 2019.

[59] Y. Pan *et al.*, "Melt-centrifuged (Bi, Sb) 2Te3: engineering microstructure toward high thermoelectric efficiency," *Advanced Materials,* vol. 30, no. 34, p. 1802016, 2018.

[60] Z. Chen *et al.*, "Vacancy-induced dislocations within grains for high-performance PbSe thermoelectrics," *Nature communications,* vol. 8, p. 13828, 2017.

[61] H. Zhao *et al.*, "Engineering the Thermoelectric Transport in Half-Heusler Materials through a Bottom-Up Nanostructure Synthesis," *Advanced Energy Materials,* vol. 7, no. 18, p. 1700446, 2017.

[62] S. I. Kim *et al.*, "Dense dislocation arrays embedded in grain boundaries for high-performance bulk thermoelectrics," *Science,* vol. 348, no. 6230, pp. 109-114, 2015.

[63] H. Okamoto, "Mg-Sb (Magnesium-Antimony)," *Journal of phase equilibria and diffusion,* vol. 31, no. 6, pp. 574-574, 2010.

[64] H. Q. Trinh, J. O. Jo, S. B. Lee, and Y. S. Mok, "Preparation of red nitride phosphor from powder mixture of metal nitrides using spark plasma sintering," *Current Applied Physics,* vol. 14, no. 8, pp. 1051-1056, 2014.

[65] P. Cavaliere, B. Sadeghi, and A. Shabani, "Spark Plasma Sintering: Process Fundamentals," in *Spark Plasma Sintering of Materials*: Springer, 2019, pp. 3-20.

[66] M. Suárez *et al.*, "Challenges and opportunities for spark plasma sintering: a key technology for a new generation of materials," in *Sintering Applications*: IntechOpen, 2013.

[67] S. Song *et al.*, "Study on anisotropy of n-type Mg3Sb2-based thermoelectric materials," *Applied Physics Letters,* vol. 112, no. 9, p. 092103, 2018.

[68] I. Pallecchi, M. Monni, P. Manfrinetti, and M. Putti, "Band filling and disorder effects on the normal state thermoelectric behavior in MgB2," *Journal of Physics: Condensed Matter,* vol. 31, no. 16, p. 164001, 2019.

[69] Y. Wu *et al.*, "Lattice Strain Advances Thermoelectrics," *Joule,* vol. 3, no. 5, pp. 1276-1288, 2019.

[70] Z. Liu, J. Mao, T.-H. Liu, G. Chen, and Z. Ren, "Nano-microstructural control of phonon engineering for thermoelectric energy harvesting," *MRS Bulletin,* vol. 43, no. 3, pp. 181-186, 2018.

[71] J. Shuai, B. Ge, J. Mao, S. Song, Y. Wang, and Z. Ren, "Significant role of Mg stoichiometry in designing high thermoelectric performance for Mg3 (Sb, Bi) 2-based n-type zintls," *Journal of the American Chemical Society,* vol. 140, no. 5, pp. 1910-1915, 2018.

[72] T. Kanno *et al.*, "Enhancement of average thermoelectric figure of merit by increasing the grain-size of Mg3. 2Sb1. 5Bi0. 49Te0. 01," *Applied Physics Letters,* vol. 112, no. 3, p. 033903, 2018.

[73] J. J. Kuo *et al.*, "Grain boundary dominated charge transport in Mg 3 Sb 2-based compounds," *Energy & Environmental Science*, vol. 11, no. 2, pp. 429-434, 2018.

[74] B. Madavali and S.-J. Hong, "Enhanced Thermoelectric Properties of p-type Bi 0.5 Sb 1.5 Te 3 Thermoelectric Materials by Mechanical Alloying and Spark Plasma Sintering," *Journal of Electronic Materials*, vol. 45, no. 12, pp. 6059-6066, 2016.

[75] E. B. Kim *et al.*, "Enhanced thermoelectric properties of Bi0. 5Sb1. 5Te3 composites with in-situ formed senarmontite Sb2O3 nanophase," *Journal of Alloys and Compounds*, vol. 777, pp. 703-711, 2019.

[76] D.-W. Liu, J.-F. Li, C. Chen, and B.-P. Zhang, "Effects of SiC nanodispersion on the thermoelectric properties of p-type and n-type Bi 2 Te 3-based alloys," *Journal of electronic materials*, vol. 40, no. 5, pp. 992-998, 2011.

[77] H. R. Williams *et al.*, "Spark plasma sintered bismuth telluride-based thermoelectric materials incorporating dispersed boron carbide," *Journal of Alloys and Compounds*, vol. 626, pp. 368-374, 2015.

[78] G. Li *et al.*, "Deformation mechanisms in high-efficiency thermoelectric layered Zintl compounds," *Journal of Materials Chemistry A*, vol. 5, no. 19, pp. 9050-9059, 2017.

[79] S. M. K. N. Islam *et al.*, "Giant enhancement of the figure-of-merit over a broad temperature range in nano-boron incorporated Cu 2 Se," *Journal of Materials Chemistry A*, vol. 6, no. 38, pp. 18409-18416, 2018.

[80] M. Li *et al.*, "Ultrahigh figure-of-merit of Cu2Se incorporated with carbon coated boron nanoparticles," *InfoMat*, vol. 1, no. 1, pp. 108-115, 2019.

[81] M. Shahabuddin *et al.*, "Microstructural and crystallographic imperfections of MgB2 superconducting wire and their correlation with the critical current density," *AIP Advances*, vol. 4, no. 1, p. 017113, 2014.

APPENDIX A

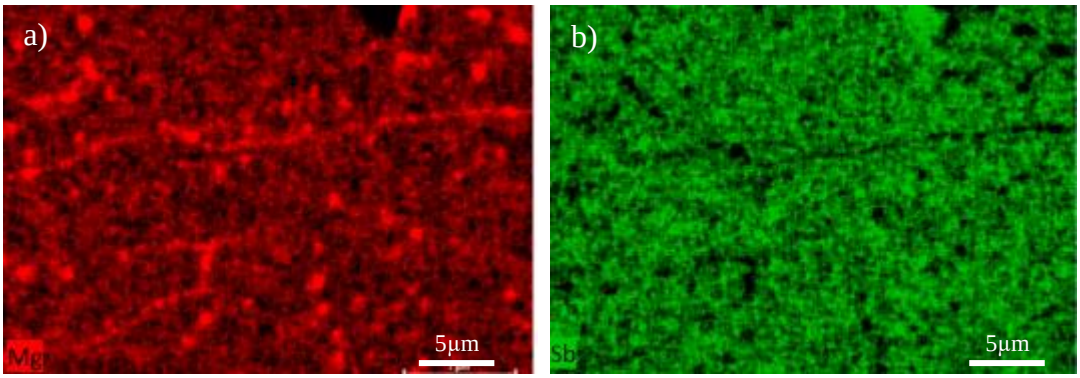

Figure A. 1 EDX mapping of Mg_3Sb_2 (MO40) sample a) Mg distribution B) Sb distribution

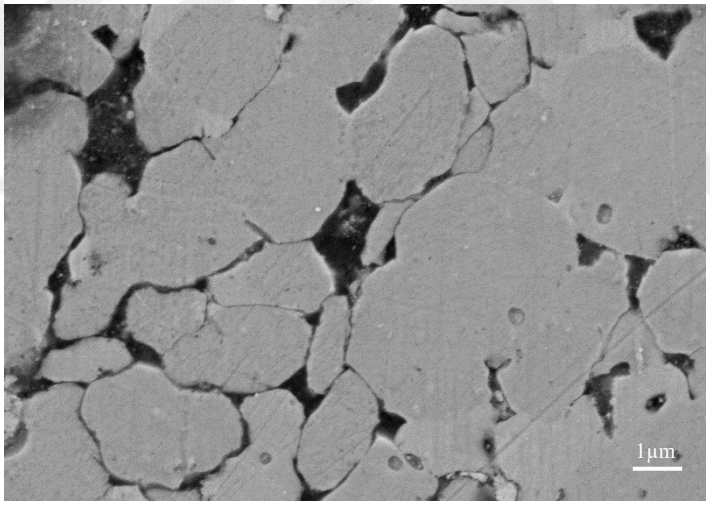

Figure A. 2 SEM image of melt-centrifuged $Mg_{3.2}Sb_{1.5}Bi_{0.49}Te_{0.01}$ sample (MO70) with 4 to 7 µm grains and 1 to 3 µm porosities.

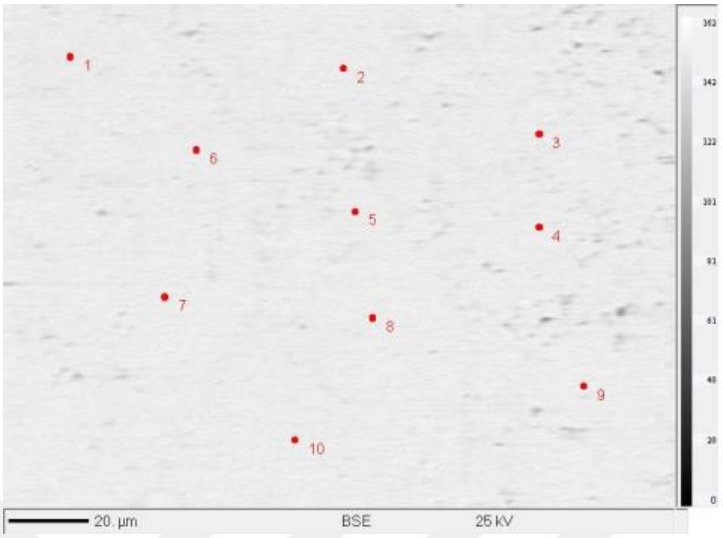

Figure A 3. 10 different spots corresponding to the WDX analysis of $Mg_{3.2}Sb_{1.5}Bi_{0.49}Te_{0.01}$ sample (MO57)

Table A.1 The WDX analysis results from 10 different spots for $Mg_{3.2}Sb_{1.5}Bi_{0.49}Te_{0.01}$ sample (MO57)

Elements (atomic%)	Spot 1	Spot 2	Spot 3	Spot 4	Spot 5	Spot 6	Spot 7	Spot 8	Spot 9	Spot 10
Sb	29.105	28.586	28.645	29.325	29.020	28.794	28.838	28.598	28.370	28.805
Mg	61.569	61.605	61.648	61.429	61.204	61.566	61.369	61.515	62.117	61.701
Bi	9.091	9.587	9.486	9.031	9.554	9.421	9.574	9.664	9.299	9.275
Te	0.235	0.221	0.221	0.215	0.222	0.218	0.218	0.222	0.215	0.218

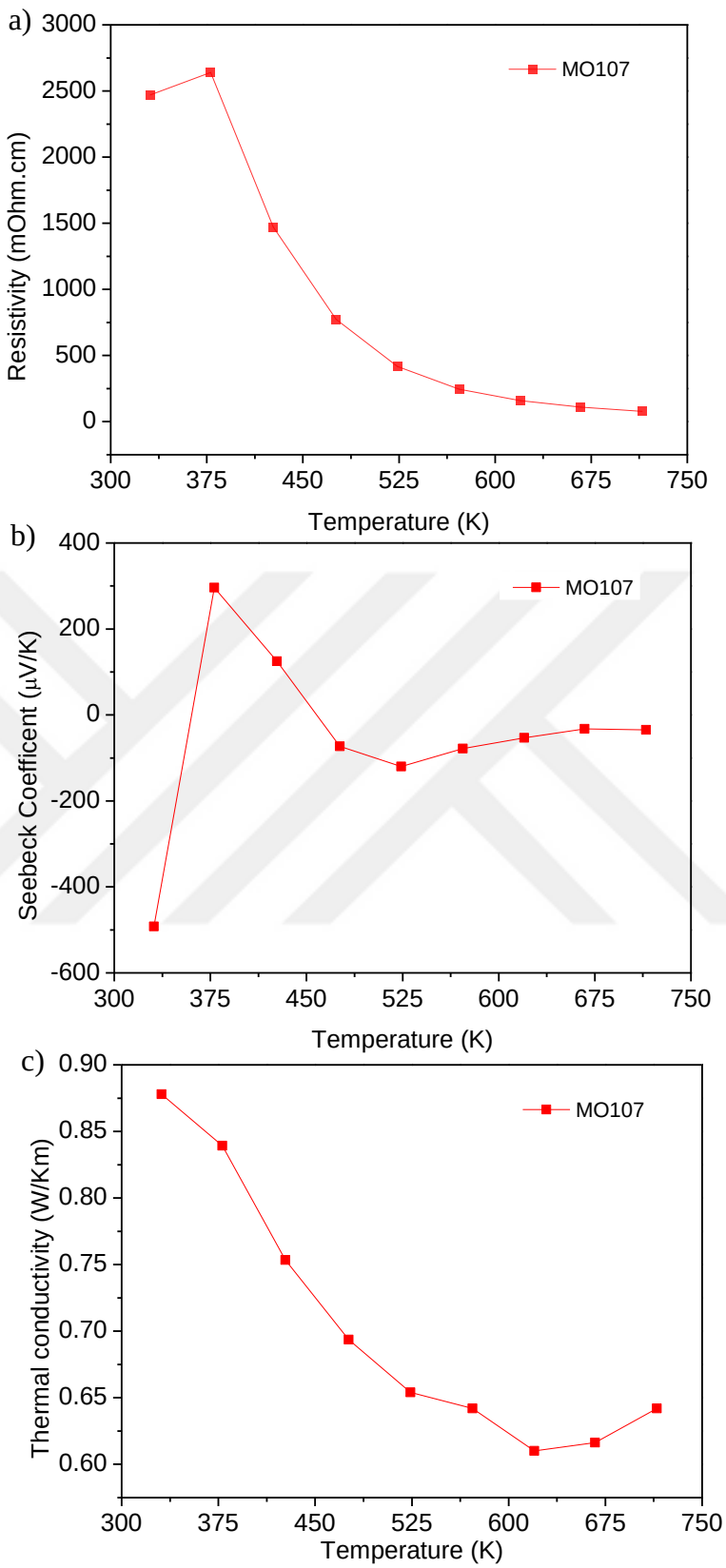

Figure A. 4 a) The electrical resistivity, **b)** Seebeck coefficent and **c)** thermal conductivity of MO107 ($Mg_{3.2}Sb_{1.5}Bi_{0.49}Te_{0.01}$ sample sintered at 800°C)